Investigation of light propagation in thin-film silicon solar cells by dual-probe scanning near-field optical microscopy

Stephan Lehnen

Member of the Helmholtz Association

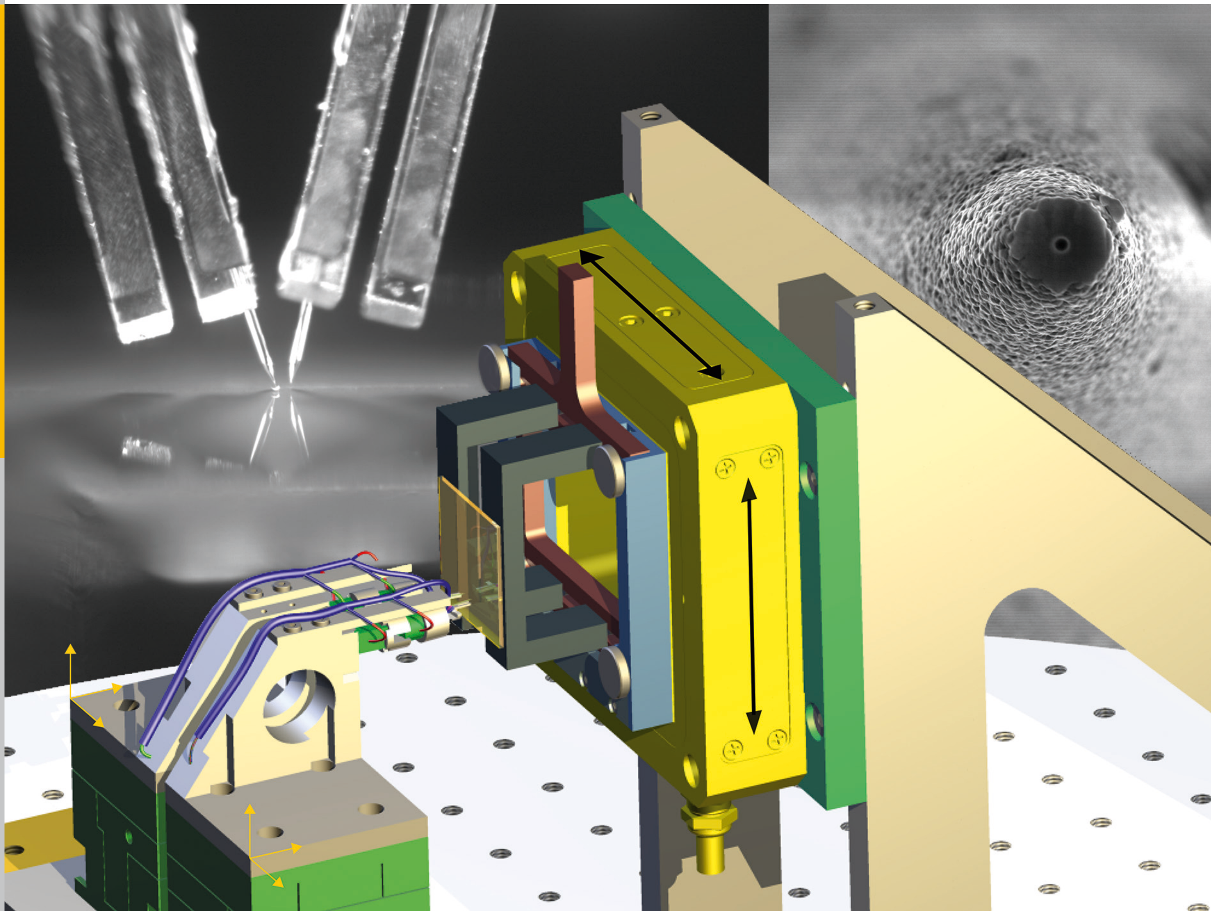

Energie & Umwelt /
Energy & Environment
Band / Volume 270
ISBN 978-3-95806-066-1

JÜLICH
FORSCHUNGSZENTRUM

Schriften des Forschungszentrums Jülich
Reihe Energie & Umwelt / Energy & Environment Band / Volume 270

Forschungszentrum Jülich GmbH
Institute of Energy and Climate Research
IEK-5 Photovoltaics

Investigation of light propagation in thin-film silicon solar cells by dual-probe scanning near-field optical microscopy

Stephan Lehnen

Schriften des Forschungszentrums Jülich
Reihe Energie & Umwelt / Energy & Environment Band / Volume 270

ISSN 1866-1793 ISBN 978-3-95806-066-1

Bibliographic information published by the Deutsche Nationalbibliothek.
The Deutsche Nationalbibliothek lists this publication in the Deutsche Nationalbibliografie; detailed bibliographic data are available in the Internet at http://dnb.d-nb.de.

Publisher and Distributor:	Forschungszentrum Jülich GmbH Zentralbibliothek 52425 Jülich Tel: +49 2461 61-5368 Fax: +49 2461 61-6103 Email: zb-publikation@fz-juelich.de www.fz-juelich.de/zb
Cover Design:	Grafische Medien, Forschungszentrum Jülich GmbH
Printer:	Grafische Medien, Forschungszentrum Jülich GmbH
Copyright:	Forschungszentrum Jülich 2015

Schriften des Forschungszentrums Jülich
Reihe Energie & Umwelt / Energy & Environment, Band / Volume 270

D 82 (Diss. RWTH Aachen University, 2015)

ISSN 1866-1793
ISBN 978-3-95806-066-1

The complete volume is freely available on the Internet on the Jülicher Open Access Server (JuSER) at www.fz-juelich.de/zb/openaccess.

Neither this book nor any part of it may be reproduced or transmitted in any form or by any means, electronic or mechanical, including photocopying, microfilming, and recording, or by any information storage and retrieval system, without permission in writing from the publisher.

Contents

1 Introduction **7**

2 Fundamentals **11**

2.1 Diffraction . . . 11
2.2 Diffraction Limited Resolution . . . 12
2.2.1 Abbe Limit . . . 13
2.3 Failure of the Kirchoff Theorem / Diffraction at Subwavelength Size Apertures . . . 14
2.4 Beyond the Diffraction Limit . . . 15
2.5 Light Trapping . . . 19
2.5.1 Yablonovitch Limit . . . 20
2.6 Shear-Force . . . 25
2.7 Device-Structure of a Silicon Thin-Film Solar Cell in n-i-p Configuration . 26

3 System Setup **29**

3.1 General Setup & Design Criteria for a Dual-Probe SNOM . . . 29
3.2 Motorised Coarse Alignment . . . 31
3.3 Piezo Fine Alignment . . . 31
3.4 Shear-Force Distance Control . . . 32
3.5 Cameras & Lighting . . . 35
3.6 Vibration Isolation . . . 36
3.7 Surface Markers . . . 37
3.8 Laser & Optical Setup . . . 38
3.9 Detector & Lock-In Technique . . . 38
3.10 Estimate of the Maximal Distance in between the Probes . . . 39

4 Optical Probes for Near-Field Microscopy **43**

4.1 Apertureless Probes . . . 43
4.2 Aperture Probes . . . 43
4.2.1 Probe Etching . . . 45
4.2.2 Probe Pulling . . . 45

4.2.3 Coating 46
4.2.4 Aperture Adjustment 46
4.3 Probe Preparation 48
4.4 Probe Characterisation 51

5 Modes of Operation **55**
5.1 Basic Modes of Operation 55
5.1.1 Collection Mode in Transmission Geometry 55
5.1.2 Collection Mode in Reflection Geometry 56
5.2 Dual-Probe Mode 57
5.2.1 Alignment of the Probes 58
5.2.2 Interaction between the Probes 59
5.3 Height-Scan Mode 60

6 Light Paths and Photon Loss Mechanisms in Dual Probe Measurements **63**
6.1 Absorption in the Sample Material 64
6.2 Distribution inside the Layer 65
6.3 Reflection Losses 67
6.3.1 Theoretical Background 67
6.3.2 Intensity Decay due to Reflection Losses 70
6.4 Light Guidance in the TCO Layer 72
6.5 Direct Light Transfer between Illumination and Detection Probe 72

7 Measurement of the Light Propagation in thin films **75**
7.1 Basic Dual-Probe Mode 75
7.1.1 Analysis by Line Scans 75
7.1.2 Analysis by Circular Averaging 77
7.2 Coupling Efficiency Eliminated Scan Mode 78
7.2.1 Wavelength & Texture Dependence of the Intensity Decay 80
7.3 Fact or Artefact? 82
7.3.1 De-convolution of the probe's shape from topography measurements 85

8 Simulations **87**
8.1 Ray-Tracing Approach 87
8.1.1 Ray-tracing for Realistic Angular Distribution 89
8.1.2 Limitations of Ray-Tracing 92
8.2 FDTD Simulations 94
8.2.1 Limitations of the Simulation 100

8.2.2 Angular Distribution of the SNOM-Probe Emission/Sensitivity . . . 101

9 Summary & Outlook **105**

9.1 Summary 105

9.2 Outlook 106

Zusammenfassung **109**

References **117**

Acknowledgments **119**

1 Introduction

Energiewende Global climate change, scarcity of resources, and reservations about nuclear energy have triggered a significant change in energy policy towards sustainability. Even the New York Times and The Economist use the German term *Energiewende* today to describe the ongoing transition to renewable energy [1–3]. Huge efforts are necessary to implement this transition. Several technologies for renewable energy are operational and are competing in terms of efficiency and energy costs. In the end, the acceptance of renewable energy, depends on reasonable costs.

Solar Cells Thin-film solar cells are likely to reduce costs in comparison to crystalline solar cells as they require less energy during the production process. In the case of silicon-based thin-film solar cells, the use of abundant and nontoxic material is an additional benefit. Furthermore, less silicon is required. However, while the low layer thickness significantly reduces the cost of production, it also reduces the capacity for light absorption. Weak absorptance has to be compensated for by advanced photon management techniques which trap the light by prolonging the light path inside the absorber layer. Various approaches for light-trapping have been developed, which use a variety of different physical phenomena [4]. No matter which kind of light-trapping concept is finally applied, the performance has to be evaluated using a suitable characterisation method.

Characterisation Standard characterisation methods, e.g. current-voltage characteristics and quantum efficiency measurements, can supply information about whether or not a solar cell equipped with a certain light-trapping concept achieves a higher efficiency. Nonetheless, these methods are often restricted to macroscopic information on the entire solar cell. The internal mechanism of light guidance therefore remains unknown. A deeper understanding of the internal mechanism is, however, the basis of a targeted development and implementation of new light-trapping concepts. Simulations are one way of gaining access to microscopic information about the interaction of light with sub-wavelength structures.

Simulations Different approaches exist to simulate light trapping in thin-film solar cells. Statistical descriptions reveal the limitations of light trapping based on assumptions,

which more or less accurately describe the actual devices. More detailed information on specific optical features is provided by ray-tracing. However, if the size of the involved structures decreases towards subwavelength scale, ray-tracing based on geometrical optics reaches the limits of physical validity. Finite-difference time-domain simulations, in contrast, are capable of calculating the fields on the required length scale. However, the high demand for computing power, in particular in the case of randomly textured interfaces, hampers the utilization of this method. Finally, the interaction of simulation and experiment is the key to new discoveries. In this context, near-field microscopy represents the experimental counterpart to simulations.

Near-field Microscopy The investigation of the optical properties of sub-wavelength-sized structures requires a tool with sufficiently high optical resolution. A scanning near-field optical microscope (SNOM) meets this requirement. Near-field microscopy offers fascinating insights into the nano world. Its versatile and unique capabilities to measure light intensities within the near-field of a light guiding layer, grants access to a deeper understanding and further improvement of light-trapping concepts. By measuring high spatial frequencies of the electromagnetic field, referred to as the evanescent field, a high optical resolution is achieved and information about light, trapped by total internal reflection, is accessible.

The idea for near-field microscopy goes back to an exchange of letters between Edward Hutchinson Synge and Albert Einstein in 1928 [5]. Ever since, near-field microscopy has been developed from a thought experiment to an established tool used in a wide range of different fields of research [6–9].

Previous SNOM measurements on thin-film solar cells have examined near-field effects on randomly textured interfaces [10, 11]. The investigated layer stacks were globally illuminated by a plane wave from the rear side, while the light intensity was locally measured on the front side. Due to the global illumination, the origin of a measured intensity at a specific position remains unknown. In other words, essential information about the propagation of light inside the layer are not accessible. Hence, a new approach is needed which offers modes of operation beyond the capabilities of single-probe SNOMs.

The detailed investigation of light-trapping requires to illuminate *and* detect locally by means of two separated probes. This concept is realized at a dual-probe SNOM which was setup from scratch in the course of this thesis. A dual probe SNOM applies two structuraly identical probes. One probe is connected to a source of illumination and couples light into the investigated layer whereas the light intensity is measured at some distance by an additional detection probe. This way, a dual probe SNOM adds the unique feature to actually measure and visualize light propagation in thin layers. A particular challenge is related to the surface texture of the investigated solar cells. Scattering at

local surface features strongly influence the light propagation. The microscope provides modes of measurement which are especially designed to compensate for the influence of local surface features.

Outline The scope of this thesis is to investigate light propagation in thin films by means of a newly set up dual-probe SNOM. The fundamental principles of microscopy beyond the diffraction limit are outlined in Chapter 1. Scanning with a fragile detection probe in extremely close proximity to a texture surface while the sample is illuminated locally by an additional illumination probe is a technical challenge. The general setup and design criteria for a microscope that meets this challenge are described in Chapter 2. Manufacturing an aperture with sub-wavelength diameter was an important milestone in the development of near-field microscopes. Chapter 3 describes how SNOM probes are manufactured, characterised and prepared for operation. A dual-probe SNOM has many modes of operation which are introduced in Chapter 4. Chapter 5 accounts for the various loss mechanisms of light propagation. Finally, Chapter 6 presents experiments on light guidance in hydrogenated microcrystalline silicon (μc-Si:H) absorber layers, which are compared to simulations in Chapter 7. Chapter 8 provides a summary and an outlook on future activities.

2 Fundamentals

The first chapter describes the fundamentals of near-field microscopy. It will be shown how near-field microscopes surmount the diffraction limit of classical microscopes. Furthermore, the concept of light-trapping is introduced. A theoretical limit of light-trapping, known as the Yablonovitch limit, is derived. The demand for a high resolution and the investigation of totally internal reflected light, require sub wavelength probe-to-sample distance. The applied distance control system relies on shear-forces in between the probe and the sample surface. The physical origin of shear-forces is outlined in this chapter.

2.1 Diffraction

The way diffraction phenomena are theoretically discussed, mainly depends on three parameters of the regarded system. Those are the largest extension of the diffracting object D (for simplicity a circular aperture is considered in the following), the wavelength λ, and the distance R. (R is the smallest of the two distances between illumination source and aperture R_{dp} or between aperture and observation plane R_{op}.) The Fresnel number [12]

$$F = \frac{D^2}{R\lambda} \tag{2.1}$$

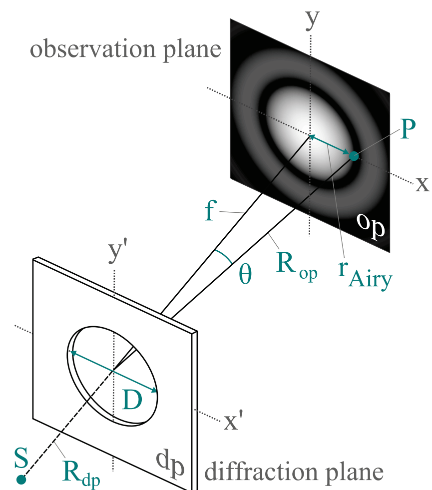

Figure 2.1: Illustration of the different parameters which determine the diffraction at a radial aperture at various distances

describes the relative size of the parameters. If the distance between the observation plane and the aperture is small (in comparison to the aperture size, $F \geq 1$), the image of the aperture strongly resembles the original aperture shape and is only slighty distorted. Diffraction at this length scale is denoted *near-field* or *Fresnel diffraction*. At large distance ($F \ll 1$), the image of the aperture is strongly dom-

inated by diffraction pattern, which are called *Airy-pattern* (illustrated at the observation plane in Fig. 2.1). A further increase in distance enlarges the diffraction pattern, without changing its shape [13]. This regime is referred to as *far-field* or *Fraunhofer diffraction*.

The different character of Fresnel and Fraunhofer diffraction is also evident from the shape of the wavefronts. The point source S (Fig. 2.1), as well as every point of the aperture, can be regarded as source of a spherical wave (Fresnel-Huygens principle). If the distance between the source of the spherical wave and the point of observation is small, the bending of the wavefronts can not be neglected, since the distances between the source and various points at the observation plane vary significantly. Consequently, the field and also the phase differs (Fresnel diffraction). If, however, the distance is large and the wavefronts are plain at scales in the order of the aperture size, Fraunhofer diffraction occurs.

In the following section, the resolution limit of a far-field microscope is derived by applying Fraunhofer diffraction.

2.2 Diffraction Limited Resolution

Resolving power is the measure of the ability of an instrument to separate two neighbouring point-like objects [14].

The resolving power of classical far-field microscopes is, even in the absence of any aberrations and in the limit of infinite signal-to-noise detection, limited by diffraction. If an object is observed by a far-field microscope, the light originating from the object is diffracted at the finite size of the microscope aperture due to its wave nature. In case of an point-like object, the resulting image reveals an Airy pattern. If two neighbouring object points are imaged, their Airy-patterns overlap, making it difficult to discriminate the objects from each other.

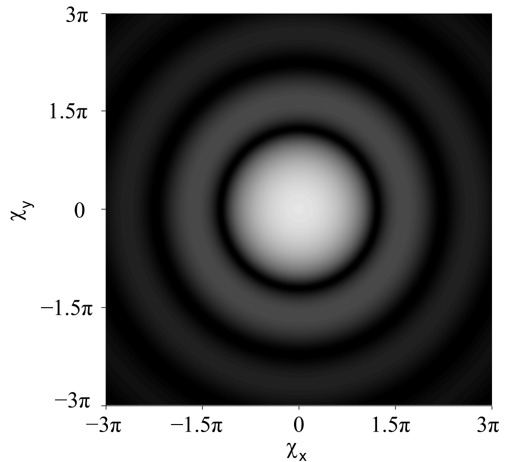

Figure 2.2: 2D plot of an Airy disc (intensity plotted on a logarithmic scale[1])

The determination of the minimum distance at which the two patterns can just be

[1] To improve the visibility of the outer rings and to avoid plotting zero intensities at a logarithmic scale, the maximum intensity is set to one and an offset of 1.5×10^{-3} is added to the intensity distribution prior to transferring the intensity to a logarithmic scale.

distinguished is, to some extent, a matter of definition. Hence, various definitions exist. Rayleigh stated that two objects are just resolved if the centre of the Ariy-disc of one object falls on the first Ariy-disc minimum of the second object [15]. In this case, the minimal resolvable distance between the object points is related to the radius of the Ariy-disc which is determined by the wavelength λ, the diameter of the aperture D and the focal length f [16].

$$r_{\mathrm{Airy}} = 1.22\,\frac{\lambda}{D}\,f \tag{2.2}$$

2.2.1 Abbe Limit

Ernst Abbe (1840 - 1905) investigated theoretically, but also by experiments, the resolution limit of optical instruments in case of coherent illumination. The resolution limit can be derived by considering a line grating as test object. The smallest grating constant d that can just be resolved corresponds to the resolution limit.

The line grating is illuminated at normal incidence and the diffracted light is observed through an objective lens (Fig. 2.3). The grating diffracts light into different orders of diffraction. The first maxima of diffraction occurs, if the path length difference between adjacent slits of the grating equals the wavelength. For a wavelength λ inside the medium of refractive index n and a grating constant d, this results in

$$\sin(\theta_1) = \frac{\lambda}{n\,d} \tag{2.3}$$

Depending on the aperture angle α of the objective, higher orders of diffraction are not captured (Fig. 2.3). In order to gain an image of the grating, at least the diffraction order zero and one have to be imaged by the objective. Hence, the aperture angle α has to be at least equal to θ_1. From Eq. 2.3 follows

$$d = \frac{\lambda}{n\,\sin(\alpha)} = \frac{\lambda}{NA} \tag{2.4}$$

whereby NA is the numerical aperture of the objective. The resolution can be further increased, if only the diffraction order zero and +1 is captured and the illumination is performed at an angle equal to the aperture angle α. Technically, this is realised by a condenser [17]. The resolution is increased to

$$d = \frac{\lambda}{2\,NA} \qquad \text{(Abbe)} \tag{2.5}$$

which is the *Abbe limit of diffraction*. Equation 2.5 represents the minimal distance

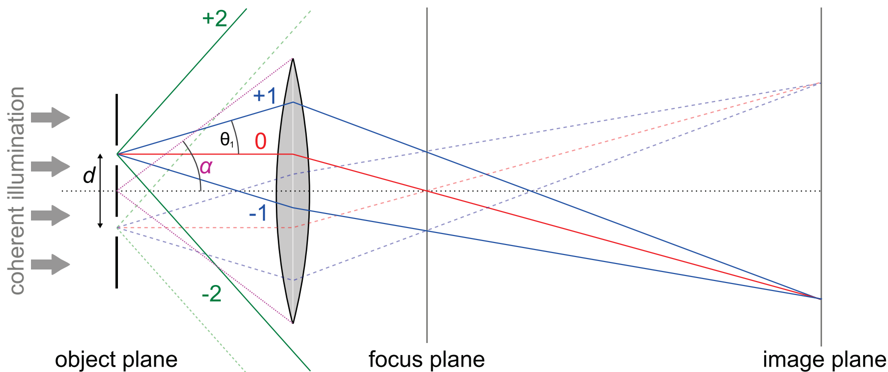

Figure 2.3: Imaging of a line grating with an objective. The grating diffracts the light into different orders of diffraction (the orders 0 to ± 2 are displayed). The aperture angle α has to be equal or greater than the angle θ at which the first diffraction maximum occurs to allow for imaging an object of size d. (Illustration based on [18])

between two adjacent point objects at the focus plane[2] which can just be resolved by a microscope in case of a circular aperture and coherent illumination. In case of visible light ($\lambda = 500\,\mathrm{nm}$) and a high numerical aperture of $N.A. = 1.5$ (oil ambient between objective and sample), the spatial resolution is even under ideal conditions (i.e. infinite signal-to-noise detection, no aberrations or distortions etc.) limited to about 210 nm [15]. As a rule of thumb, the best achievable resolution of far-field microscopes is in the order of half a wavelength.

According to the Abbe limit, the resolution can be increased by using shorter wavelengths (or even matter waves) or by increasing the numerical aperture. However, the Abbe limit is rather a technical limitation than a fundamental one. There are indeed options to exceed the Abbe limit and to decrease the diffraction limit (confocal microscopy) or to surmount it (near-field microscopy)[14].

2.3 Failure of the Kirchoff Theorem / Diffraction at Subwavelength Size Apertures

Fresnel and Fraunhofer diffraction are approximations of the Kirchhoff's diffraction theory. The theory is based on assumptions which fail, if the physical dimensions associated with aperture size, source distance, or observation plane distance reach subwavelength size. An example of an assumption, not valid in near-field, is that the aperture is illuminated by a

[2] The resolution limit of objects placed at the focal plane is usually higher than along the optical axis.

spherical wave having a $1/r$ field dependency [15]. Actually, the electric field of a dipole has indeed terms which decay with $1/r^2$ and $1/r^3$. These terms are usually neglected in the far-field since almost all energy transferred to the far-field is related to the $1/r$ term [15]. However, at subwavelength distance, terms which have a strong distance dependency can still have a significant contribution to the electric energy density.

Since fundamental principles of diffraction theory are invalid in the near-field, Bethe and Bouwkamp apply an alternative approach [19–21]. The Bethe-Bouwkamp theory describes the transmission through a sub-wavelength circular hole in a perfectly conducting infinitely thin screen [22]. An exemplary result is that the power transmitted through an aperture with radius a is proportional to a^6, rather than to a^4 as calculated based on Kirchhoff's diffraction theory, or a^2 as expected by geometrical consideration [23].

2.4 Beyond the Diffraction Limit

The resolution is ultimately limited by the Heisenberg uncertainty relation, which states that the product of the uncertainty in the spatial position of a particle and the uncertainty of its momentum in the same direction cannot become smaller than $\hbar/2$ [14]. In case of photons

$$\hbar \Delta k_x \, \Delta x \geq \hbar/2 \tag{2.6}$$

which leads to

$$\Delta x \geq \frac{1}{2\Delta k_x} \tag{2.7}$$

whereby

$$k = \sqrt{k_x^2 + k_y^2 + k_z^2} \tag{2.8}$$

According to Eq. 2.7, the spatial confinement is inversely proportional to the spread of wave vectors. A large spread of wave vectors leads to high spatial confinement, i.e. high spatial resolution. The spread of wave vectors can be increased by increasing one component (for example k_x) above the length of the total wave vector, in such a way, that $k_x^2 + k_y^2 > k^2$. To satisfy Eq. 2.8, another component, e.g. k_z, has to become imaginary.

Physically, an imaginary wave vector component occurs, whenever light is totally reflected. In the following, k_x and k_y are defined to be parallel to an interface between two adjacent media of different refractive index n and n'. The boundary plane is located at

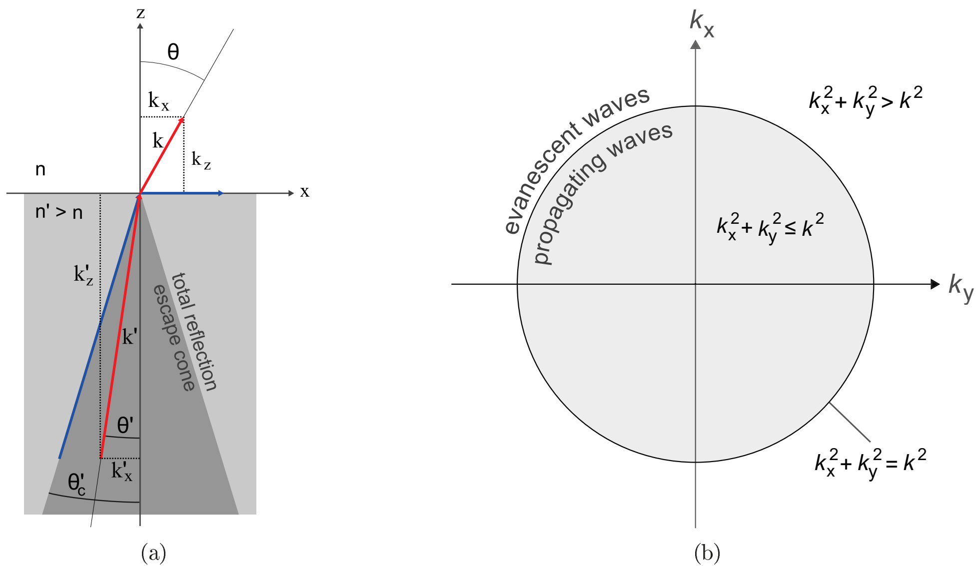

Figure 2.4: (a) Refraction at an interface between two media with different refractive indices. Evanescent waves occur if the angle of incidence θ' gets larger than the critical angle θ'_c (b) Illustration of the k-space of evanescent and propagating waves

$z = 0$. The wave vector $\mathbf{k}'$ of the incident light is parallel to the x/z-plane. Figure 2.4(a) illustrates the refraction at the interface for light, incident at an angle θ', which is smaller than the angle of total reflection (referred to as critical angle θ'_c). The z-component of the wave vector decreases upon the transition to a media with lower refractive index. Nevertheless, k_z is real and $k_x^2 + k_y^2 \leq k^2$. The incident wave is refracted at the interface but remains a propagating wave.

If the angle of incidence approaches the critical angle, k_z vanishes. A further increase results in an imaginary k_z. Figuratively speaking, the wave is refracted over the horizon [24]. The impact of a complex wave vector component arises by considering the transmitted field E_t [25].

$$\begin{aligned} E_t \propto e^{\mathbf{ikr}} &= e^{\mathrm{i}k\sin(\theta)x}\, e^{ik\cos(\theta)z} \\ &= e^{\mathrm{i}k\sin(\theta)x}\, e^{-zk\sqrt{\frac{\sin^2(\theta')}{\sin^2(\theta'_c)}-1}} \\ &= e^{\mathrm{i}k\sin(\theta)x}\, e^{-\gamma z} \end{aligned} \tag{2.9}$$

As soon as the angle of incidence θ' is larger than the critical angle θ'_c, the factor γ is real and Eq. 2.9 describes a wave, which is propagating along the boundary plane, but decays

exponentially behind the interface at $z > 0$. This kind of wave is called *evanescent* which derives from Latin and means "vanishing" or "imperceptible" [13].

The limit between propagating and evanescent waves matches a circle in k-space and is illustrated in Figure 2.4(b).

$$\text{propagating waves:} \quad k_x^2 + k_y^2 \leq k^2 \tag{2.10}$$

$$\text{evanescent waves:} \quad k_x^2 + k_y^2 > k^2 \tag{2.11}$$

The resolution of a microscope can be strongly increased if it is capable of detecting evanescent waves. Unfortunately, evanescent waves have, as the name suggests, the property to decay rapidly in space. According to Eq. 2.9, the evanescent field is proportional to $e^{-\gamma z}$, with the decay constant γ given by

$$\gamma = k\sqrt{\frac{\sin^2(\theta')}{\sin^2(\theta'_c)} - 1} \tag{2.12}$$

Figure 2.5 illustrates the penetration depth into air for selected wavelengths at a μc-Si:H/air interface. The penetration depth depends on the angle of incident and is defined as the distance at which the evanescent field is decreased by $1/e$. The graph reveals, that the sensing element of a microscope has to be placed very close to the interface, in best case at a distance smaller than $\lambda/2$. Furthermore, a high resolution is correlated with a

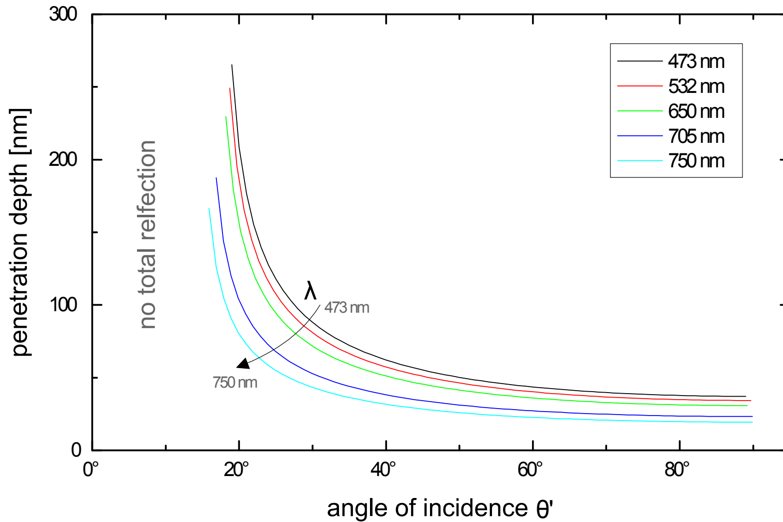

Figure 2.5: Penetration depth of the evanescent field into air in dependence of the angle of incidence θ' for selected wavelengths (calculated for a μc-Si:H/air interface)

high bandwidth in k-space (Eq. 2.7). Unfortunately, high values of k_x are related to high angles of incidence which have a small penetration depth, supporting the demand for a short distance between interface and sensing element.

Evanescent waves do not transport any net energy in the direction normal to the interface.[3] However, if evanescent waves reach a medium of sufficiently high refractive index, e.g. a SNOM probe, they are converted to propagating waves which transport information about subwavelength-structures from the near-field to the far-field (Fig. 2.6). Thereby energy is transferred beyond the interface. A similar effect is known as *frustrated total internal reflection* (FTIR). Here, an incident wave strikes a boundary plane towards a media with lower refractive index, e.g. air, at an angle at which it is totally reflected. If the gap between the media of the incident light and an adjacent media of higher refractive index is sufficiently small, photons surmount the gap. The occurrence of photons behind a barrier which is classically insurmountable is referred to as *quantum tunnelling*.

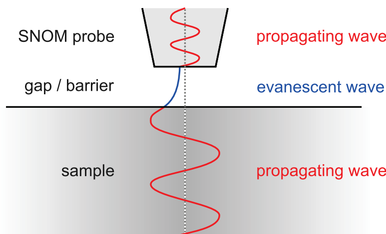

Figure 2.6: Schematic illustration of photon tunneling between surface and SNOM probe

It will be discussed later (Chap. 4), how the sensing element of a near-field microscope is actually realised. From the discussion above it is already obvious, that the sensing element has to be emerged into the evanescent fields in subwavelength distance above the surface. Additionally, it needs to be able to guide the converted evanescent waves to a detector placed in some (macroscopic) distance.

The limited resolution of far-field microscopes, derived in the previous chapter, can as well be regarded as a direct consequence of spatial filtering. As a result of the fast decay of evanescent waves, far-field microscopes are limited to the detection of propagating waves (shaded area in Fig. 2.4(b)). A limited bandwidth in k-space is related to a limited resolution in real space.

It is the essence of near-field microscopy to extend the accessible area in k-space to the domain of evanescent waves and, thereby, to increase the resolution to a subwavelength scale.

[3] The time averaged Poynting vector component perpendicular to the interface is zero.[14]

2.5 Light Trapping

A basic prerequisite for the generation of electricity from sunlight is the absorption of photons. Depending on the photon energy and the applied absorption material, the distance, photons pass in average, before being absorbed, differs. The length, at which the intensity is decreased by $1/e$, is referred to as absorption length. If the absorption length is distinctly shorter than the absorber layer thickness, virtually all photons are absorbed before reaching the rear side of the absorber layer. In this case, there is no reason to think about any light trapping concepts since the absorption is not limiting the solar cell efficiency.[4] If, however, the absorption length is distinctly longer than the absorber layer thickness, a major part of the incident radiation leaves the absorber without contributing to the generation of photo-generated charge carriers (Figure 2.7 (a)).

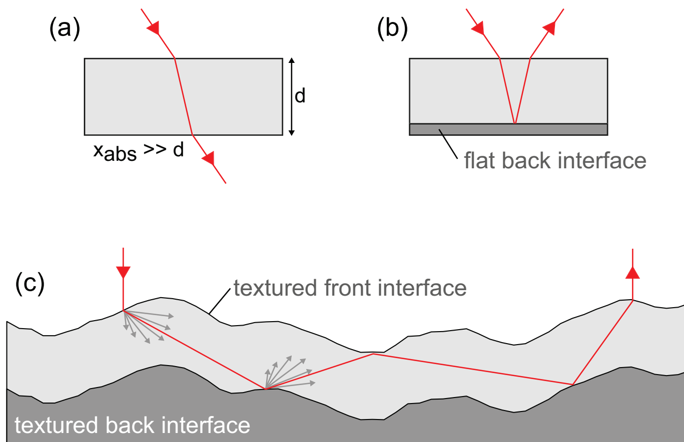

Figure 2.7: (a) Transmittance of light through an absorber layer which has a distinctly lower thickness d than the absorption length x_{abs} of the incident light (b) A flat back reflector doubles the path of light inside the layer and thereby increases absorption (c) Textured front and back interfaces scatter the incident light into preferably large angles and induce a strong path length increase.

In terms of high absorptance, thick layers are beneficial. On the other hand, thin absorber layers offer advantages with respect to material and processing time savings. Further more, thin layers lower the demand in material quality with regard to mobility and lifetime of photo-generated charge carriers or, particular in a-Si:H, the resistance against light-induced degradation [26, 27].

As it will be shown shortly, the thickness of 1 µm of the µc-Si:H layer is not sufficient

[4] Even in case of a sufficiently thick absorber layer, light-trapping concepts may reduce the reflectivity at the front interface and thereby increase the total amount of photons which enter the absorber layer.

to absorb the majority of the incident light at wavelengths longer than roughly about 600 nm. Hence, concepts are required to prolong the path of light inside the thin absorber layer. A longer light path results in a higher absorptance and potentially increases the cell efficiency. Increasing the path of light in a given material by applying optical concepts, is referred to as *light trapping*.

A simple approach for the implementation of light trapping is the use of a back reflector which already enhances the light path to twice the physical thickness (Figure 2.7 (b)). To go beyond, a large number of different approaches have been developed during the last decade which imply a variety of different physical phenomena, all aiming towards an increased light path [4]. Often, refraction and diffraction are applied to achieve a transfer of the wave vector of the incident light towards large components parallel to the surface. High orders of diffraction are attained by photonic crystals [28], dielectric gratings [29], or plasmonic gratings [30, 31].

A well established implementation of light trapping is to apply textured interfaces which scatter the incident light into preferably large angles. Light, scattered at a textured back reflector into angles beyond the escape cone will, to a great extent, be internally reflected at the front interface. The light is reflected multiple times and its path, thus, increased (Figure 2.7 (c)). However, for every theoretically possible light path, at which light is coupled into the absorber layer, the reversal process has to exist as well. Merely by the requirement for the existence of a reversal process, it can be derived that the light trapping efficiency is limited. A limit for the maximal average path length has been derived by Yablonovitch.

2.5.1 Yablonovitch Limit

In the limit of low absorption, the number of photo-generated carriers is strongly dominated by the average path length, photons pass before being transmitted at the front interface. The Yablonovitch limit provides an upper boundary for the average path length in case of isotropic illumination and low absorption [32].

An important prerequisite for the applicability of the Yablonovitch limit is an isotropic distribution of light in the absorber layer. This implies an ergodic system at which all states are equally occupied. A *Lambertian scatterer* is the physical model of a scatterer which induces a completely randomized distribution of the impinging light for all wavelengths, independent of the angle of incidence.

The luminance of a Lambertian scatterer is independent of direction and position. (A Lambertian scatterer has the same apparent brightness, no matter from which angle it is

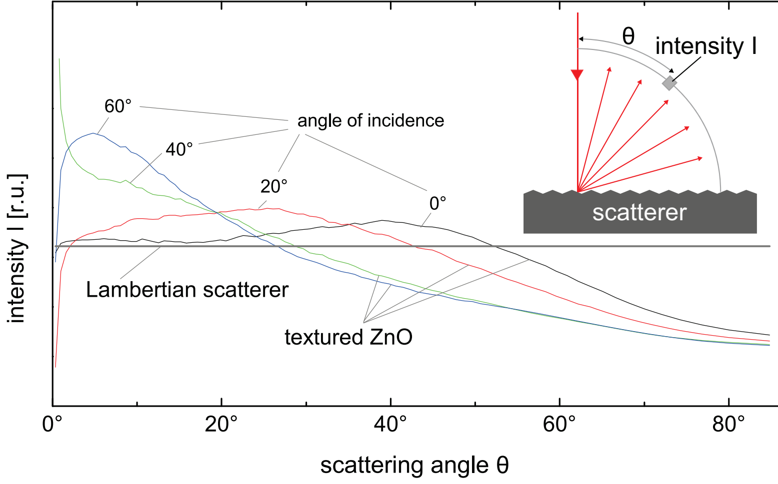

Figure 2.8: Comparison of the simulated angular distribution of light, scattered at a textured ZnO back reflector at various angles of incidence, with a Lambertian scatterer. The angular distribution is calculated within the µc-Si:H layer for a vacuum wavelength of 750 nm, assuming a standard etched ZnO texture (defined in Chap. 2.7). The intensity is plotted on a linear scale. The simulation is based on the phase model of Dominé [24].

viewed [12]). The angular distribution of a Lambertian scatterer $d\Phi_L$ is given by [33]

$$d\Phi_L = 2\cos(\theta)\sin(\theta)d\theta \tag{2.13}$$

A factor of two originates from the normalisation $\int_0^{\pi/2} d\Phi_L \stackrel{!}{=} 1$. In Figure 2.8, the simulated light distribution induced by a textured ZnO is compared to a Lambertian distribution of light.[5] As opposed to a Lambertian scatterer, the intensity per solid angle is not constant. Furthermore, the angular distribution of light scattered at a textured ZnO surface depends on the angle of incidence. It is obvious, that the applied textured surface only partly resembles a Lambertian scatterer.

On the basis of the assumed isotropic angular distribution, the average path, the light passes before reaching the back reflector, is determined by [33]

$$\langle l_0 \rangle = \int_0^{\pi/2} \frac{d}{\cos(\theta)} 2\cos(\theta)\sin(\theta)d\theta = 2d \tag{2.14}$$

[5] The simulations are based on the phase model introduced by Dominé [24].

The layer thickness d and the angle θ are illustrated in Figure 2.9. Equation 2.14 reveals, that in case of a Lambertian scatterer, the light passes an average distance, which equals twice the layer thickness, before it reaches the back reflector. Consequently, the front interface is reached after a distance of $4d$ under the assumption of a perfect back reflector. At each reflection at the front interface, a certain part of the light intensity will be transmitted (Fig. 2.9). In other words, a light ray has a certain chance to leave the layer. This chance depends on the transmittance T at the front interface. For some rays, the light path inside the layer ends at the first reflection. Thus, the average path length of a light ray after the first reflection at the front interface is given by

$$\langle l_1 \rangle = 4dT \tag{2.15}$$

The part of light which is not transmitted $(1 - T)$ reaches the front interface a second

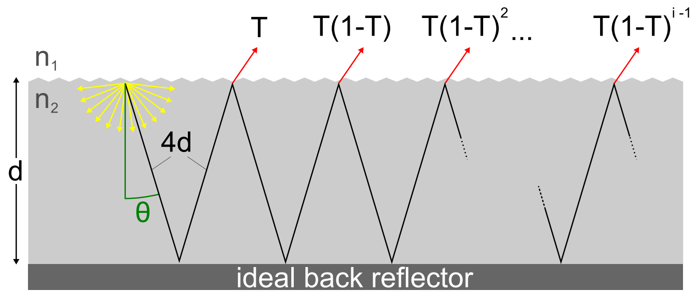

Figure 2.9: Derivation of the average path length in a medium of low absorption by considering the transmission of isotropic distributed rays at the front interface. The back reflector is assumed to have an ideal reflectance for all wavelengths. [Figure taken from [33] (modified)]

time and has again a certain chance to leave the layer.

$$\langle l_2 \rangle = 8dT(1 - T) \tag{2.16}$$

Hence, rays which had j interaction(s) with the front interface, have an average path length of

$$\langle l_j \rangle = j4dT(1 - T)^{j-1} \tag{2.17}$$

In summary, a bunch of rays with different path lengths exist. To determine the average path length of all rays $\langle l \rangle$, their light paths have to be added. Applying the geometric

series results in [33]

$$\langle l \rangle = 4d \sum_{j=1}^{\infty} jT(1-T)^{j-1} = \frac{4d}{T} \tag{2.18}$$

Since the Yablonovitch limit refers to the case of negligible absorption, the entire light intensity is transmitted after an infinite number of reflections

$$\sum_{j=1}^{\infty} T(1-T)^{j-1} = 1 \tag{2.19}$$

The probability of transmittance at the front interface scales with the ratio of light rays which have angles of incidence smaller than the angle of total reflection θ_c. The angular distribution is known from Eq. 2.13. The ratio of light rays which are transmitted at the front interface is [33]

$$T = \int_0^{\theta_c} 2\cos(\theta)\sin(\theta)d\theta = \sin^2(\theta_c) = \frac{1}{{n_2}^2} \tag{2.20}$$

whereby the critical angle θ_c is

$$\theta_c = \arcsin\left(\frac{n_1}{n_2}\right) \approx \arcsin\left(\frac{1}{n_2}\right) \tag{2.21}$$

for $n_1 = n_{\text{air}} \approx 1$. Combining Eq. 2.18 and Eq. 2.20 results in the average path length, referred to as Yablonovitch limit [33]

$$\langle l \rangle = 4n^2 d \tag{2.22}$$

The factor of n^2 is attributed to the density of states in a medium and the equipartition theorem which guarantees equal occupation of states internally as well as externally [34]. A factor of 2 originates from taking the back reflector into account and another factor of 2 accounts for the oblique light traversal. [35]

Figure 2.10 (a) illustrates the maximal average path length increase in μc-Si:H in relation to the layer thickness for a wavelength range from 300 to 1200 nm. The best compliance of the precondition for of low absorptance is given at long wavelengths close to the band gap. Here, the maximal average path length approaches 36 times the layer thickness. In Figure 2.10 (b) the absorptance in a 1 μm thick μc-Si:H layer is compared to the absorptance under consideration of the Yablonovitch limit. Additionally, the maximal absorptance according to Tiedje et al. is shown. Tiedje et al. extend a detailed balance

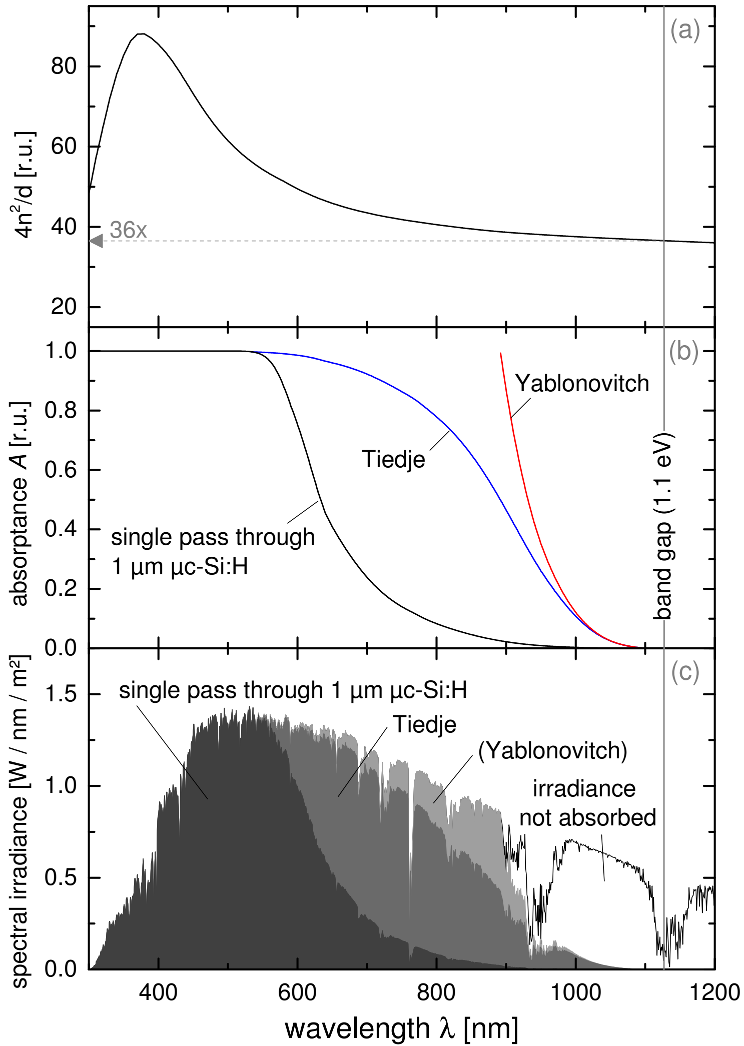

Figure 2.10: (a) Path length increase relative to the layer thickness d. (b) Absorptance in a 1 µm thick µc-Si:H layer (single pass) in comparison to the limit introduced by Tiedje [36] and Yablonovitch [32]. (c) Comparison of the absorbed incident solar power (AM1.5g [37]) in a 1 µm thick µc-Si:H layer (single pass) and under consideration of the Tiedje and Yablonovitch limit. (The Yablonovitch limit is displayed despite the fact that it is limited to low absorption)

method for calculating the radiative recombination limit to include free carrier absorption and Auger recombination in addition to radiative recombination [36]. The model is applicable if $\alpha d \ll 1$ which is true for λ >600 nm, in case of a 1 µm thick µc-Si:H layer.

The Yablonovitch limit is not restricted to any special kind of surface texture, as long as the light distribution remains isotropic. However, light trapping concepts which apply wave-optical effects are not considered in the Yablonovitch limit [32]. 2D grating structures can, at least for a limited wavelength range and with the drawback of significant angular dependency, exceed the Yablonovitch limit, as shown by a statistical coupled-mode theory introduced by Fan et al. [38].

2.6 Shear-Force

Shear force is the force acting on a laterally oscillating probe near a surface [39]. The occurrence of shear-forces is frequently used at near-field microscopes as basis of a distance control system, as described in Chapter 3.4.

The physical background of shear-force is still under discussion. A variety of different forces are accounted to be the origin of shear-force. An ascertain source are Van-der-Waals forces [40] between neutral molecules of the probe and those of the sample surface due to dipolar interactions. Van-der-Waals forces can sufficiently damp an oscillating probe and have an attractive force that decays by the 6th power of the probe to surface distance which explains the short range of the interaction.[6]

Various authors [42–44] account damping due to a surface contamination for the origin of shear forces. It was observed that a change in the humidity influences the shear-force interaction [45]. However, since shear-forces appear in ultra high vacuum as well, viscous damping due to capillary water can not be the solitary explanation of shear-force. Additionally, a viscous damping of an oscillation results in a decrease of the resonance frequency, in contrast to the observed increase.

Furthermore, it was proposed by Ayers [46] that a charged moving probe near the sample's surface would induce a movement of image charge in the sample. Since the charge flow is ohmic, the movement of the probe would result in a dissipative current. However, the calculated forces of $F_{max} = 5 \times 10^{-27}$ N are orders of magnitude smaller than the literature values which are in the pico to nano Newton range [42, 46, 47].

Shear-force distance control is thought to be a non-contact technique but this is still speculated upon [45]. According to Smolyaninov [48], who measured the resistance between the probe and a gold coated probe surface, metal coated probes touches the sample

[6] Strictly speaking, the decay by the 6th power of the distance relates to the interaction between single molecules. A weaker decay applies for the Van-der-Waals forces between macroscopic objects. [41]

during the measurement.

The extensive discussion about the universal mechanism behind shear-forces in literature reveals that various experimental circumstances influence the occurrence and strength of shear-forces. The type and length of the probes, the tendency of a sample to attract water, the medium of operation, and the sample material in general all have an influence on shear-forces.

Within the framework of the thesis, shear-forces are solely used for distance control. All measurements are performed in air, applying the same kind of aluminium coated glass fibre probes (Chap. 4). The investigated samples exhibit a homogeneous surface without clusters of different material which might induce different shear-forces (Chap. 7.3). These conditions are well suitable for using shear-force based distance control.

2.7 Device-Structure of a Silicon Thin-Film Solar Cell in n-i-p Configuration

For the investigation of light propagation, single junction thin-film silicon solar cells are used. The layer structure of the samples used within this thesis is illustrates in Figure 2.11. The structure corresponds to a n-i-p configuration. The term "n-i-p" relates to the order of deposition of the n-doped layer (n), the intrinsic layer (i), and the p-doped layer (p). At a n-i-p configuration, the light is not passing through the substrate. Hence, the front interface is accessible for SNOM measurements. Additionally, the substrate can be modified regardless of its transparency. This allows for investigations on new concepts, like plasmonic back contacts [30, 49].

In detail, the layer structure is composed as follows. A layer of aluminium doped zinc oxide (ZnO:Al) is deposited by radio frequency magnetron sputtering on top of a glass substrate. Subsequently the ZnO:Al is textured by wet-chemically etching in 0.5wt% HCl for 40 s [50].[7] Some of the investigated samples have the same layer structure, but non-textured interfaces.

A silver back reflector is deposited by thermal evaporation. A thin interlayer of ZnO:Al, sputtered on top of the back reflector, avoids plasmonic losses [51, 52]. The intrinsic and doped μc-Si:H layers are deposited by plasma-enhanced chemical vapor deposition (PECVD). The front contact consists of a transparent conductive oxide (TCO). In this case, ZnO:Al with a thickness of 80 nm is used as TCO. The TCO is highly transparent but has a rather low conductivity due to the small thickness. A silver grid increases the

[7] ZnO:Al, processed in the described manner, is referred to as *standard TCO* within this thesis. The abbreviation TCO is defined in the next section.

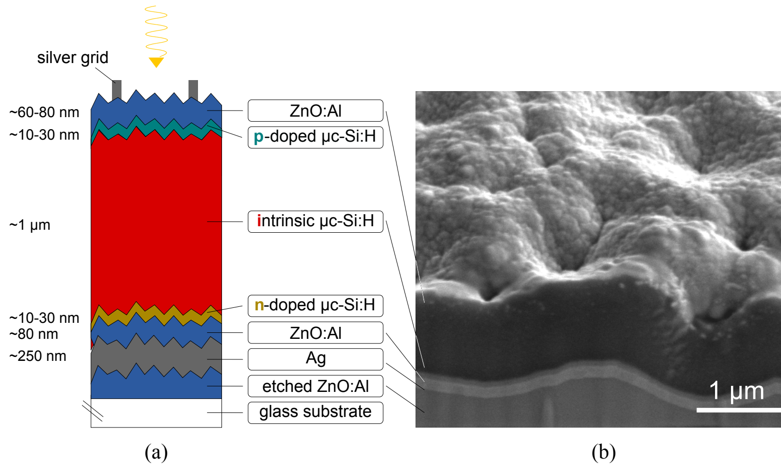

Figure 2.11: (a) Cross section of a textured single junction µc-Si:H thin-film solar cell in n-i-p configuration [49] (modified). (b) SEM image of the layer structure

conductivity of the front-contact.[8]

During operation as solar cell, the incident light is scattered at the textured ZnO:Al front contact of the solar cell. Charge carriers are generated in the µc-Si:H layer. Light which is not absorbed on the first path is reflected and scattered at the silver back reflector. Scattering at the back reflector strongly contributes to the light-trapping efficiency [53, 54].

[8] The distance between the silver grid lines is large in comparison to the size of usual scan areas of SNOM-measurements. Hence, there is plenty of space in between for measurements.

3 System Setup

A dual-probe SNOM suitable for the considered measurements was not commercially available. Hence, the microscope had to be setup from scratch in the course of this thesis. This chapter outlines the challenges and the technological solutions. Before describing the different components in detail, the following section is supposed to provide on overview of the general design criteria for a dual-probe SNOM.

3.1 General Setup & Design Criteria for a Dual-Probe SNOM

The experimental task is to measure light-trapping and light guidance in textured thin-films. Therefore, a high optical resolution is essential which is not feasible with far-field microscopes due to the diffraction limit (Chap. 2.2). "Far-field" simply means that the sensing element of the microscope, e.g. the lens, is placed at a distance to the sample which is large in comparison to the wavelength. The key idea of near-field microscopy is to surmount the classical resolution limit by approaching a sub-wavelength size measuring probe in sub-wavelength sample distance. Thereby, the resolution is determined by the aperture of the probe rather than by the wavelength.

Common probes have apertures in the order of 50 nm, offering a resolution in the same order of magnitude (Chap. 4). The challenge is to guide the extremely fragile probe in very close distance of about 20 nm above a textured surface with a texture height of up to 1 μm. Thereby, a high position accuracy in all spatial directions is essential to ensure that the position accuracy is neither limiting the optical resolution of the microscope nor the probe-lifetime. A piezo-based fine alignment meets the requirement and allows for smooth movements on the nanometre scale (Chap. 3.3). The range of scan devices with nanometre resolution is limited to small scales. Hence, a coarse alignment is necessary which has to be stable enough to avoid any undesired movement of the probe (Chap. 3.2). Furthermore, high precision on small scales is only feasible with a proper vibration isolation. Therefore, the microscope is placed on top of a vibration-cushioned optical table (Chap. 3.6).

A critical part of the experiment is the approaching of the probes. Both, the approach of the probes towards the sample surface and the approach of the probes towards each other

are experimentally challenging. A precise control of the approaching process on all scales is mandatory to avoid probe crashes. Several cameras with different and partly adjustable magnifications are used to monitor the probes from a centimetre to a micrometre range (Chap. 3.5). The distance control on smaller scales is realised by a shear-force mechanism (Chap. 3.4). It detects if the probe is in direct vicinity to the sample surface and thereby avoids probe crashes. Due to the very small gap in between the probe and the sample, the distance control needs to be fast to detect any change in the probe's distance to the surface at reasonable scan speed.[1]

In order to measure optical properties, the sample is illuminated by lasers (Chap. 3.8). Six lasers with wavelengths between 473 and 750 nm are operated simultaneously to cover the visible part of the solar spectrum. However, the detector is not able to distinguish between photons of different wavelengths. Hence, the laser intensity is modulated and the detector signal is fed into lock-in amplifiers. In dual-probe mode, the attenuation of the light after passing two probes and several micrometre of the sample material is strong and only a few photons per second reach the detector. A peltier cooled GaAs-detector has sufficient low noise for the low light intensities and is sufficiently fast (Chap. 3.9).

All laser beams need to be perfectly aligned to facilitate an effective coupling of multiple laser beams into a single glass fibre connected to the illumination probe. The attenuation upon transmission through the probe into the layer (or vice versa) changes wavelength-dependent at the transition of the probe from far-field to near-field distance. The adjustment of the intensities, by exchanging neutral density filters while the probe is only 20 nm apart from the sample surface, requires once more an elaborated vibration isolation.

Last but not least, the sheer number of devices is an additional challenge. For a dual-probe microscope all devices related to the two probes, i.e. the coarse and fine alignment, the different parts of the shear-force distance control, and the camera system are needed twice. Controlling two probes in three spatial directions on a coarse and fine scale in addition to the capability to move the sample in two directions adds up to 14 axes. Additionally, the motorised adjustment of the cameras add another 7 axes in total. Measuring with up to six wavelengths simultaneously implies that devices like lasers, lock-in amplifiers, frequency generators and so on are six-fold present. All the devices need to be controlled by a measurement software and the resulting data has to be digitalized, saved, and analysed.

[1] *thought experiment:* A typical scan speed is 1 µm/s. This may appear rather slow but a comparison with the macroscopic world may change this impression. A speed of 1 µm/s in a probe-to-sample distance of 20 nm above 1 µm hills is equivalent to flying above 2 km high mountains in a flight altitude of 40 m above ground with a speed of 7200 km/h (Mach 5). The need for an advanced distance-control system is obvious.

3.2 Motorised Coarse Alignment

The coarse position of the probes is controlled by motorised linear stages. The mechanical design of the coarse alignment is dimensioned for much higher loads than the pure weight of the attached probe assembly group. This helps to prevent an amplification of vibrations even if the linear stages are extended to the maximal position. The motor controller (thorlabs T-Cube) offers manual control as well as remote control by the measuring computer which can save certain positions and reset them on demand.

3.3 Piezo Fine Alignment

Figure 3.1 illustrates the different components of the fine alignment. The alignment at small scales is realised by piezo based nanopositioning stages from physikinstrumente (PI). Both stages are equipped with so called NanoCubes (P611-3S). This compact multi-axes piezo system has a travel range of 100 µm in all spatial-directions with a specified accuracy of 1 nm. For some measurements, it is advantageous to move the sample instead of the probes. Therefore, the sample holder is attached to a scan frame (PI P-733.2CL) which has a travel range of 100 µm in x- and y-direction. The piezo stages are operated in a close-loop mode, meaning that the real extension in all direction is measured. This helps to avoid a drift of the absolute probe position and facilitates to perform long scans (e.g.

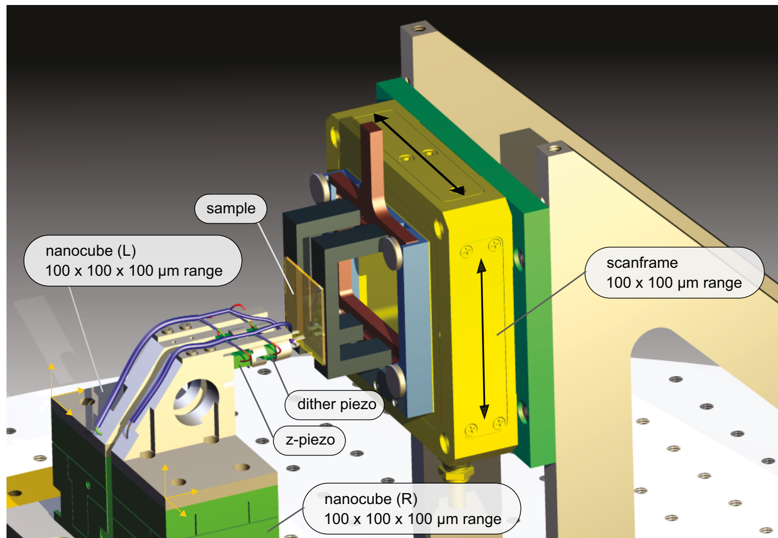

Figure 3.1: Illustration of the piezo based fine alignment of the left and right probe and the sample

10 hours) without any visible drift.

The data communication to the positioning devices was originally realised by a GPIB connection and each change in position was transferred separately. Although it takes only 100 ms to transfer a positioning request, the large number of positions per measurements (180 000 for a standard measurement) easily adds up to hours only for the data communication. A change to a different control mode at which the positions of a whole scan line are calculated in advance, increased the communication speed to a level at which it is not limiting the scan speed any more. However, the synchronisation between the current position and the measured light intensities is challenging.

3.4 Shear-Force Distance Control

Shear-force distance control is based on a decrease in the oscillation amplitude of a resonantly dithered tapered fibre during its approach to a surface [48]. It is applicable in air, fluids [55], ultra high vacuum, and in superfluid helium [48]. No light is needed for the detection which makes shear-force distance control perfectly suitable for applications where low light intensities have to be detected. In contrast to a distance control which relies on measuring tunnel currents, this method does not depend on conductive surfaces and is applicable to a wide range of different samples.

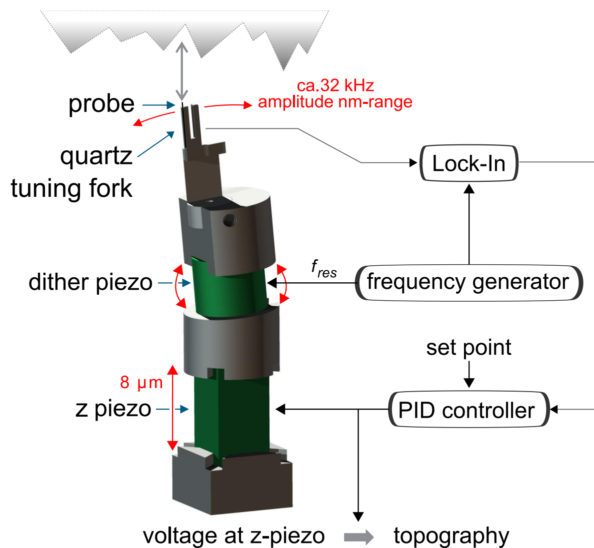

Figure 3.2: Shear-force distance control

An important component of the shear-force distance-control system is a quartz tuning fork (Fig. 3.2). It is widely used as frequency standard and due to the large industrial production available at very low cost [55]. The probe is clued to the quartz tuning fork (Chap. 4.3). A dither piezo induces an oscillation of the tuning fork and the attached probe at the effective resonance frequency ω_{res}. The piezoelectric effect of quartz allows to detect the oscillation fully electrically [55]. The alternating current through the tuning fork is converted to a voltage, amplified, and used as input of an lock-in amplifier. The

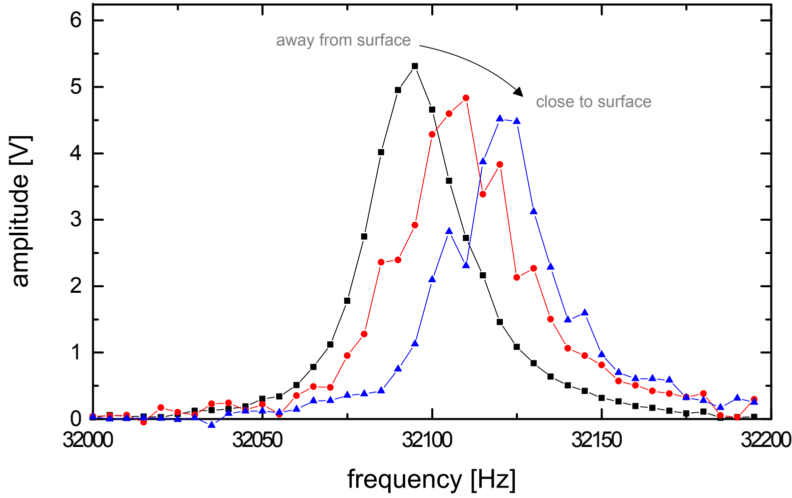

Figure 3.3: Shift of the resonance frequency upon approaching to the surface. The displacement is defined as a change in position towards the sample surface, starting from a distance outside of the range of shear-force. (The displacement is not equal to the sample-to-surface distance)

output voltage of the lock-in amplifier is proportional to the amplitude of the oscillation.

Upon approaching the sample, shear-forces (Chap. 2.6) between the probe and the sample surface decrease the oscillation amplitude, increase the resonance frequency, and cause a phase shift.[2]

Any of these three oscillation parameters can be used for distance control. Phase-locked shear-force detection tends to allow for the highest scan speeds [56, 57]. However, for investigations of light guidance in thin films, the scan speed is limited by the integration time of the detector, rather than by the distance-control system. Additionally, positive experience with an already existing system influenced the decision towards distance control based an a detection of the change in amplitude. A PID controller[3] compares the current amplitude with a set point and, as required, adapts the distance appropriately by applying a voltage at the z-piezo. The voltage at the z-piezo is proportional to the topography.

The microscope is not especially designed to measure distance dependent shear-forces. Nevertheless, it is feasible to measure resonance curves at different probe-to-sample dis-

[2] The range of shear-forces can differ for various reasons (Chap. 7.3). A decrease in the amplitude of the probe's apex, effectively increase the stiffness of the probe which leads to a higher spring constant. The resonance frequency ω_{res} is related to the spring constant k and the mass m by $\omega_{res} = \sqrt{\frac{k}{m}}$. Hence, an increase of the spring constant results in a higher resonance frequency.

[3] Proportional-Integral-Derivative controller

tances. Although relative movements of the probes can be accurately measured, it is not easy to determine the absolute sample-to-probe distance on a length scale beyond the resolution of the cameras. In the beginning of near-field microscopy, the distance control was realised by various approaches, based, for example, on the measurement of the tunnel currents. When shear-force distance control became common, a second independent system for measuring the absolute distance was still available at the microscopes. From this time, various paper exist about the distance dependence of shear-force [48, 56, 58, 59].

Despite the lack of knowledge about the absolute probe position, resonance curves are measured at different distances from the surface. The black coloured resonance curve in Figure 3.3 is measured at some distance to the sample surface. The actual probe-to-surface distance is not known but since the resonance frequency does not change upon small changes in the distance, it can be assumed that the start distance is outside of the typical range of shear-forces. The start position is defined as a displacement of zero. An increase of the displacement corresponds to a smaller distance between probe and surface. The resonance curve measured at the start position reveals a symmetrical shape and resembles a Gaussian distribution. Subsequently, the distance is decreased in steps of 5 nm and resonance curves are measured (Fig. 3.4). Closer to the surface, the resonance frequency increases and the amplitude slightly decreases. Additionally, the shape of the

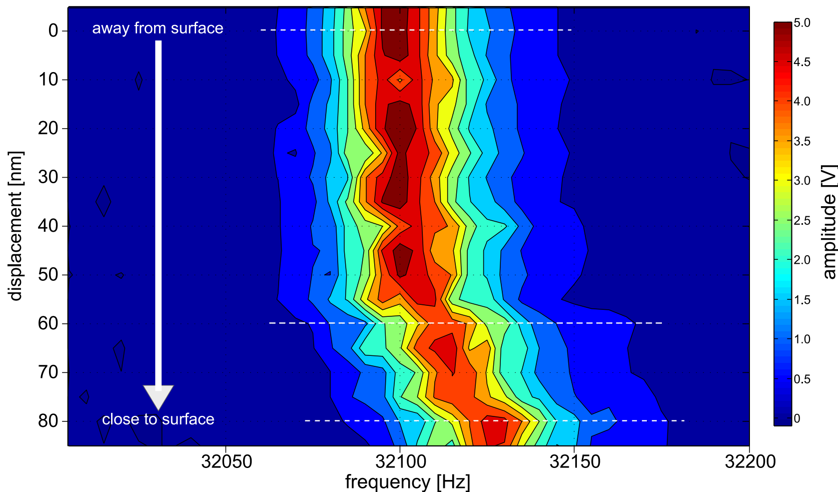

Figure 3.4: Contour plot of the shift in the resonance frequency of a dithered fibre during its approach to the surface. The start position is outside of the range of shear-forces and arbitrary chosen as a displacement of zero. The colours stand for the voltage at the output of the lock-in amplifier and are proportional to the oscillation amplitude. The white dashed lines refer to the displacement depicted in Fig. 3.3.

resonance curve is getting distorted. (The distance-control system is switched off for this measurement.)

Figure 3.4 reveals that the resonance frequency is shifted by about 20 Hz within a distance of slightly more than 20 nm. The results are in compliance with values reported in literature. Smolyaninov reports on a range of shear-force damping for metal coated tips in the order of 20 nm to 30 nm [48]. Additionally, Behme describes a shear-force distance control which reveals a shear-force range of 20 nm [60].

3.5 Cameras & Lighting

Operating a SNOM is not feasible without monitoring the probes position relative to each other and the sample surface. From the centimetre to the micrometre range, the position is monitored by several cameras. Unfortunately, the light conditions are critical for cameras. Due to the high magnification, necessary to image the small features, the light intensity is rather low. On the other hand, the sample is illuminated by lasers which cause high intensities on parts of the image. The camera software allows for limiting the automatic brightness control to certain parts of the image. A further difficulty are shadowing effects which occur in dual-probe measurement mode. The probe has to be placed in between the illumination unit (LED) and the camera. In dual-probe mode, the illumination units mutually block a free sight of the probes. A "x"-shape configuration of the cameras and the lightning LEDs prevents shadowing effects. Furthermore, this configuration has the advantage that no moving parts are involved. Displacing the LEDs mechanically out of the camera's field of vision has proven to cause too many vibrations.

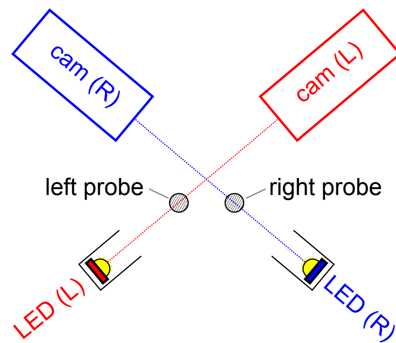

Figure 3.5: x-shape configuration of the cameras and the illumination unit

In addition to the two high magnification cameras (one for each probe), a third camera, mounted underneath the probes, monitors the coarse approaching of the probes to the surface and the distance in between the probes. A fourth zoom camera displays the sample surface and helps to position the probes relative to each other and surface markers. As soon as a probe is at close distance to the surface, no manual change in the camera position is possible, since touching the system in this state can easily destroy the probes. Therefore, motorised lens mounts adjust the field of view of the high magnification cameras which are essential for the last micrometre of the probe approaching process.

3.6 Vibration Isolation

The small gap of only 20 nm between the probe and the surface make vibration isolation a crucial factor in the design and operation of any near-field microscope. This setup implies two damping elements. The microscope is placed on an air cushioned optical table. Furthermore, the optical setup including lasers and various filters is placed on a separate optical breadboard, isolated by foam material from the microscope. This allows for an exchange of the neutral density filters while the probe is in the near-field of the sample surface. All devices with integrated cooling fans or transformers are not placed on top of the optical table. However, avoiding vibrations is difficult. Numerous cable connections between devices which have to be placed on the optical table (e.g. the piezo stages) and those which are banned due to vibrations (e.g. air-cooled power adapters) are inevitable. Furthermore, air vibrations have to be avoided and the air conditioning has to be switched off during measurements.

A detailed analysis of the vibration sources is accessible by placing one probe in the sample's near-field and recording the feedback-signal of the shear-force distance control without scanning above the sample. Theoretically, a rather constant feedback signal is expected since there is no relative motion between the probe and the sample surface. Any strong variations of a constant feedback signal are due to vibrations or electro magnetic noise (Fig.3.6). A Fourier transform of the recorded signal reveals the frequency

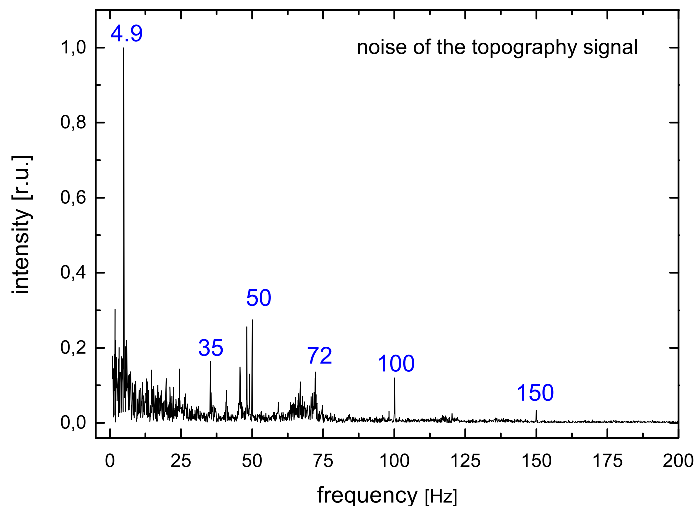

Figure 3.6: Noise of the topography signal, recorded during probe punching (Chap. 4.2.4). The signal at 4.9 Hz arise from the punching procedure. All other peaks are attributed to noise.

of the noise source. By this procedure noise sources like backing pumps of neighboured experiments and the influence of the air conditioning were identified.

3.7 Surface Markers

Surface markers are used whenever the absolute position on the sample surface is important (Fig. 3.7). With the help of markers, it is possible to combine the high topography resolution of an Atomic Force Microscope (AFM) scan with the optical information gained by a SNOM measurement of the same area. Although SNOM measurements provide topography information as well, the spatial resolution of a SNOM measurements is lower due to the larger apex diameter. The apex diameter of a SNOM probe is determined by the size of the aperture and the coating thickness. The aperture needs to have a size of at least 50 nm to allow for a reasonable optical throughput. A certain coating thickness is essential to ensure the optical confinement of the light inside the probe. Probes designed for atomic force microscopy do not have to consider optical issues. Consequently they commonly have a sharper apex and provide higher resolution. The advantages of SNOM and AFM measurements can be combined by applying both methods at the same measurement field. Thereby, the topography measured with the SNOM probe is only used to align the AFM measurement with higher resolution. This way, simulations based

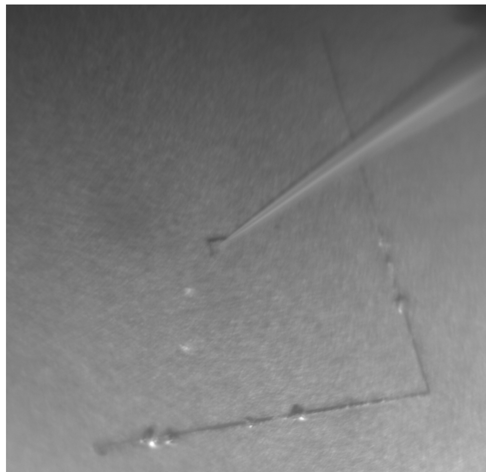

Figure 3.7: SNOM probe close to a L-shape sample marker applied for defining an absolute position on the samples surface. (The "large L" marker has a size of 5×5 mm and is visible with the bare eye. The small marker has a size of 5×5 µm and is used for a fine alignment.)

on the topography determined by an AFM measurement, can be compared with SNOM measurements of the same sample area.

Furthermore, surface markers are used for the alignment of the probes towards each other. This probe alignment process is described in Chapter 5.2.

3.8 Laser & Optical Setup

In total, six solid state lasers with wavelengths between 473 and 750 nm are used simultaneously. In general, the requirements for the lasers are rather low. They need to have a laser power in the order of 20 to 200 mW. Higher laser powers are not beneficial, since the illumination probe is specified for a maximal power input of 10 mW. Slightly higher laser powers are chosen to compensate for losses at the mirrors and dichroic filters, used to align the different laser beams to the fibre coupler (Fig. 3.8). The fibre coupler is designed for being used at a single wavelength only. Consequently, the coupling efficiency can only be optimised for a single wavelength, whereby the attenuation at other wavelengths has to be compensated by higher laser power. The direction of the laser emission has to be stable because any change in the laser beam position at the glass fibre coupler strongly change the coupling efficiency. Furthermore, the laser power needs to be temporal stable, although small variations are acceptable in relation to a change in intensity of several orders of magnitude during a measurement. The time stability of the applied lasers after 15 minute operation is better than 5 % during 20 hours.

3.9 Detector & Lock-In Technique

The light collected by the detection probe is guided to a GaAs-photomultiplier tube (PMT)[4]. The PMT is operated at 1800 V. The quantum efficiency is between 23 and 7 % for the wavelength spectrum from 300 to 800 nm. The detector is equipped with a peltier cooling which is in turn water cooled. At low temperature, the detection limit is 500 photons per second. The lowest detection threshold is reached at the photon-counting mode. In this mode, the signal from the detector is directly fed into an electronic assembly which counts each pulse from the detector that exceeds a certain threshold (Fig. 3.8). Additionally, there is no need for a modulation of the lasers which slightly increases the available laser power. However, the photo-counting mode is limited to a single-wavelength operation. An optically opaque housing allows for performing standard measurement under room light conditions.

[4] Hamamatsu 650S

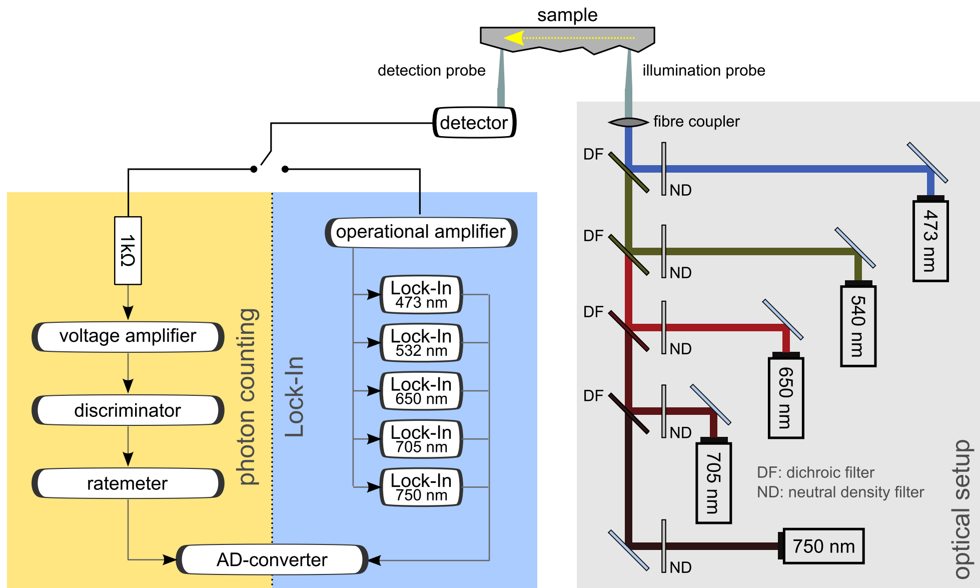

Figure 3.8: Illustration of the optical setup. Multiple laser beams are coupled into the glass fibre of the illumination probe. The light collected by the detection probe is guided to a detector. The detection electronics offer two modes of operation. A *lock-in mode* can handle multiple wavelength simultaneously. At very low intensities, the *photon-counting mode* is applied. In this case, only one laser is operated at the same time.

3.10 Estimate of the Maximal Distance in between the Probes

As mentioned above, the detector has a certain limit for the lowest detectable light intensity. The detection limit of the detector corresponds to about 500 photons/s. On the other side, in dual-probe mode, the maximal allowed laser intensity is limited by the thermal threshold of the illumination probe. The probes are specified for a maximal optical power of 10 mW which corresponds to about 4×10^{16} photons/s.[5] (topmost dashed line in Fig. 3.9) The difference in between the available photon rate and the detection limit might appear tremendous at the first glance. However, the light needs to pass the illumination probe and thereby loses five orders of magnitude in intensity. Hence, only 4×10^{11} photons/s actually reach the sample. A similar situation applies at the detection probe. If at least 500 photons/s are supposed to reach the detector, five orders of mag-

[5] Within the regarded spectral range, the small wavelength dependence of the number of photons which corresponds to a certain optical power, is neglected in this coarse estimate.

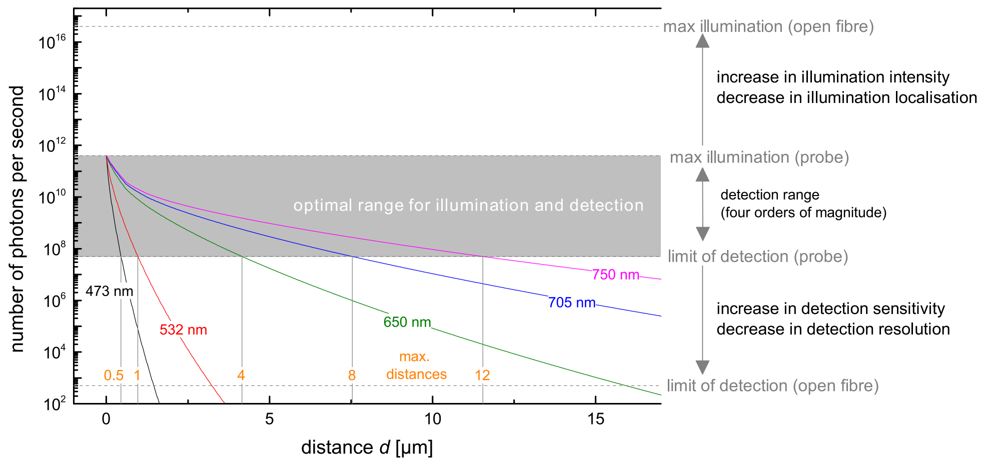

Figure 3.9: Estimate of the maximal distance between illumination and detection probe in case of light propagation in a μc-Si:H layer. The maximal distance is displayed for selected wavelength.

nitude more photons have to reach the detection probe. Hence, an intensity threshold of 5×10^7 photons/s at the position of the detection probe applies. If the illumination and the detection probe are placed at zero distance, 4×10^{11} photons/s are available from the illumination probe, whereas only 5×10^7 photons/s are needed for the detection. Correspondingly, the probe-to-probe distance can be increased until the photon rate at the detection probe is declined by about four orders of magnitude.

The photon rate at the detection probe decreases due to several loss mechanisms which are discussed in more detail in Chapter 6. Some loss-mechanisms are wavelength dependent. Therefore, the distance, at which the photon rate deceeds the detection limit, strongly depends on the wavelength. At a wavelength of 473 nm, the required photon rate at the detection probe is deceeded, as soon as the distance between the probes exceeds 0.5 μm. Hence, it is not feasible to detect the propagation of light in μc-Si:H at a wavelength of 473 nm at a distance larger than 0.5 μm. The absorptivity in μc-Si:H decreases for longer wavelength, increasing the maximal distance between the probes to a level at which it is experimentally accessible.

Nonetheless, the detection range can be increased to a certain extend. The listed maximal probe-to-probe distance, illustrated in Figure 3.9, applies for perfect probes with an aperture size of about 50 nm. An increase in aperture size significantly increases the optical throughput for the price of decreased resolution. The highest optical throughput is achieved by a completely open bare glass fibre without tapered apex. If such a fibre is used as illumination probe, the light intensity is strongly increased (topmost dashed

line in Fig. 3.9). However, any reasonable information about the source of illumination is lost in this extreme case. On the other side, the aperture of the detection probe can be increased as well, even so this decreases the resolution (lowest dashed line in Fig. 3.9). For practical purpose, a trade-off between reasonable aperture size and resolution is essential.

The maximal distances listed in Figure 3.9 are based on a ray-tracing simulation (Chap. 8.1) which includes reflection losses at a flat front interface, absorption, and the decrease of intensity due to a distribution of the light inside the layer (Chap. 6). Further loss mechanism like scattering at impurities at the sample surface may apply which will decrease the maximal achievable distance between the probes. Therefore, the given distances are upper limits for the maximal probe-to-probe distance.

Performing dual-probe measurements is experimentally less challenging in case of low absorptance and correspondingly long maximal distances between the probes. Fortunately light trapping gains more significance in the wavelength regime of low absorptance as well. Hence, the wavelength regime which is of most importance for light-trapping is also the one which is comparatively easy accessible by dual probe measurements.

4 Optical Probes for Near-Field Microscopy

Optical probes are a key component of near-field optical microscopes [14]. Hence, a wide range of different probe designs exist which are primarily based on two different concepts, namely probes with and without aperture. The way optical probes are manufactured has a strong influence on the optical properties. Although the probes used within this thesis are commercially available, the two most common ways of probe manufacturing are briefly outlined. The ability to adjust the aperture size is crucial, in particular in dual probe operation. Both, a rather straight forward method of aperture punching and a highly precise focus ion-beam treatment are described. Prior to any measurements the probes have to be prepared. The probe preparation, as well the subsequent characterisation of the optical properties, are outlined in the end of the chapter.

4.1 Apertureless Probes

Apertureless SNOMs apply a tiny scattering point at the apex of a solid metal probe for a local field enhancement. The probe scatters light from the near-field of the sample to a detector. Since the light is not guided through a waveguide, the wavelength is not limited by the optical properties of the waveguide material. Furthermore, the tiny apex allows for a high spatial resolution. However, apertureless SNOMs are limited to near-field operation. Additionally, they are not suitable for the considered measurement of light propagation in thin films.

4.2 Aperture Probes

A conceptually different approach are aperture probes. This kind of probe consists of a metal coated glass-fibre with a tapered apex. A small area at the probe's apex is not coated, forming an aperture in the size of about 50 nm. The probe can be used as local collector or local source of illumination. Choosing an aperture SNOM implies the necessity to form a subwavelength size aperture at the apex of a glass fibre. The major

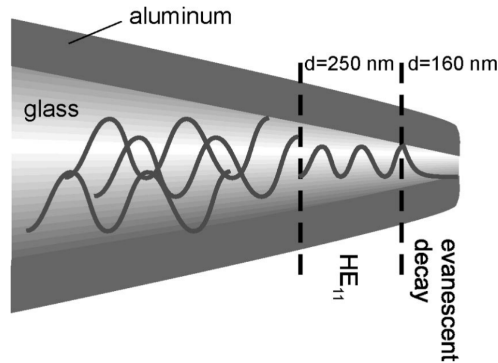

Figure 4.1: Mode propagation in a tapered metal-coated optical fibre at a wavelength of 488 nm. [14]

challenge is to meet two completely contrary requirements. On the one hand, a high optical resolutions is a prerequisite to meet the scientific demand. On the other hand, a reasonable optical throughput is experimentally preferable.

Probes with large cone angles and sharp apex best satisfy the requirements. A large cone angle considerably reduces the part of the probe which has a sub-wavelength diameter and therefore causes a lower attenuation (Fig. 4.1). Regarding a probe with 50 nm aperture, the light is typically attenuated by five orders of magnitude in the visible range, i.e. only one of 10 000 photons passes the aperture. An additional restriction addresses the use of probes in dual-probe operation.

The applicability for dual-probe operation implies that two probes can approach each other as close as possible. A further restriction relates to the simplicity of probe manufacturing in large quantities. If the research project is mainly restricted to the physical properties of a probe itself, huge efforts are feasible for the manufacturing process. If probes are rather regarded as expendable items which have to be replaced on a regular basis, the ease of fabrication is of strong importance.

Additionally, the reproducibility of the probe manufacturing process is a major concern. Since the influence of the probe itself on the measurement is still not completely understood, it is as much more important to ensure that changes in the measured fields are actually due to changes of the investigated samples, rather than due to a change of the probe used for the measurement. A strong convolution of sample and probe properties renders an analysis of the experimental data impossible. There are mainly two ways to produce aperture probes in large quantities and high reproducibility. Both start with an ordinary commercially available, single-mode glass fibre. The choose of the fibre depends on the wavelength of interest. The aim of both manufacturing procedures is to create a taper at the end of the fibre.

4.2.1 Probe Etching

One way to achieve a taper at the end of the fibre is chemical etching. The protection layer method (known as "'Turner Method" [62]') uses the interface between a layer of 40 % aqueous hydrofluoric acid covered by an organic solvent to form the taper of the probe (Fig. 4.2). Taper formation takes place because the height of the meniscus is a function of the diameter of the remaining cylindrical fibre. Since the fibre diameter shrinks during etching the meniscus height is reduced, thus preventing higher parts of the fibre from being etched [14]. The cone angle can be varied from 8° to 41° by the adequate choice of the organic solvent [61]. The point diameters are below 40 nm. Although the large cone angle and the small point diameter are promising, the protection layer method has the major drawback of rough surfaces. Rather than moving continuously, the applied hydrofluoric acid meniscus jumps between stable positions, causing an uneven etching of the taper. Rough surfaces hamper the metallisation of the probes, reduce the maximal applicable laser power and causes protrusions at the probe's apex which increase the minimal probe-to-surface distance. Etching without cleaving the fibre cladding (tube etching [63]), reduces the surface roughness.

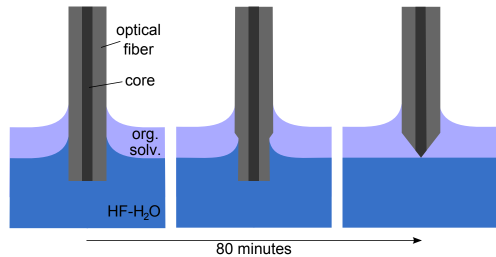

Figure 4.2: Probe Etching [61]

4.2.2 Probe Pulling

An alternative approach for probe formation is mechanical drawing with a commercial micropipette puller. A preheated stripped glass fibre is locally heated with a CO_2 laser or a filament while a pulling force is applied (Fig. 4.3). The fibre core decreases in the taper region due to the drawing process [61]. Variable parameters are mainly the pulling speed profile, the size of the irradiated area and the heating time profile [14]. A key difference of pulled fibres is, that in contrast to etched fibres, the fibre core decreases (non-linear) over the whole range of the taper [61]. This results in lower optical throughput and can cause further complications like unfavourable mode distortion [14] and a high degree of polarisation in one particular direction [64] which can even be time dependent due to relaxation processes [65]. The cone angle, which is typically be-

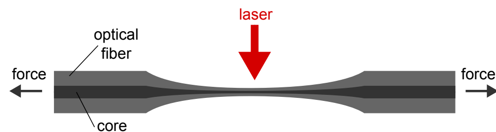

Figure 4.3: Probe Pulling

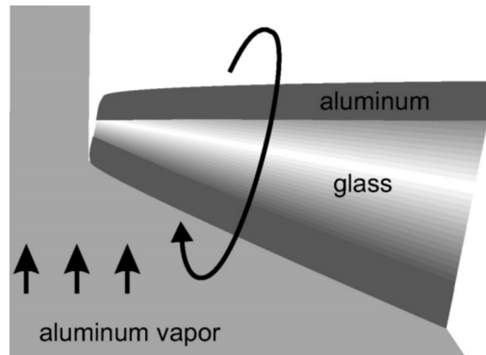

Figure 4.4: Evaporation geometry of the aluminium coating process. The probe is slightly tilted and rotating during the evaporation process. The deposition rate of metal at the apex is much smaller than on the side walls [14].

low 15°, is smaller than for etched probes. Besides this drawbacks, pulled probes offer a good reproducibility in fabrication [64], a sharpness down to 20 nm [64], and little surface roughness [14]. The probes used in this work are pulled probes.

4.2.3 Coating

No matter, whether the probe is used as a local source of illumination, a local collector, or both, the optical spatial resolution strongly depends on the confinement of the optical energy at the apex of the probe [14]. Hence, the fibre is coated with a thin metallisation layer, subsequent to the taper formation by etching or pulling (Fig. 4.4). Typically, aluminium is used for the coating because is has the smallest skin depth in the visible spectrum among all metals [14]. Preferably, thermal or e-beam evaporation is used for the metallisation, since sputtering suffer from the tendency that aluminium forms rather large grains, causing a leakage of light at the grain boundaries [14].

No matter, if the probes are produced by one way or the other, a high reproducibility in fabrication is only achievable by well established and approved processes. Therefore, the probes used within this work were purchased from a commercial vendor. Only very few companies offer SNOM probes which are not limited for the use in a specific commercial microscope of a certain company. Various probes from different vendors were tested and the final decision was made mainly on the ability to change the aperture size.

4.2.4 Aperture Adjustment

The aperture size is a crucial element of a probe, determining its optical throughput and the resolution. A high resolution is always desirable, especially when measuring

evanescent fields. However, in dual-probe operation, the light has to pass the aperture of the illumination and detection probe which can therefore not be too small. Several probe post processing procedures allow for an adjustment of the aperture size, at least in the direction of larger sizes. Aperture formation by ion beam milling offers a precise control over the aperture in size and even over its shape. Figure 4.5 shows a SEM[1] image of a probe before and after FIB[2]-processing. Although FIB is a powerful tool for detailed probe formation, it is hardly suitable for preparing a large number of probes. Mounting a fragile probe with 2 m attached glass fibre in a FIB-system is time consuming and always involves the risk that the probe is damaged during the mounting or demounting process. The damages are not necessarily visible with the bare eye and might be apparent not until the probe is mounted to the SNOM system and the first measurement is performed. An additional difficulty is induced by the magnetic fields of the FIB-system. Usually, the probes have passed several standard tests before they are chosen for a FIB-treatment. The tests require the probe to be glued to a quartz tuning fork. The metal parts of the tuning fork are attracted by the magnetic fields which are switched on when the FIB-system is operated in high resolution mode and bend the probe until it touches parts of the FIB system and is destroyed. Therefore, the probe needs to be fixed in a specially build holder during the FIB treatment.

Despite the extensive capabilities of FIB, a fast and easy to use procedure for aperture

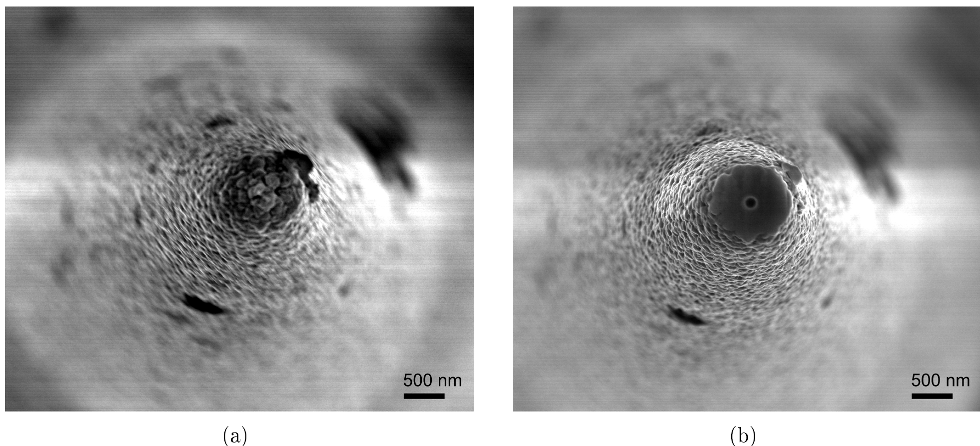

(a) (b)

Figure 4.5: (a) SEM image of an unused SNOM probe with Au/Cr coating (The probes used for the measurements presented in Chapter 7 are aluminium coated and have a much smoother surface) (b) FIB processed SNOM probe

[1] Scanning Electron Microscope
[2] Focused Ion Beam

size modification is required. Aperture punching is less controllable than ion beam milling, but fast and applicable to probes that are already mounted to the SNOM system. The aperture is formed by slightly touching the surface with the probe. The punching effect is boosted by applying a 5 Hz rectangular signal to the probe's distance-control system which induces a 200 nm oscillation of the probe towards the surface. During the punching process the aperture size is controlled by measuring the optical throughput of the probe. Therefore, a transparent sample is used which is illuminated in transmission mode. However, aperture punching is not feasible with all kind of probe coatings. Au/Cr coatings have such a high degrees of hardness that they can not be removed by punching. The probes used for this work have an aluminium coating and are suitable for the punching process.

4.3 Probe Preparation

Various steps are applied to prepare a SNOM probe which are displayed in detail in Figure 4.6 and summarised in the following.

An essential part of the near-field microscope is a quartz tuning fork. Subsequent to some prearrangement steps, the tuning fork is glued on top of a glass holder which mechanically connects the tuning fork to the dither piezo. The glass holder with the attached

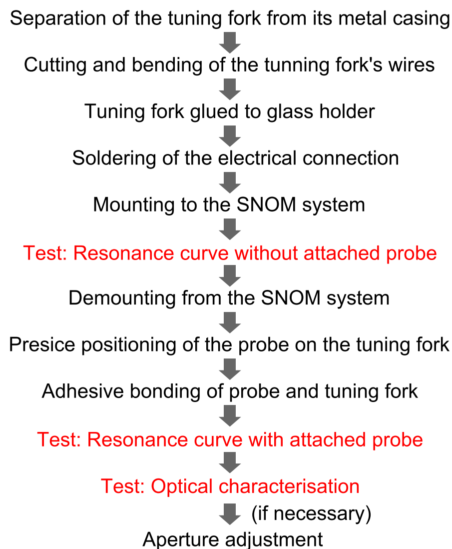

Figure 4.6: SNOM probe preparation flow chart. Several tests ascertain high quality probes at the end of the preparation.

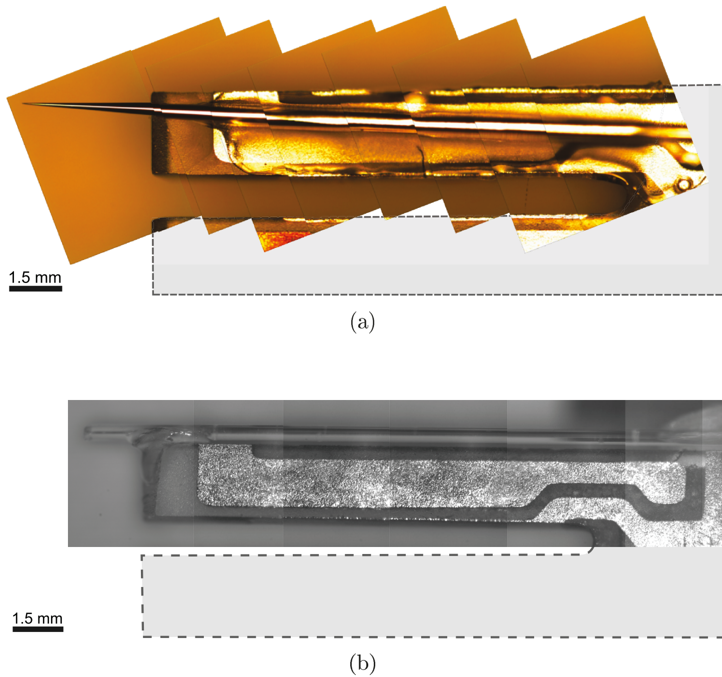

Figure 4.7: Probe clued to the upper plane (a) or lateral plane (b) of a quartz tuning fork. Different adhesive bonding techniques are applied. In (a) the adhesive surface between probe and tuning fork is large, promising a good transfer of the shear-forces for the price of an increased disturbance of the oscillation. In (b) only the outermost part of the tuning fork is connected with the glass fibre. (The probe displayed in (b) is only a bare glass fibre for testing purpose.)

tuning fork is mounted to the SNOM system to perform a resonance test. Therefore, the frequency of the dither-piezo passes through a frequency range of about 200 Hz, centred around the expected resonance frequency of the tuning fork. The oscillation induces an alternating current at the tuning fork which is proportional to the amplitude of the oscillation. If the tuning fork is fixed properly on top of the glass holder and no glue has flown in between the fork's tines, the amplitude will meet a certain threshold and the resonance curve will reveal a sharp peak.

q-Factor The full width at half maximum of the resonance peak, in relation to the resonance frequency, is referred to as *quality factor*, or briefly *q-factor*. The q-factor is a measure of the stored energy of an oscillating system in relation to the energy loss per cycle [66]. A high q-factor stands for an oscillator with low damping. A system with low internal damping is highly sensitive to external forces. Hence, in terms of sensitivity, high q-factors are beneficial. However, as soon as the glass fibre is glued to one of the tuning

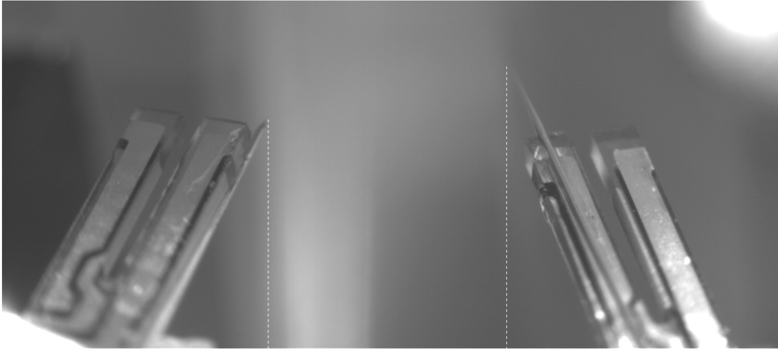

Figure 4.8: Image of two probes glued to quartz tuning forks and mounted to the SNOM system. The probes are tilted to allow for an approaching of the probes.

fork's tines, the additional mass and stiffness of the fibre strongly disturbs the symmetry of the tuning fork and reduces the q-factor. Commercially available micro-tuning forks have q-factors in the range of $Q = 5 \times 10^4 - 20 \times 10^4$ in vacuum and $Q \approx 1.5 \times 10^4$ in air [67]. The q-factor of tuning forks with attached glass-fibre decreases to about 100 - 1700 [67–69].

The key for a properly working distance control is, to attach the probe to the tuning fork by maintaining a high q-factor. In an ideal case, the oscillation of the tuning fork is only influenced by forces proportional to the probe-to-sample distance. However, attaching the fibre to the tuning fork is always a trade-off between disturbing the tuning fork as little as possible and ascertain a sufficiently high transfer of the shear-forces on the tuning fork.

Not all tuning forks are suitable for being used in near-field microscopy. Besides the size and the resonance frequency of the tuning fork it is essential, that they remain operating with attached glass fibre. Extensive tests were performed to find suitable tuning forks. A change in the production process of the manufacturer might not effect the resonance frequency or the q-factor of a tuning fork. However, it can indeed have strong effects on the oscillation properties with attached probe.

Different configurations of probe position were examined. The tests reveal that it is equally possible to glue the probe to the upper plane or lateral plane of the tuning fork (Figure 4.7). One way or the other, it has be ascertain that the left and the right probe can theoretically touch each other in dual-probe operation (Figure 4.8).

If all resonance tests are passed, the probe is optically characterised as described in the following chapter. In case the optical throughput does not meet the demand for the considered measurement, the aperture size might be adapted (previous chapter).

4.4 Probe Characterisation

Some dual-probe measurements with stationary illumination probe and scanning detection probe on flat, non-textured samples reveal that the light does not propagate radial symmetrically around the illumination probe. Most likely, this is due to not perfectly circular apertures of the illumination- and/or detection-probe, i.e. the illumination probe's sensitivity and/or the illumination probe's radiation profile is anisotropic. In order to avoid or at least to know the influence of a probe's beam characteristic on a measurement, each newly mounted probe needs to be characterized preliminary to the first measurement.

The ultimate goal of probe characterisation is to know the sensitivity or radiation profile, on all relevant scales from the near-field to the far-field. Holding this knowledge, it might even be possible to correct the experimental data for any influence of the probe's anisotropy. However, a measurement of the near-field emission or detection profile is difficult and hardly feasible on a regular basis preliminary to measurements. The experimental determination of the near-field coupling of a SNOM probe is in particular difficult to determine, because it depends on the properties of the surface material in close distance to the aperture. Hence, instead of being an intrinsic property of a certain probe, the near-field emission and detection profile correlates with properties of the illuminated surface and the distance in between the surface and the probe's aperture. Therefore, the decision of whether or not to use a certain probe is based on its far-field characteristic.

As a first approach, a fast and easily applicable method for probe far-field characterisation is presented in the following section. Besides a specially designed sample holder, it mainly uses hardware and software that exist anyway at an aperture SNOM. The probe does not need to be disassembled from the SNOM for the characterisation which makes it easy to characterise the probe whenever necessary even in between measurements. The characterisation method is based on measuring the beam profile of an illumination probe.

In first approximation and with reference to the reversibility of light paths, it can be assumed that if a probe radiates light preferably in a certain direction, it will show the same anisotropy in its detection sensitivity. If this is the case, the measurement of the radiation profile of an illumination probe will provide information about its direction dependent detection behaviour as well. To put it another way, if a probe operated as illumination probe, has a highly anisotropic beam profile, there is no reason why it should have a perfectly isotropic detection sensitivity if later on operated as detection probe. Hence, the isotropy of the beam profile is a criterion for using or not using a probe for measurements.

To determine the beam profile of a SNOM probe, a specially designed sample holder is used. The sample holder is equipped with a CMOS chip at the position where usually

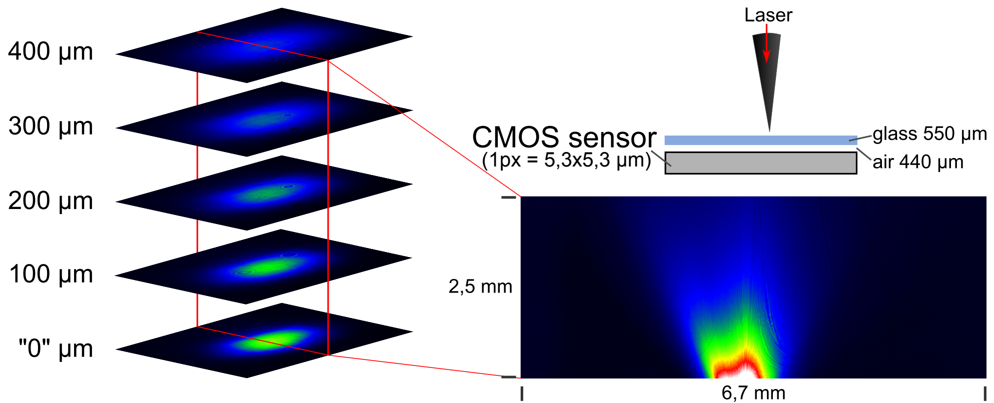

Figure 4.9: Optical probe characterisation. A CMOS chip is illuminated through the aperture of a SNOM probe. The probe is stepwise retracted while an image of the probe emission is taken at each height step. With the help of an analysis software, cross-sectional images are created.

the sample is placed. The probe is positioned above the centre of the CMOS chip, close to the chip's surface. The CMOS chip is illuminated with a laser coupled into the glass fibre. Since there is no absorptive medium in between the probe and the CMOS chip, the laser power usually needs to be adapted by neutral density filters to avoid a saturation of the CMOS chip. During the beam profile measurement, the probe is stepwise retracted from the CMOS chip while a photo is taken at each height step (Fig. 4.9). Approved settings are a step height of 5 µm and 500 steps in total resulting in a height profile of 2.5 mm. Each photo has a resolution of slightly more than a megapixel whereby the actual pixel size is 5.3×5.3 µm. Hence, a dataset with more than 500 million data points needs to be analysed. A specially for this purpose developed analysis software calculates cross-sectional images in arbitrary directions.

In Figure 4.9, the bottommost photo is captioned with "0 µm". Of course, it is not possible to actually take a picture of the probe's beam profile at zero distance. The sensor area of the CMOS chip is protected by a glass window which is placed at some distance to the chip's surface. The gap in between the chip and the glass window in addition with the thickness of the protection glass prevent the probe from approaching closer than about 1 mm to the sensor area. Although it might be possible to remove the protection glass, a photo of the beam profile can only be taken if a couple of pixels are illuminated simultaneously. The pixel size limits this method to the far-field.

The beam profile for a given probe depends on the wavelength (Fig. 4.10). Consequently, the beam profile characterisation needs to be performed for all laser wavelengths separately. Since the beam-profile measurement is completely automatised, only the lasers

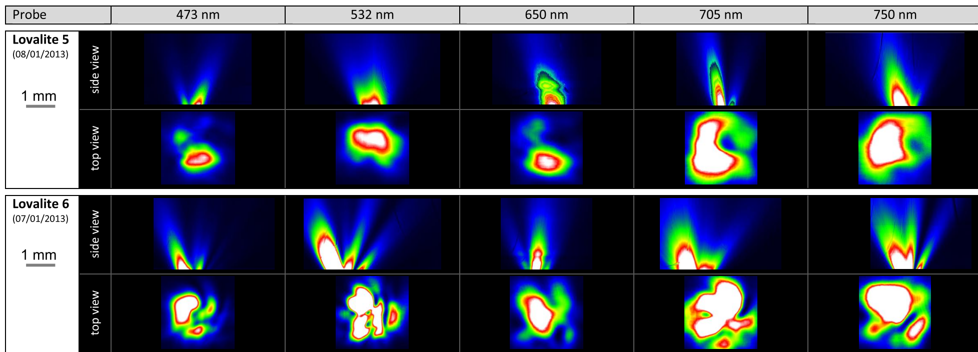

Figure 4.10: Beam profiles of two different probes. The probe named Lovalite 5 reveals a basically isotropic beam profile. In contrast, the beam profile of the probe Lovalite 6 is highly anisotropic.

have to be switched and the intensity has to be adapted with the neutral density filters to get the wavelength dependent beam profile. The probe named "‘Lovalite 5"’ in Figure 4.10 is an example for a probe with comparatively isotropic beam profile. The intensity is mainly concentrated in a single beam, although the profile for 473 nm and 705 nm reveal small side lobes. The "‘Lovalite 6"’ probe features multiple lobes for more or less all wavelengths.

Dual-probe measurements imply that the intensity at a certain measuring point depends on the radiation profile of the illumination probe, the sensitivity profile of the detection probe and, therefore, on the distance and angle between both probes. Furthermore, probe properties depend on the operating time. Despite a distance control, which theoretically avoids any contact between the probe and the surface, the probes show abrasive wear after long term usage which slightly increases the optical throughput. This demands even more for a fast and easy to use characterisation method.

5 Modes of Operation

A SNOM, especially one equipped with two probes, offers a variety of measurement modes. This chapter outlines the different modes of operation, from basic modes to more sophisticated modes which are exclusively available at dual probe SNOMs.

5.1 Basic Modes of Operation

The two basic modes of operation, which are often found in literature, are *collection mode* and *illumination mode*. Collection mode refers to a configuration in which the probe detects the light in near-field while the source of illumination is placed in the far-field. Alternatively, the source of illumination can be placed in near-field and the detection takes place in the far-field which is referred to as illumination mode. Furthermore, it is distinguished if the light is transmitted through the sample (transmission geometry) or reflected at the sample's surface (reflection geometry). Instead of using an external source of illumination it is also feasible to detect light emitted by the sample itself due to photoluminescence or electroluminescence [70].

5.1.1 Collection Mode in Transmission Geometry

The collection mode in transmission geometry is the most simple mode of operation. The sample, which needs to be transparent, is illuminated from the rear side while the detection probe measures the transmitted light intensity at the front side (Fig. 5.1). Since the sample is directly illuminated by a laser, the power of the irradiating light is not limited by the maximal power rating of an illumination probe. If the sample is highly transparent, a high intensity of light reaches the detection probe. This allows for very small probe apertures in the 50 nm range, offering a high resolution.

The illumination through a glass substrate resembles the usual mode of illumination in a solar cell. Performing SNOM measurements in between the different deposition steps of a solar cell, allows for investigating the optical properties of the different layers separately. In particular, this mode of operation is used to investigate the scattering behaviour of textured transparent conductive oxides [11, 71, 72].

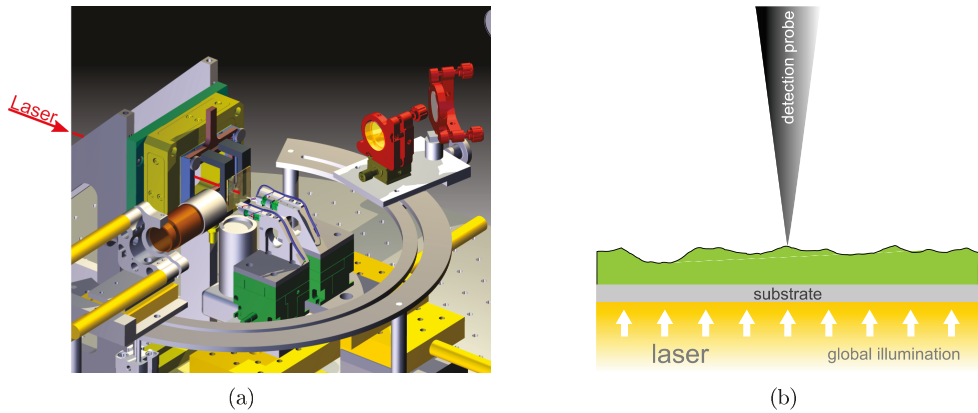

(a) (b)

Figure 5.1: Illustration of the transmission geometry. The sample is illuminated from the rear-side while the transmitted light intensity is measured at the front side.

5.1.2 Collection Mode in Reflection Geometry

In reflection geometry, the illumination, as well as the detection, take place at the same side of the sample (Fig. 5.2(b)). Usually, this mode is used in single-probe operation. Therefore, the entire assembly group of a probe, which is not needed for the considered measurement, can easily be demounted. This way, the illumination laser can reach the sample surface at different angles, covering almost the whole range from $\pm 90°$ to the

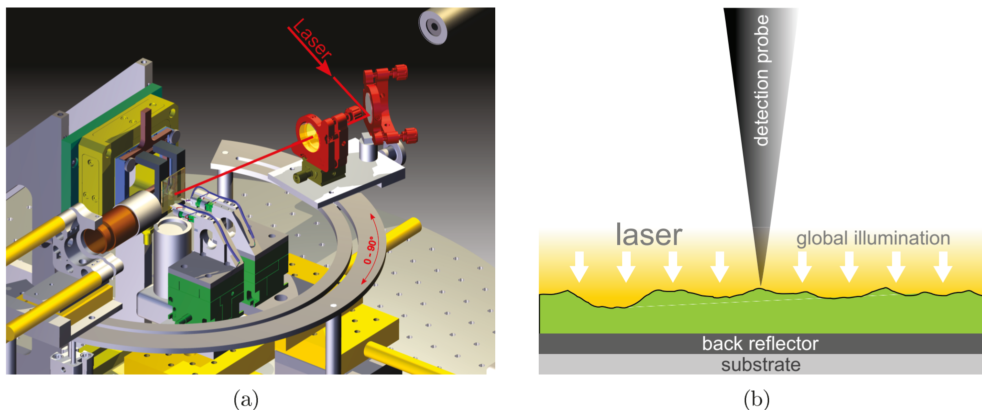

(a) (b)

Figure 5.2: Illumination and detection at the front side of the sample in reflection geometry (b). The angle of incidence is adjustable, as illustrated in (a). If neccessary, one of the probe assembly groups is demountable.

normal (Fig. 5.2(a)). Although the measured raw data only contain information about the light intensity of each measured pixel at the sample surface, the angular distribution of light is accessible by Fourier transformation [73, 74].

5.2 Dual-Probe Mode

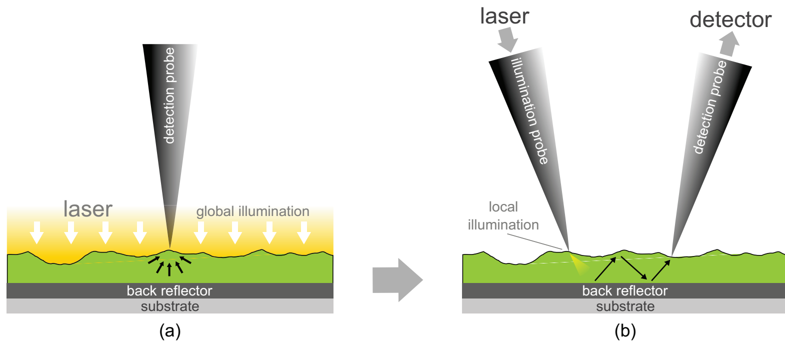

Figure 5.3: Transition from global illumination in single-probe operation (a) to a local illumination in dual-probe mode (b).

In transmission as well as in reflection mode, a sample area larger than the measurement area is homogeneously illuminated from the far-field. Consequently, the probe collects light from various sources. Hence, the experimental data solely contain information about the total light intensity at each measured pixel. The origin of the light intensity at a certain position remains unknown (Fig. 5.3 (a)). In dual-probe mode, the global illumination from the far-field is replaced by an illumination probes which illuminates the sample on a local scale. Simultaneously, an additional detection probe measures the light intensity at the sample surface at some distance to the illumination probe (Fig. 5.3 (b)). Various different kinds of dual-probe scanning modes are feasible. In the most straightforward scenario, the illumination probe is placed at a constant position while the detection probe scans the area sidewise of the illumination probe. Alternatively both probes are positioned at a constant distance while the sample is moved.

In all dual-probe measurement presented in this thesis, the left probe is chosen to be the illumination probe. However, the probes are structurally identical and any of them can be used as illumination or detection probe. More over, it is imaginable to use different kinds of probes for measuring different kinds of physical properties, not even necessarily limited to optical properties (⇒ Outlook, Chap. 9).

5.2.1 Alignment of the Probes

Dual probe measurements require an accurate alignment of the SNOM probes. The light emitted by the illumination probe is strongly attenuated when passing through the investigated µc-Si:H layer (Chap. 3.10). Hence, illumination and detection probe have to be placed in close distance of a few micrometer. The coarse alignment is controlled by cameras (Chap. 3.5). The fine alignment demands for a surface feature with sharp edges. Initial experiments to align the probes at silver grids, commonly used to contact solar cells, failed, because the steepness of the grids is not sufficient[1]. Surface markers scribed by a focus ion beam or a laser offer sufficiently sharp edges for probe alignment (Figure 5.4(a)). The topography along a line, crossing the surface marker, is scanned by both probes. The shift in the measured topography profile corresponds to the distance between the probes in the scanning direction (Fig. 5.4(b)). By scanning across the surface marker in x- and y-direction, the distance in between the probes can be determined and adapted.

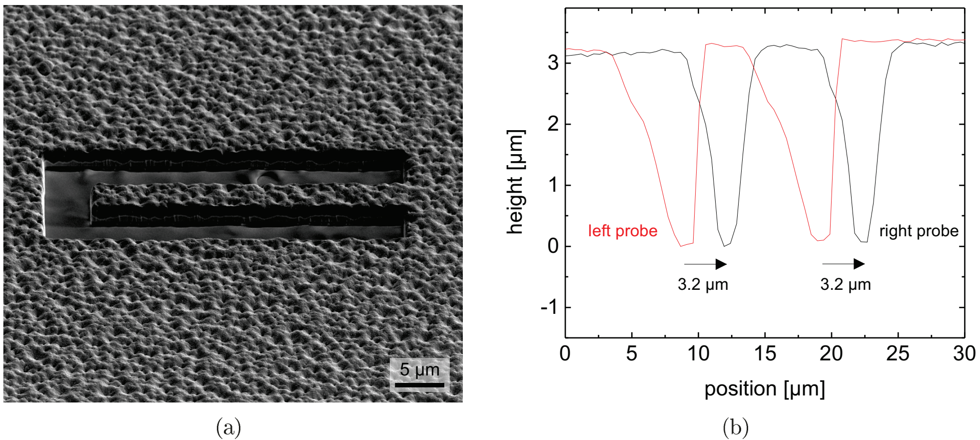

(a) (b)

Figure 5.4: (a) SEM image of a U-shape sample marker created by FIB treatment (b) Shift in the topography between left and right probe used to measure and adapt the probe-to-probe distance

[1] Although the grids appear to have sharp edges when observed with the bare eye, the height of the silver grids actually increases along a distance of about 100 µm. Hence, instead of a sharp edge, a SNOM measurement of standard size (10×10 µm), reveals only a slightly tilted topography which is not suitable for probe alignment.

5.2.2 Interaction between the Probes

In dual-probe operation, the illumination and the detection probe operate at close distance. If the distance becomes too small, the probes interact. The distance-control system is designed to react to any change in the forces interacting on the probe by retracting the probe from the surface until the oscillation amplitude meets a certain set point (⇒ Shear-force distance control Chap. 3.4). Hence, the probe will react to an interaction with the second probe like to any other interaction with a surface feature. Consequently, the topography data measured by the scanning probe reveals a steep hill at the position of the second probe. Vice versa, a probe which is supposed to remain at a constant position, shows a constant topography signal during usual operation. In case the scanning probe gets too close, a hill in the topography is apparent which is in fact the scanning probe (Fig. 5.5).

The change in the topography signal of the stationary probe is used to stop the measurement and to prevent a potential damage of both probes. At usual scan speeds of about 1 μm/s, no damage of the probes is observed, if they slightly touch each other. However, the probe retraction from the surface is realised by a piezo which has a limited range (Chap. 3.4). If the overlap of the probe's position gets too large, the scanning probe can not be retracted far enough and the probe(s) will be damaged.

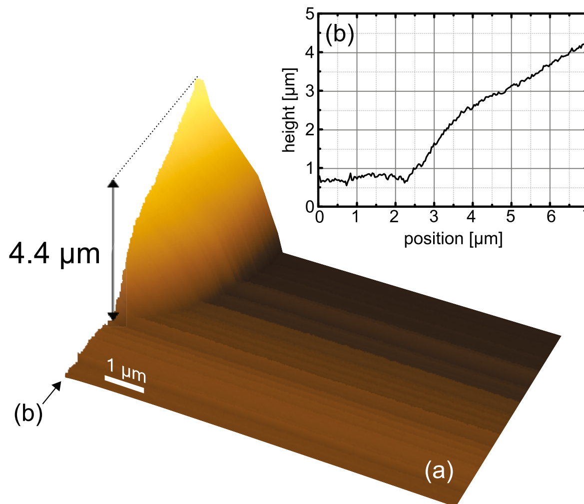

Figure 5.5: (a) Topography image measured with the left (stationary) probe at close distance to the right (scanning) probe. The steep hill on the left originates from an interaction in between the probes. A line scan along the edge of the measurement field is shown in (b).

To distinguish between an interaction with the sample's topography and an inter-probe-interaction, Klein suggests the use of a dual-band modulation (DBM)[75]. This technique applies tuning forks with different fundamental eigen modes. The interaction between the probes is detected by analysing the response signal of one probe with a lock-in amplifier locked at the frequency of the other tuning fork. The response signal increases prior the topography signal which allows for measurement at short probe-to-probe distance. Nonetheless, dual-band modulation is not capable of avoiding major crashes at high scan speeds. A further drawback of using tuning forks with different eigen modes is that they most likely react differently to interactions with the sample surface. Hence, the results may depend on the applied tuning fork which contradicts the concept of structurally equal probes. Therefore, dual-band modulation is not applied within this thesis.

Various mechanisms are accounted for the probe-to-probe interaction. The long interaction range of several micrometre (Fig. 5.5) excludes Van der Waals forces. As outlined by Klein [75], the interaction remains even with metal coated probes and metallised grounded samples which excludes electrostatic forces. The interaction is independent of whether or not the probe is in contact with the sample surface. Hence, vibrations transported through the sample can not be the origin of the interaction. Instead, the long-range interaction is attributed to oscillating air pressure between the probes and the tuning forks. If forces between the probes are induced by air pressure oscillations, rather then by mechanical contact, it is reasonable that no damage occurs.

5.3 Height-Scan Mode

The height-scan mode is applicable in single- and dual-probe operation. Usually, this mode starts with operating the detection probe in the near-field. Subsequently to each scan, the probe mount is slightly retracted from the surface. Up to a certain height, the distance-control system immediately compensates for the change of the probe mount, keeping the probe itself still in the sample's near-field. After several height steps, the distance-control system has extended the z-piezo to its maximum, such that the probe raises from the sample surface at the valleys of the texture. Step-

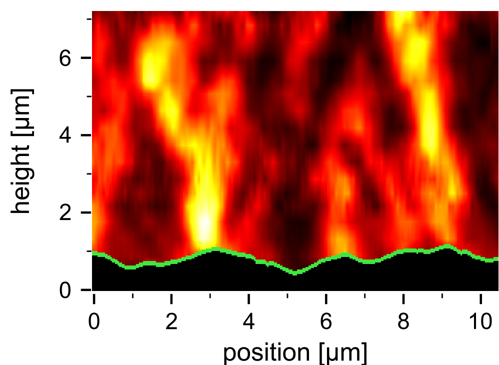

Figure 5.6: single-probe height-scan measured at a textured ZnO in collection mode in transmission geometry [76]

by-step, the probe is further retracted, until the probe is completely raised from the surface of the sample, even at the hills of the texture. Theoretically, a height of up to 100 μm is accessible, but usually, only the range from the near-field to the close far-field (ca. 20 nm - 10 μm) is of interest. Since numerous measurements are necessary to get the entire three-dimensional intensity distribution above the sample surface, the measurement duration can easily reach 30 hours, demanding for a high system stability. Small shifts in the relative position of each height layer are automatically corrected by the analysis software used for calculating the actual intensity distribution (Fig. 5.6) from the raw data [77].

6 Light Paths and Photon Loss Mechanisms in Dual Probe Measurements

In order to measure the light propagation in thin films, the sample is locally illuminated through an illumination probe while the light intensity is measured at some distance by a detection probe. Only a small fraction of the light emitted by the illumination probe finally reaches the detection probe. The intensity decay is a superposition of different photon loss mechanisms[1] which are illustrated in Figure 6.1 and are subject of this chapter.

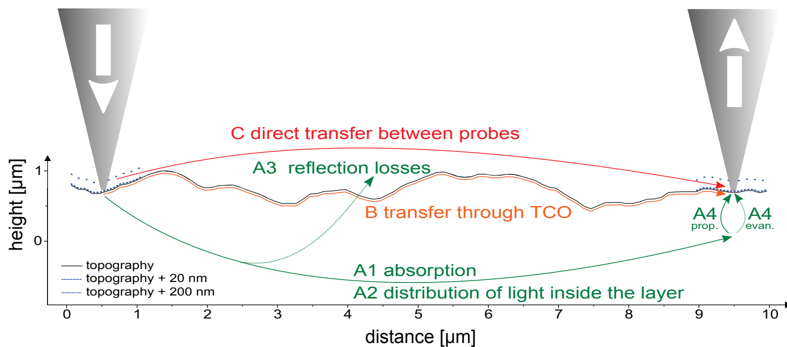

Figure 6.1: Illustration of several light paths and photon loss mechanisms in between the illumination probe and the detection probe. The displayed profile height corresponds to the topography of a standard TCO (Chap. 2.7). Additionally to the topography profile, a probe-to-surface distance of 20 nm and 200 nm is marked to illustrate the chance of a direct light transfer between the probes in case of textured surfaces.

[1] Within the context of the investigation of light propagation inside a layer, all mechanisms which reduce the number of detected photons in a dual probe experiment are considered to be loss-mechanisms. This does not necessarily mean that they reduce solar cell performance. Indeed, absorption inside the absorber layer is a required process in solar cell operation. Likewise, the distribution of light inside the layer does in general not negatively affect the efficiency of a solar cell. In contrast, reflection losses actually reduce solar cell performance.

By passing through the layer in between the probes, absorption reduces the number of photons (A1). Furthermore, only a small fraction of the photons emitted by the illumination probe propagates in the direction of the detection probe (A2). Additionally photons are transmitted at the front interface (A3). The detection probe detects photons which are transmitted (A4) at the front interface as well as those which are totally reflected (A5). Besides light paths through the μc-Si:H layer, light guidance in the TCO layer is theoretically possible. Moreover, an undesired direct transfer of light between illumination probe and detection probe has to be considered (C).

6.1 Absorption in the Sample Material

The light radiated by the illumination probe has to pass through several micrometre of the sample material before it reaches the detection probe (A1 in Fig 6.1). Thereby, the intensity decreases due to absorption. If every section of the sample material absorbs the same fractional amount of light, the intensity decays exponentially with the distance, as described by the Beer-Lambert law [78]

$$I_{\text{abs.}}(r) \propto e^{-\alpha(\lambda)\cdot r} \tag{6.1}$$

The absorption coefficient $\alpha(\lambda)$ of μc-Si:H strongly depends on the wavelength λ as it is illustrated in Figure 6.2(a). Especially for light with short wavelength, absorption is the major mechanism for a decrease of intensity. As will be shown later, several loss mechanism cause an exponential decay in intensity. In these cases the absorption coefficient is referred to as *effective absorption coefficient*.

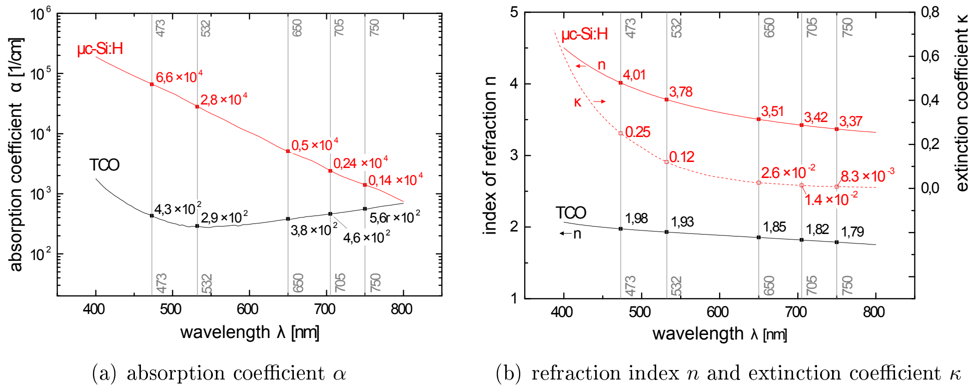

(a) absorption coefficient α

(b) refraction index n and extinction coefficient κ

Figure 6.2: Wavelength dependence of the absorption coefficient α (a) and the index of refraction n (b) for Al-doped TCO and μc-Si:H

6.2 Distribution inside the Layer

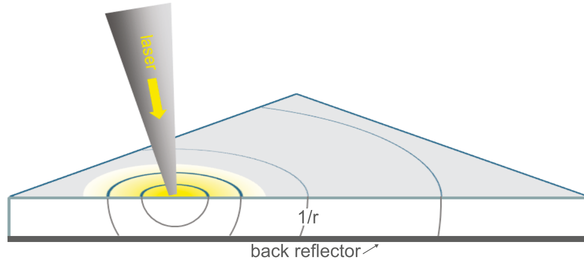

Figure 6.3: Intensity decay due to a distribution of photons in the layer

A major share of the light, emitted by the illumination probe, does not propagate in the direction towards the detection probe. Under the assumption, that the illumination probe emits light radial symmetrically, the share in emitted light intensity, which is emitted in the direction towards the aperture of the detection probe, corresponds to a circle segment with the size of the aperture. Hence, even if no absorption or reflection losses would exist at all, there is still a loss in the measured light intensity at the detection probe simply by a distribution of the light intensity inside the layer (A2 in Fig 6.1).

If the light-guiding layer is thin in comparison to the minimal probe-to-probe distance and has a high reflectivity at the front and back interfaces, the light can only propagate in two dimensions. It is confined to the xy-plane (Fig. 6.3). Hence, the intensity decreases reciprocally with the radius.

$$I_{\text{distr.}}(r) \propto \frac{1}{r} \tag{6.2}$$

Taking only the absorption and the distribution inside the sample into account, the intensity decay can easily be calculated (Fig. 6.4). As discussed in Chapter 3.10, the detection threshold allows for a loss of approximately four orders of magnitude in intensity measured from the sample area directly beneath the illumination probe to the position of the detection probe. The absorption for short wavelengths (473 nm, 532 nm) is strong and it is challenging to detect the light at an experimentally accessible distance. (more details about the detection limit ⇒ Chap. 3.9)

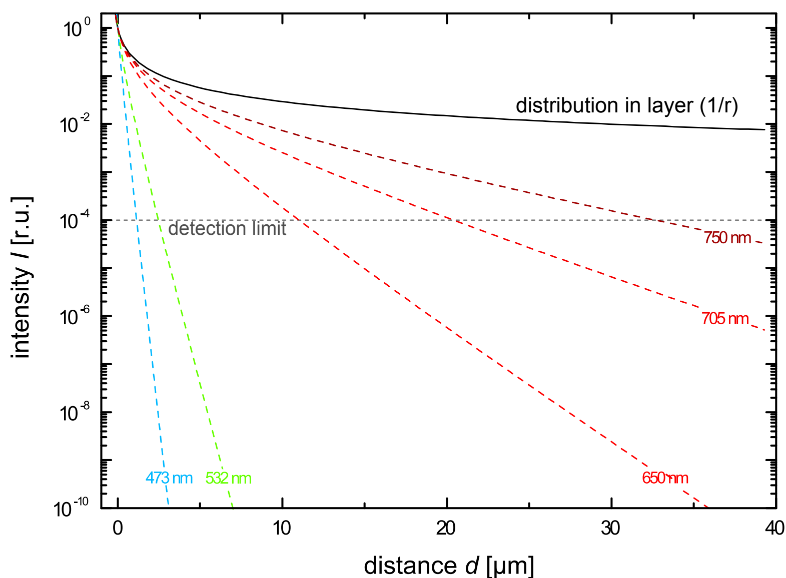

Figure 6.4: Intensity decay due to absorption and the distribution of light inside the layer for selected wavelengths. (To avoid infinite intensities for a $1/r^2$-decay at zero distance, it is assumed that the minimal spot size of the illumination probe is 100 nm. Details about the detection limit ⇒ Chap. 3.9)

6.3 Reflection Losses

6.3.1 Theoretical Background

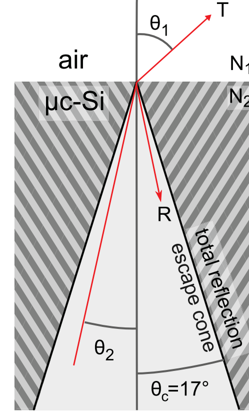

Figure 6.5: Illustration of the accessible angle range and definition of θ_1 and θ_2

Whenever light reaches an interface between two media with different indices of refraction, a part of the light is transmitted through the interface while the remaining part is reflected (Fig. 6.5). Hence, if light coming from inside the layer impinge upon the surface, a certain part of the light will leave the layer (A3 in Fig 6.1). In case of a flat, non textured, surface, the ratio between reflection and transmission of an incident plane wave is described by the Fresnel equations. For non-magnetic materials, it depends on the angle of incidence, the refractive indices of the two involved media and the polarisation. Light which is polarised perpendicular to the plane of incidence (r_s) has a higher reflection coefficient than those which is polarised parallel to the plane of incidence (r_p). According to the Fresnel equations, the reflection coefficients are determined by [13]

$$\begin{aligned} r_s &= \frac{N_2 cos(\theta_2) - N_1 cos(\theta_1)}{N_2 cos(\theta_2) + N_1 cos(\theta_1)} \\ r_p &= \frac{N_1 cos(\theta_2) - N_2 cos(\theta_1)}{N_2 cos(\theta_1) + N_1 cos(\theta_2)} \end{aligned} \tag{6.3}$$

The index of refraction N_2 and the angle θ_2 refer to the media of the incident light which is in this case μc-Si:H. Correspondingly, N_1 and θ_1 are related to the media of the transmitted light (air). The reflection coefficients change when taking the absorption of the material into account. In this case N_2 and N_1 are complex numbers

$$N_{1/2}(\lambda) = n_{1/2}(\lambda) + i \cdot \kappa_{1/2}(\lambda) \tag{6.4}$$

whereby $n_{1/2}(\lambda)$ is the real part of the index of refraction and $\kappa_{1/2}(\lambda)$ is the extinction coefficient. The absorption coefficient α is related to the extinction coefficient κ by

$$\frac{\alpha\lambda}{4\pi} = \kappa \tag{6.5}$$

The wavelength dependence of n_i and κ_i is illustrated in Figure 6.2(b). The media of the transmitted light is air. Hence, n_t is approximately equal to one and κ_t is zero. Since n_i and κ_i are strongly wavelength dependent, the reflectivity and therefore reflectivity losses will depend on the wavelength as well. The reflectivity $R_{r/p}$ is related to the reflection coefficients $r_{r/p}$ by

$$R_{s/p} = \left|r_{s/p}\right|^2 \tag{6.6}$$

Under the assumption that all directions of polarisation exist with the same probability, e.g. the light is unpolarised, the reflectivity R is simply given by the average of the reflectivity R_s and R_p.

$$R = \frac{R_s + R_p}{2} \tag{6.7}$$

The reflectivity for different polarisations and angles of incidence is illustrated in Figure 6.6(a). Contrary to total reflection in non absorptive media, the reflectivity in absorptive media like µc-Si:H is finite, even at angles larger than the angle of total reflection. Especially for short wavelengths the high extinction coefficient κ (Fig. 6.2(b)) decreases the reflectivity (Fig. 6.6(b)). However, the strong absorption in this wavelength range strongly attenuates the propagation of light anyway. Reflection losses are more important at long wavelengths. Although the losses due to finite reflectivity are small, they add

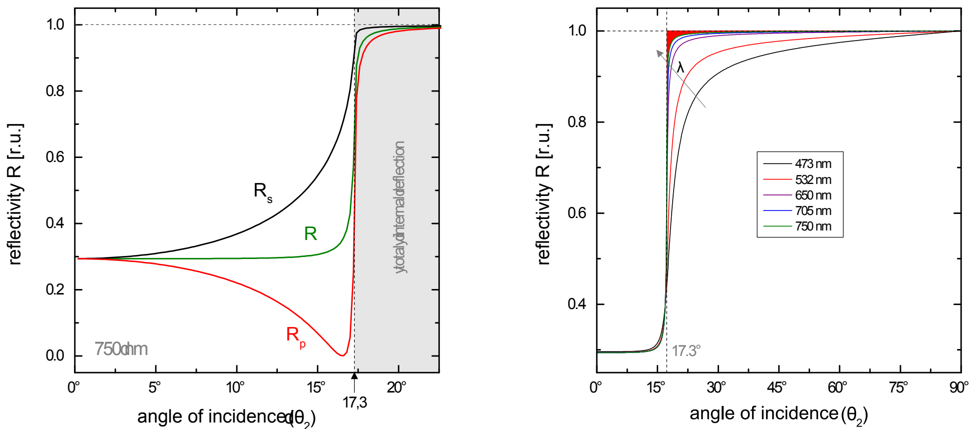

(a) Reflectivity of light polarised perpendicular R_s and parallel R_p to the interface. Additionally the reflectivity for unpolarised light R is displayed.

(b) Dependence of the reflectivity on the wavelength displayed for unpolarised light

Figure 6.6: Reflectivity at air/µc-Si:H interface

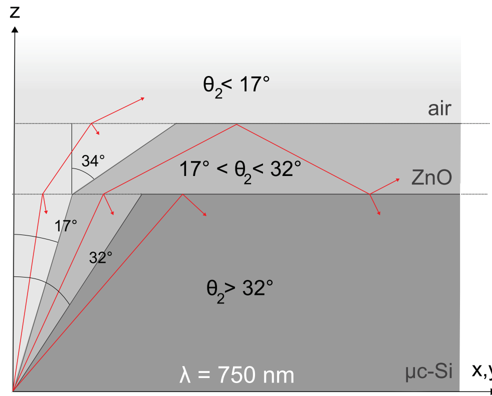

Figure 6.7: Angles of total-reflection at the μc-Si:H/ZnO and the ZnO/air interface

up for multiple reflections. It is obvious from Figure 6.6(a) that only light incident from inside the layer to the surface at angles close to or larger than the angle of total reflection is efficiently reflected back into the layer.

Angles of Total Reflection Total reflection occurs, in the proper meaning of the word, only in non absorptive media. As discussed in the previous section, the reflectivity at the interface between two adjacent media is finite if at least one of the two involved media has a decent absorptivity in the regarded wavelength range. In case of μc-Si:H at a wavelength above 700 nm, the deviation from total reflection is rather small (Fig. 6.6(b)). Hence, the term "total reflection" is used in this section despite the finite reflectivity.

An incident light ray which reaches the interface between μc-Si:H and TCO at an angle of incidence larger than 32 ° is totally reflected (Fig. 6.7). At angles between 17 ° and 32 °, the light is partly transmitted to the TCO layer but totally reflected at the TCO/air interface. If the light has an angle of incidence smaller than 17 °, it can partly transmit at the TCO/air interface and leave the layer stack. The angle of total reflection at the interface towards air determines the escape cone illustrated in Figure 6.5. Only light with angles of incidence within the escape cone can transmit through the front interface. Vice versa, the angular range which is accessible from the outside is limited to the escape cone.

The angle of total reflection related to the transmittance into air does not change when the intermediate TCO layer is excluded. Hence, for the sake of simplicity, a μc-Si:H/air interface is investigated in the following sections.

path-length increase Not only that the light is less likely reflected for small angles (Fig. 6.6(a)), it also needs a higher number of reflections at the front and back interface and a longer path-length to traverse a certain distance between the illumination and

the detection probe (Fig. 6.8). Hence, the real distance of the light passing through the absorptive media is in general longer than the distance between the probes. For the largest angle of incidence accessible from the outside ($\theta_1 = 90°$, $\theta_2 = 17.275°$) the path-length is increased by a factor of 3.4 in comparison to the direct distance between the probes. Accordingly, a measurement which determines the absorption by measuring the intensity at the sample surface might reveal an effective absorption coefficient α which is slightly too high, since it cannot distinguish if the intensity is lost due to a high absorptive media in between the probes or due to radiative losses. (As a matter of choice it would also be feasible to introduce an effective distance instead of accounting the path-length increase for a higher absorptivity. However, to keep it simple, all loss mechanisms which cause an exponential decay in intensity are described by an effective absorption coefficient α.)

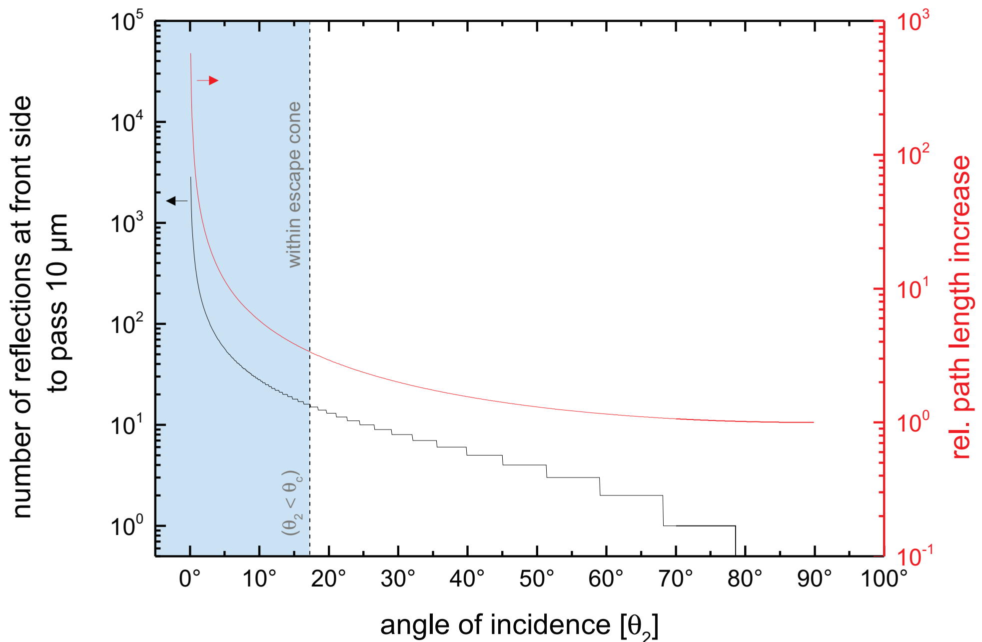

Figure 6.8: Number of reflections to pass a distance of 10 µm in dependence on the angle of incidence. Additionally the relative path length increase is displayed.

6.3.2 Intensity Decay due to Reflection Losses

Each time light incident from inside the µc-Si:H layer at angles smaller than the angle of total reflection reaches the interface between the µc-Si:H air interface a certain part of the light is transmitted and leaves the layer. The remaining part is reflected back

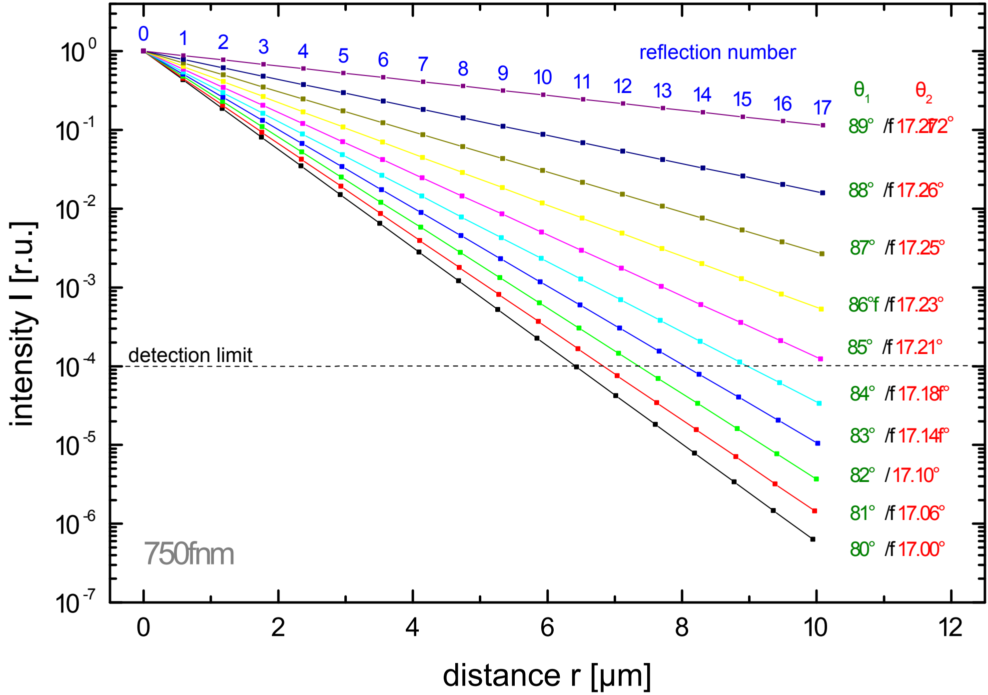

Figure 6.9: Intensity decay due to reflections in dependence on the angle of incidence in air, θ_1, and the resulting angle in µc-Si:H, θ_2 (defined in Fig. 6.5). The back reflector is assumed to be a perfect reflector. The number of reflections relates to reflections at the µc-Si:H air interface.

in the µc-Si:H layer. Hence, the intensity decays with increasing distance whereby the extinction depends on the angle of incidence (Fig. 6.9). The decay induced by multiple reflections is illustrated in Figure 6.9. To avoid reflection losses, large angles of incidence are advantageous. However, in solar cell applications and SNOM measurements with far-field illumination (collection mode Chap. 5.1), the light travels in air prior to reaching the µc-Si:H layer. Due to refraction at the interface, not all angles inside the µc-Si:H layer are accessible from the outside (Fig. 6.5). At an angle of incidence of $\theta_1 = 89°$, the light is refracted to an angle of $\theta_2 = 17.272°$ inside the µc-Si:H layer which is close to the angle of total reflection (17.275 °). After being reflected at the back reflector, which is assumed to be perfect, the light reaches the µc-Si:H/air interface. Since the angle of incidence θ_2 is close to the angle of total reflection, 88 % of the light intensity is reflected and remains inside the µc-Si:H layer. Nonetheless the path of light is reversible and the desirable high reflectivity inside the µc-Si:H layer is indivisible linked to a low transmittance of light from air into the layer.

However, the fraction of light which is multiply reflected in the µc-Si:H layer at the above mentioned angle of $\theta_2 = 17.272°$ needs 17 reflections to cover a distance of 10 µm which is chosen for comparison since it is the typical size of a standard measurement. A loss of 12 % at each reflection adds up to a loss of 89 % or roughly one order of magnitude of the original intensity. The detector has a high sensitivity. Hence, for such a high angle of incidence, the detection of the remaining light intensity will not be a problem even after 17 reflections. Nonetheless, the reflectivity strongly decreases for smaller angle of incidence. At an angle of $\theta_1 = 85°$, which corresponds to $\theta_2 = 17.21°$ inside the µc-Si:H layer, the reflectivity is 59 %. The reflection losses add up to four orders of magnitude after 10 µm or 17 reflections which is close to the detection threshold. At even smaller angles of incidence, the reflection losses will increase tremendously.

effective absorption coefficient Photons which pass through a certain length of the material have a specific chance of being absorbed. This probability keeps constant for the remaining photons. The same is true for losses induced by reflections. Unless the angle does not change, the reflectivity is equal for all reflections. Hence, the intensity decay due to reflections is subject to a similar exponential decay behaviour. Absorptivity, path-length enhancement and finite reflectivity result in a distance dependent decrease in light intensity and will therefore increase the effective absorption coefficient α in equation 6.1.

6.4 Light Guidance in the TCO Layer

A further, at least theoretically feasible light path, is light guidance in the TCO layer (Path B in Fig 6.1). However, in case of the investigated nip-structures, the TCO-layer thickness is only 60 to 80 nm (Chap. 2.7) and the attenuation, especially for the long wavelengths, is high. Additionally, the TCO layer follows the textured surface and the light can easily be scattered outside the layer. Moreover, it is difficult to couple light into the TCO layer.

6.5 Direct Light Transfer between Illumination and Detection Probe

Last but not least, a direct light path between illumination and detection probe has to be considered which completely bypass the sample material (Path C in Fig 6.1). If a major part of the light intensity at the illumination probe is directly coupled into the detection probe, the intensity decay will not have an exponential behaviour. Instead, the intensity will decay proportional to $1/r$, independent of the wavelength and the sample material.

Damaged probes, or those with a leaky coating, might cause a direct transition between the probes. Simulations reveal that for ideal probes, the direct transition is negligible (Chapter 8). If textured samples are measured and the illumination probe is placed in a valley of the texture, it is unlikely that light from the illumination probe can directly reach the detection probe since it is blocked by the hills of the texture which are high in comparison to the probe-to-sample distance (The texture height in Fig. 6.1 is true to scale.). Nevertheless, at long distances between illumination and detection probe and correspondingly low light intensities close to the detection limit, a direct transfer of light between the probes might have a significant influence. This applies in particular to short wavelengths at which the absorptance is too high to allow for a measurement of guided light inside the layer.

7 Measurement of the Light Propagation in thin films

This section is about measuring the light propagation in thin films and extracting relevant parameters from the experimental data by using different approaches for the data analysis. Initially, a basis dual-probe mode is introduced which allows for an immediate visualisation of light propagation. Subsequently, a more sophisticated scan procedure is described which compensates for the non-constant coupling efficiency, caused by local surface features. Additionally, the thin boundary between facts and artefacts in near-field optical measurements is discussed. Artefacts can cause misleading results, but might also be used to characterise the SNOM probe.

7.1 Basic Dual-Probe Mode

Measurements of the light propagation are performed in dual probe mode. In a basic implementation, the illumination probe is placed at a constant position while the detection probe scans above the sample surface in direct vicinity to the illumination mode. The mode of measurement is described in more detail in Chapter 5.2. The measured light distribution is illustrated in Figure 7.1. It is an advantage of this mode of measurement, that the measured intensity map directly correspond to the intensity distribution.

7.1.1 Analysis by Line Scans

The easiest way to extract the intensity decay from the experimental data is to analyse line scans in the direction of light propagation. To investigate the dependence of the results on the selection of the specific line, three different lines are chosen and the results are compared (Fig. 7.1). Line scan (1) is chosen to be aligned and centred along the main intensity lobe, whereas line scan (2) is slightly shifted to determine the influence of small shifts on the result. Line scan (3) is aligned to a small, minor distinct lobe.

An analysis software, especially programmed for this purpose, extracts line scans along arbitrary selectable paths. Thereby, an adjustable number of parallel neighbouring line

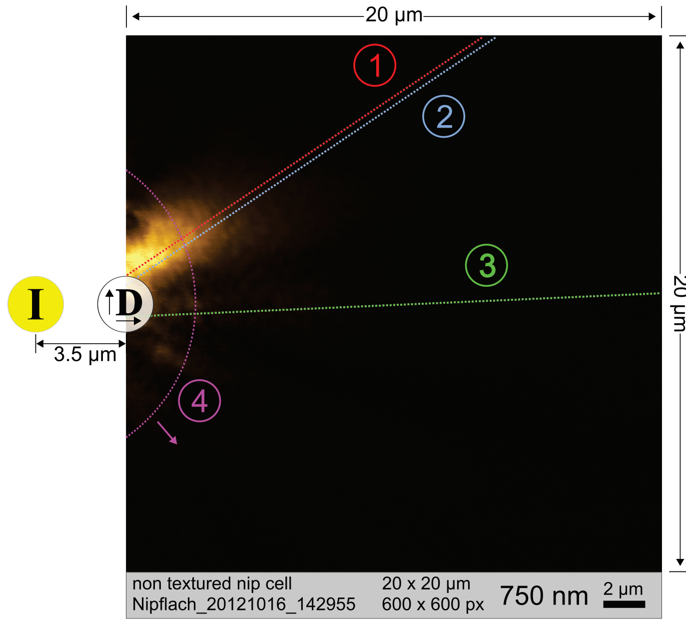

Figure 7.1: Arrangement of the illumination probe (I) and the detection probe (D) in dual-probe operation. At this measurement, the illumination probe is placed at a constant position while the detection probe is chosen as scan device. Additionally the position of selected linescans (1) to (3) and the circular averaging procedure (4) is illustrated.

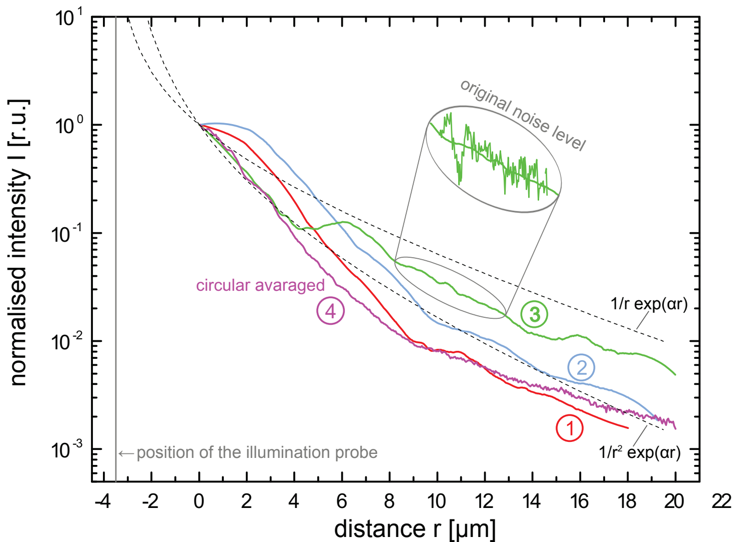

Figure 7.2: Intensity decay determined by line scans (1), (2), and (3) alongside the paths displayed in Fig. 7.1. Additionally the intensity decay based on circular averaging (4) is shown. Furthermore, two theoretical decays are displayed which take the absorption and the distribution inside the layer into account. (All graphs normalised to their initial intensities.)

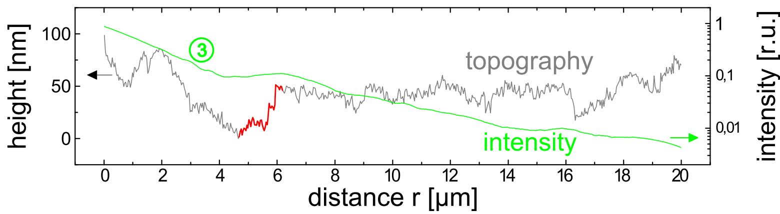

Figure 7.3: Intensity and topography along line scan 3

scans (5 in this case) are used for averaging and noise reduction. The intensity decay alongside the chosen paths is illustrated in Figure 7.2. The graphs are further smoothed to clarify the intensity decay. The original noise level is shown exemplarily for parts of line scan (3) as well.

Leaving aside effects at the first 2 µm which are most likely due to a signal overload, the intensity decays of line scan (1) and (2) have the same slope. Line scan (3) reveals a distinct kink in the intensity decay. The origin of the kink is obvious from Figure 7.3 which displays the intensity together with the topography. At a distance between 4 and 6 µm, the line scan crosses a topography feature with a height of about 50 nm. Obviously, the topography feature, which might be a little scratch at the surface, influences the light propagation. The differences in the intensity decay of selected line scans reveal a disadvantage of this method of data analysis. The results depend on the more or less arbitrary selection of a suitable line scan path. Depending on whether or not single surface features are crossed, the intensity decay shows a different behaviour. This might be on purpose in some cases but is less appropriate for gaining general physical properties like an effective local absorption coefficient which is an important quantity for example for the determination of the path length enhancement. A further drawback of a data analysis based on line scans is that line scans simply ignore the major part of the data providing no information about the frequency of occurrence and the overall influence of special surface features like the one crossed by line scan (3).

7.1.2 Analysis by Circular Averaging

A more elaborate method of data analysis is *circular averaging*. Thereby, the intensity along equal distance to the illumination source is averaged and plotted versus the distance. Beside a reduced noise level (the intensity decay in Figure 7.2 based on circular averaging is not smoothed), single surface features have a distinctly reduced influence on the intensity decay. The decay has the same slope than line scan (1) and (2) at short as well as at large

distance but without the above mentioned distortions. However, at textured surfaces, bright spots occasionally occur at major hills of the texture (Fig. 7.4). Whenever such a bright spot is crossed by a circle, the intensity decay is affected.

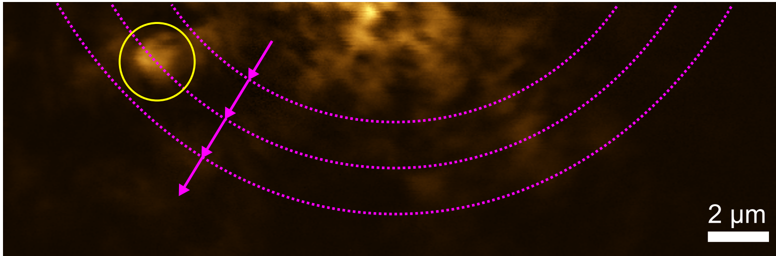

Figure 7.4: Circular averaging at textured surfaces influenced by a local surface feature

7.2 Coupling Efficiency Eliminated Scan Mode

The coupling efficiency eliminated scan mode is a special kind of a dual-probe measurement. At this mode of operation (illustrated in Figure 7.5), the probe-to-probe distance is kept constant while the sample itself is moved. The measurement starts with scanning a small sample area of $5 \times 5\,\mu\text{m}$, just large enough to contain a sufficiently large number of surface features and to prevent that single features dominate the overall intensity. After each measurement, the probe-to-probe distance is slightly increased and the same scan as before is performed. This procedure is repeated a number of times. In total, 31 measurements cover the distance range from $3.5\,\mu\text{m}$ to $16.5\,\mu\text{m}$. Since the probe-to-probe distance is kept constant within one measurement, the contrast in the pictures represents the efficiency of all light paths between the probes placed at a certain sample position. The average brightness of the measured intensity maps corresponds to the average light intensity at a certain probe-to-probe distance (mind the colour scales in Fig. 7.5). By extracting the average intensity from each measurement, the intensity decay inside the layer is revealed.

The measurement is completely automated which offers the opportunity to run multiple distance iterations consecutively. Figure 7.6 displays the intensity decay in a flat nip cell, measured at five successive runs. The start position of each run is not exactly the same which results in different initial intensities. Shifts in between the measurements can easily be identified by comparing the topography data saved simultaneously with the optical data. The intensity decay measured at run 3 is selected for the following comparison with experimental data of textured nip cells and simulations.

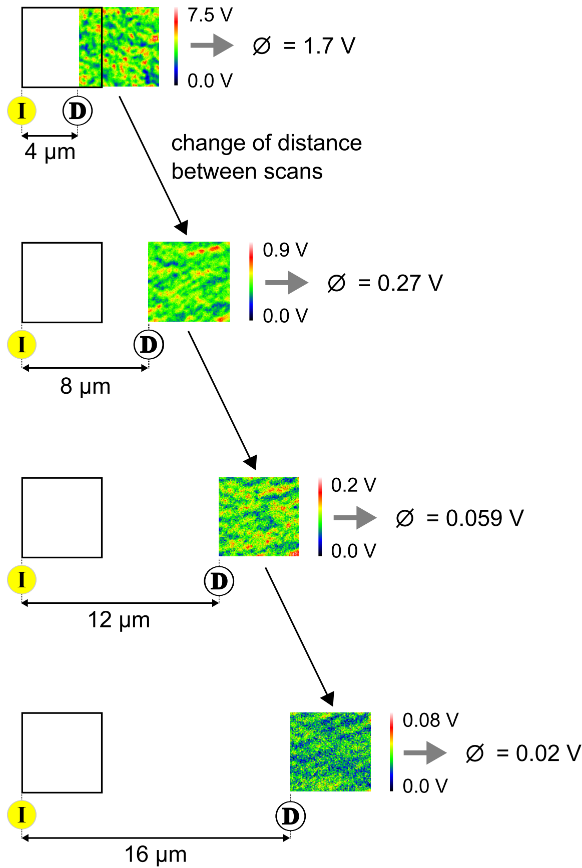

Figure 7.5: Illustration of the coupling eliminated scan procedure. The black squares symbolise the scan area of the illumination probe, whereas the actual measured intensity maps are placed accordingly to the distance between the illumination probe (I) and the detection probe (D). The probe-to-probe distance is constant within a single measurement and changed stepwise in between the measurements. The images are plotted on a linear scale. The voltage is proportional to the intensity.

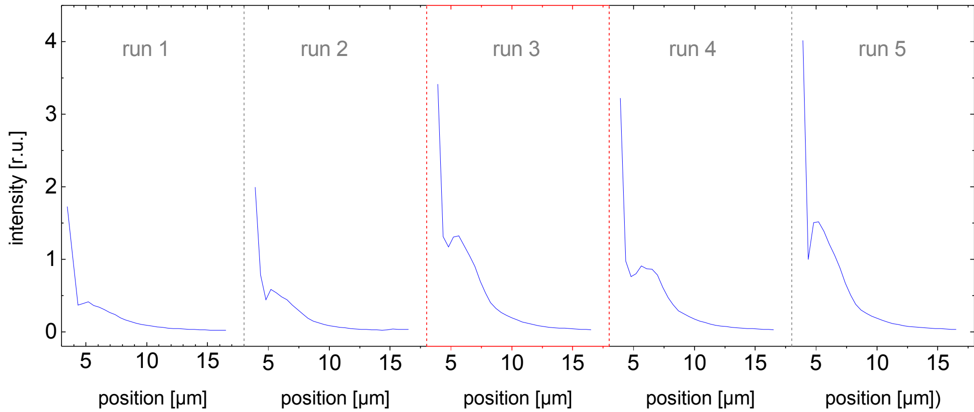

Figure 7.6: Measured intensity decay at a wavelength of 750 nm in a flat nip cell on five successive runs (the data of run 3 are presented on a log scale in Figure 7.7)

In Figure 7.7, the intensity decay in a flat and textured nip cell on a wavelength of 750 nm is displayed alongside with pictures of the single measurements at each distance step. The experimental data are determined based on the introduced coupling efficiency eliminated scan mode. The intensity decay for the textured nip cell is in good agreement with the predictions from the ray-tracing approach. A distinct bump around 4.5 µm is present in the intensity decay measured at a flat nip cell. It will be shown by FDTD simulations in Chapter 8.2 that the bump is related to effects not included in the ray-tracing model. The measured light intensities at long distances slightly exceed those predicted by the ray-tracing approach.This effect is more pronounced at shorter wavelength as will be shown in the following section.

7.2.1 Wavelength & Texture Dependence of the Intensity Decay

In general, the coupling efficiency eliminated scan mode can be combined with the capability of the SNOM system to measure multiple wavelengths simultaneously. Nevertheless, the accessible wavelength range is limited by the high absorptivity of the considered sample material at short wavelengths (<650 nm) and the low sensitivity of the applied GaAs detector at long wavelengths (>800 nm).

In Figure 7.8, the intensity decay for a wavelength of 650 and 705 nm is illustrated. The experimentally determined decay is less strong than predicted by the ray-tracing model. As already mentioned, a direct transmission of light from the illumination to the detection probe above the sample surface might influence the measurements as soon as the intensity transmitted through the sample material is low. Light with short wavelengths is

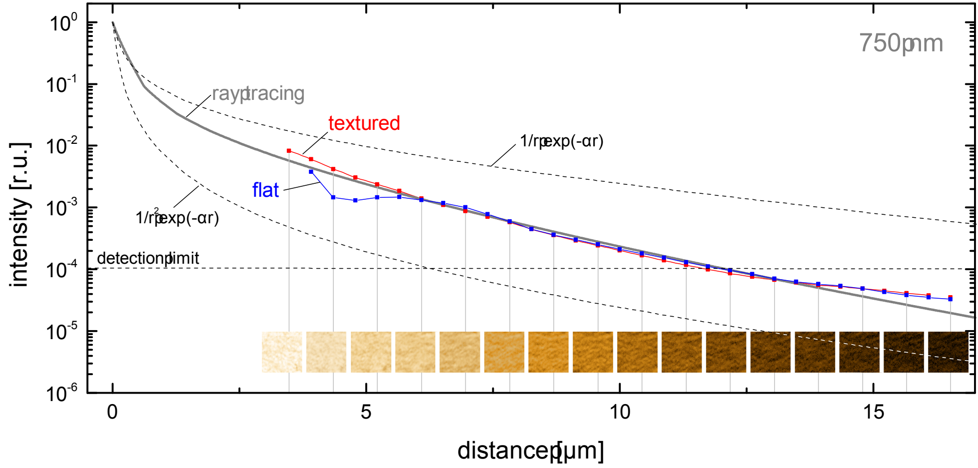

Figure 7.7: Intensity decay measured at a textured and a flat nip cell, by applying the coupling efficiency eliminated scan mode. The grey line represents the simulated intensity decay based on the ray-tracing approach. The dashed lines illustrate the theoretical intensity according to a distribution of light and absorption inside the layer. (The images of the single measurements refer to the flat nip cell and are plotted on a logarithmic intensity scale)

strongly absorbed in µc-Si:H. Hence, short wavelengths result in short maximal detection distances and strong influence on stray light. The applied lock-in amplifiers effectively filter the stray-light originating from the room illumination or displays of the measuring equipment. Unfortunately, the light directly transmitted from the illumination probe can not be filtered by the Lock-In amplifier since it has the proper modulation frequency. Additionally, a direct light transmission in-between the probes can explain why the intensity continuously decreases even at long distances. The intensity of light which propagates through µc-Si:H is continuously decreased due to absorption and reaches the detection limit at a certain distance, e.g. 12 µm for a wavelength of 750 nm. Any light intensity detected at longer distances can not originate from light propagation through µc-Si:H and might most likely due to a direct light transfer between the probes.

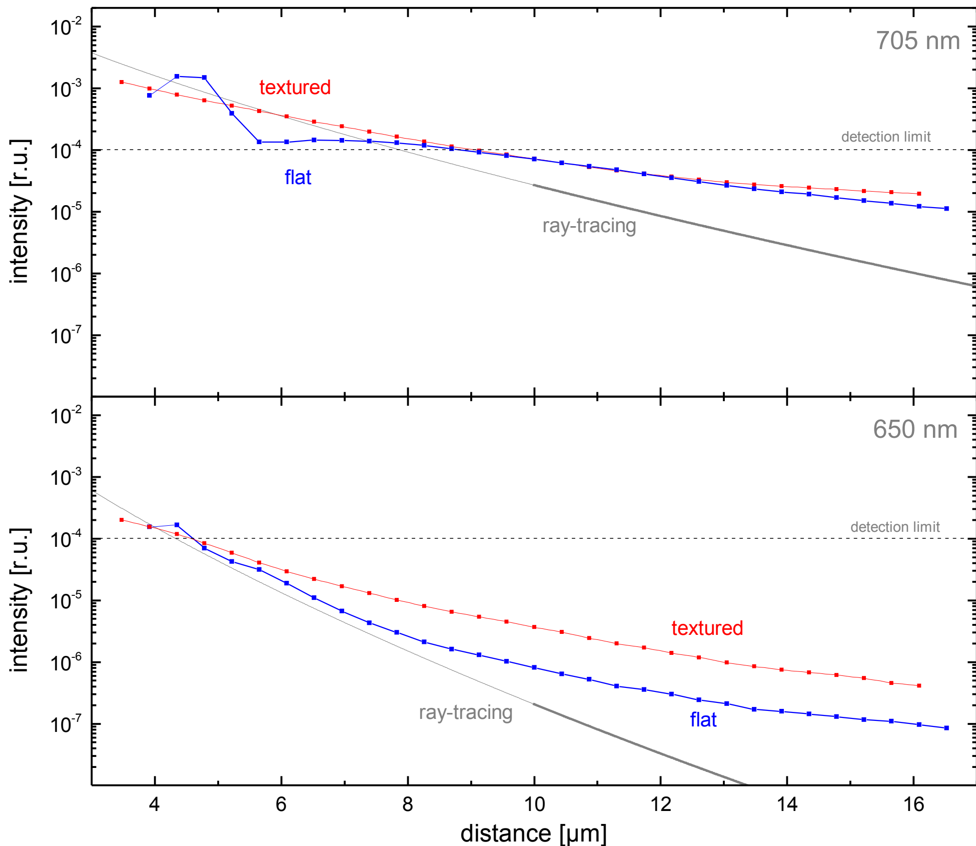

Figure 7.8: Intensity decay measured on a textured and a flat nip cell at a wavelength of 650 and 705 nm.

7.3 Fact or Artefact?

SNOM measurements can be influenced by artefacts. In this context, artefacts are all measured features that do not represent the real sample. A common topography artefact is caused by the finite size of the SNOM probe. During a scan, the surfaces of two objects, namely the sample surface and the probe, interact with each other. The probe is guided above the sample surface in a way that the shortest distance between probe and sample is kept constant. Thereby, the vertical movement of the probe, which is induced by the distance-control system to ensure a constant probe-to-sample distance, is saved and referred to as topography.

However, the topography is always a convolution of the sample surface and the probe surface. In an ideal case, the probe has an extremely sharp tip (extremely small aper-

ture size) and an opening angle that is smaller than any surface angles of the sample (fig. 7.9 (a)). Exclusively in this particular case, the measured topography equals the sample's topography. As soon as the sample surface exhibits topography features which are steeper than the probe, a de-convolution of the measured topography into the sample topography and the probe shape becomes difficult.

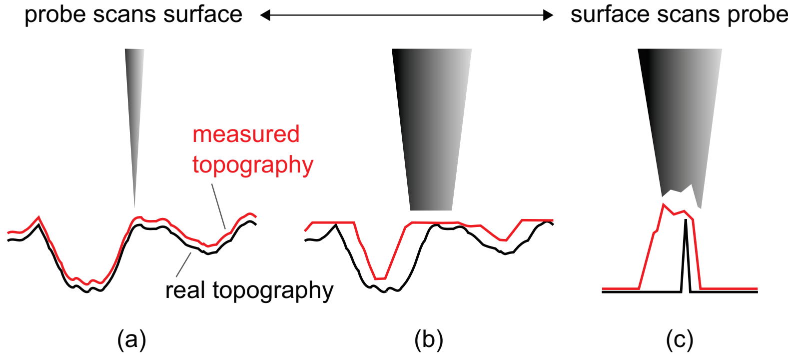

Figure 7.9: Artefacts induced by the finite size of a scanning probe. (a) Scan performed by a probe with sharp tip and small opening angle. (b) Strong convolution of probe and sample surface due to a blunt tip. (c) Inverted scan. Sharp topography feature scans the probe's shape.

As illustrated in figure 7.9 (b), the measured topography of steep surface craters reveals smaller craters than in reality. The location-dependent offset to a constant probe-to-sample distance induces optical artefacts, as evanescent fields decay exponentially (Chap. 2.4, in particular Fig. 2.5). Any change in the probe-to-sample distance will strongly change the intensity of evanescent fields. In worst case, the change in the intensity is solely due to topography artefacts. Figure 7.10 illustrates several artefacts in the measured optical signal, induced by a mismatch between the probe-to-sample distance and the actual height of the topography at the probe's position. In figure 7.10 (a), protrusions at the probe induces a shift of the measured topography and the intensity with respect to the real surface. Comparing the optical data with the measured topography conveys the impression that the intensity is low at the peak of the topography. Actually, the intensity is low, because the probe-to-surface distance is increased when the protrusion at the probe reaches the surface feature. If the apex is finally placed on top of the surface peak, the probe-to-sample distance is low and the increased intensity, which commonly occurs at sharp surface features, is measured.[1]

[1] The distance dependence of the measured intensity is actually more complex than outlined in this section. It might be that the intensity measured by a probe which is placed in the near-field of the sample's surface is dominated by evanescent fields. If the probe-to-sample distance is increased, the intensity decreases. In some higher distance to the surface, stray-light might couple into the SNOM probe, increasing the measured intensity. Furthermore, micro-lens effects can focus the light to certain

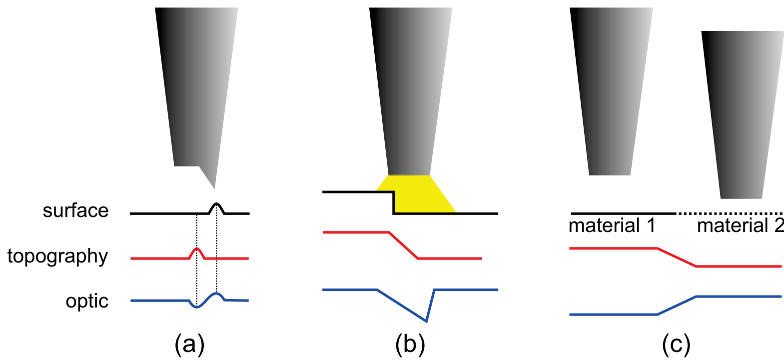

Figure 7.10: Optical artefacts induced by (a) protrusion at the probe and shifts in the probe-to-sample distance due to (b) surface features or (c) change in the material properties. (figure (a) based on [79], (b) on [15])

Figure 7.10 (b) adresses a similar situation. At steep surface features, like the trench of a surface marker, the probe-to-sample distance is changed, influencing the measured light intensity. The probe-to-sample distance can even change without a change in the surface height (Fig. 7.10 (c)). The strength of shear-forces depend on various parameters (Chap. 2.6) which are not necessarily equal for different materials. Hence, a scan above the border of surface cluster which contain different materials might exhibit topography artefacts. Fortunately, the samples investigated have a homogeneous surface material.

Besides the steepness of the probe, its apex diameter induces artefacts. Probes designed for atomic force microscopy have smaller apex diameter and will therefore provide higher resolution with less artefacts (Chap. 3.7). By applying AFM and SNOM measurements at the same field, the optical data gained by a SNOM measurement are supplemented with the high resolution AFM topography data. If the shape of the SNOM probe is known, or if at least reasonable assumptions are available, the optical data can, to a certain extent, be corrected. If the measured data are later on compared with simulations, the accordance is increased if the finite size of the probe is taken into account [80].

An extreme case of a topography artefact is shown in figure 7.9 (c). The displayed surface contains a surface feature which has a smaller apex diameter than any feature of the SNOM probe. Consequently, the surface feature scans the probe and the measured topography equals the shape of the probe apex instead of the sample's surface. This effect might be used to characterise the probe as described in the next section.

areas above the surface. Hence the intensity will in general not have a simple distance dependency.

7.3.1 De-convolution of the probe's shape from topography measurements

Topography artefacts are strongly apparent when scanning above a sharp edge of a deep trench. Figure 7.11 displays a topography scan of a trench which is part of a surface marker (Chap. 3.7). The trench is produced by focused ion beam treatment which creates sharp edges on the relevant length scale[2]. The sharp edge of the trench scans the side of the probe when its moving down the trench. On the opposite trench wall, the other side of the probe is imaged. The probe is slightly tilted to allow for a close approach to the second probe in usual dual-probe operation. Hence, the steepness at the opposing trench walls is different. The measured topography is a convolution of the edge's shape with the probe's contour. Assuming perfectly sharp trench walls, the probe shape as well as the probe tilt can be reconstructed from the topography scan as shown in figure 7.11 (b).

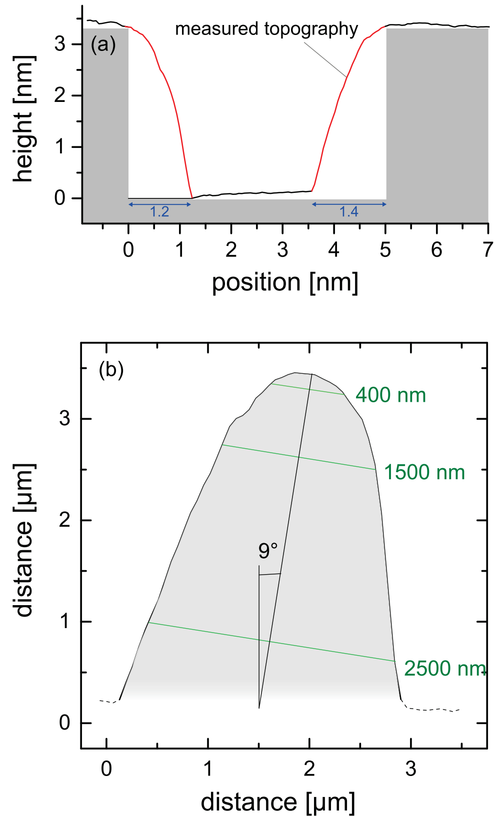

Figure 7.11: (a) Topography scan of a trench in the sample's surface. The grey area illustrates the theoretical shape of the trench. The measured topography directly corresponds to the probe's contour. The red part of the topography graph is used for the reconstruction of the probe's shape depicted in (b). The reconstructed probe shape reveals a tilt of 9°.

From a single scan line, only the cross section of the probe is reconstructible. Although it might not be the primary intended purpose of a near-field microscope, it is feasible to scan above the sharp edges of the surface marker in multiple direction and to de-convolute the entire shape of the probe.

The de-convolution of the probe's shape from topography measurements is an extreme example of an inverted scan process at which the probe is scanned by the sample rather than being the scan device.

[2] The trench is partly cut in the glass substrate and is therefore deeper than the absorber layer thickness

8 Simulations

In this chapter two different approaches for a simulation of the light propagation in thin films are presented.

A ray-tracing algorithm offers the opportunity to investigate different loss-mechanisms separately. The distribution of light inside the layer, absorption, and reflection losses at the front interface are taken into account. Furthermore, the influence of wavelength, angle of incidence, and distance on the intensity decay is revealed separately for the different loss mechanisms. The angular distribution of the light, emitted from the illumination probe, is taken as initial input of the ray-tracing simulation. The algorithm exhibits how the angular distribution changes while the light propagates in a thin layer.

In the second part of this chapter, a finite-difference time-domain (FDTD) simulation is presented. This highly hardware demanding simulation grants access to the electro-magnetic field distribution on a sub-wavelength scale. The simulations are the counterpart of the measurement shown in Chapter 7.

8.1 Ray-Tracing Approach

In the following, the loss induced by multiple reflections at a flat, non-textured front interface is investigated by a ray-tracing approach. The main idea of this approach is to investigate the relative strength of the different mechanism, responsible for the intensity decay inside the μc-Si:H layer and to examine the wavelength dependence as well as the influence of different angular distributions of the incident light. Although less accurate, ray-tracing simulations are a useful approach for explaining the intensity distribution determined by FTDT simulations.

The ray-tracing procedure calculates the light path for a given angle of incidence and determines the reflectivity loss, the distribution inside the layer and the absorptance.[1] Thereby, the significantly different path-length for different angles of incidence is considered for the absorption calculation. The approach assumes incoherent illumination. Interference of different rays is not considered. The intensity decay due to reflection

[1] The different loss-mechanisms are discussed in detail in Chap. 6.

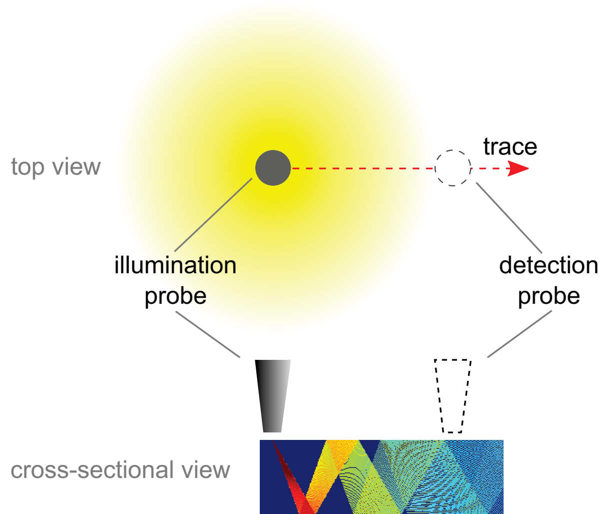

Figure 8.1: Visualisation of the ray-tracing approach. Given the angular distribution of the light emitted by the illumination probe, the ray tracing algorithm determines the path of light inside the layer. Absorption, reflection losses at the front interface and the lateral distribution of light is calculated for each ray independently. The approach considers a two dimensional slice of the layer between illumination and detection probe.

losses and absorption is calculated for each ray independently. The overall intensity decay is determined by subdividing a certain length of the μc-Si:H layer and adding up the intensity of all rays inside this subsection. The approach considers a two dimensional slice of the layer between illumination and detection probe as depicted in Figure 8.1.

Ray-tracing is based on geometrical optics. In a strict sense, geometrical optics is only applicable if the involved length scales are significantly longer than the wavelength. A layer thickness of about 1 μm may not satisfy this criterion, especially for the longer wavelengths of 705 and 750 nm (in vacuum). A physically more precise method are FDTD-simulations which are described in the second part of this chapter. However, FDTD-simulations are extremely hardware demanding and are therefore performed on a supercomputer. Hence, this method is not suitable for testing the influence of various system parameters on the intensity decay. As long as the involved scales are not too small, ray-tracing is an conveniently accessible approach for the investigation of loss mechanism which allows for an understanding of the different loss principles.

8.1.1 Ray-tracing for Realistic Angular Distribution

Refracting angles, path-lengths, and reflection losses can easily be calculated for arbitrary angles of incidence. Nonetheless, the angular distribution of the light emitted by the illumination probe needs to be known, in order to simulate the intensity decay inside the µc-Si:H layer. As it will be shown in Chapter 8.2.2, a FDTD-simulation of an µc-Si:H half-space provides the required angular distribution of the light emitted by a SNOM probe placed in the near-field of a sample surface. This way, the angular distribution of the light emitted by the illumination probe and the angular dependent sensitivity of the detection probe are considered when adding up the intensities of the single rays. (It is assumed that the angular distribution of the emitted light and the detection sensitivity both have the same angular dependence.)

The extraction of the angular distribution implies some uncertainties (Chap. 8.2.2). Therefore, the ray-tracing procedure is performed with a set of Gaussian distributions as well, to gain insight into the influence of a change in the angular distribution on the intensity decay. Figure 8.2 displays the angular distribution of light emitted by a SNOM probe next to Gaussian distributions given by

$$\text{counts}(\theta) = exp\left(-\frac{\tan(\theta)^2}{2\sigma^2}\right) \tag{8.1}$$

with several standard deviations σ. As will be shown later, the crucial difference in the

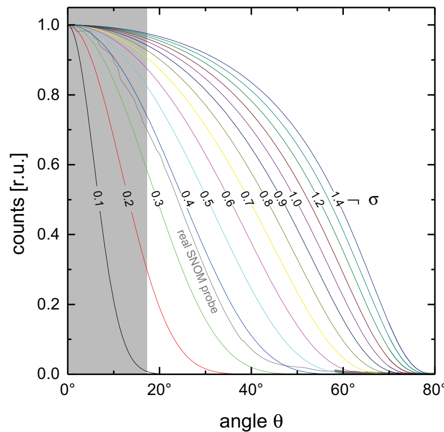

Figure 8.2: Angular distribution of the light emitted by a SNOM probe (grey line) and several gaussian distributions (coloured lines). The grey area represents the angle range which is smaller than the angle of total reflection.

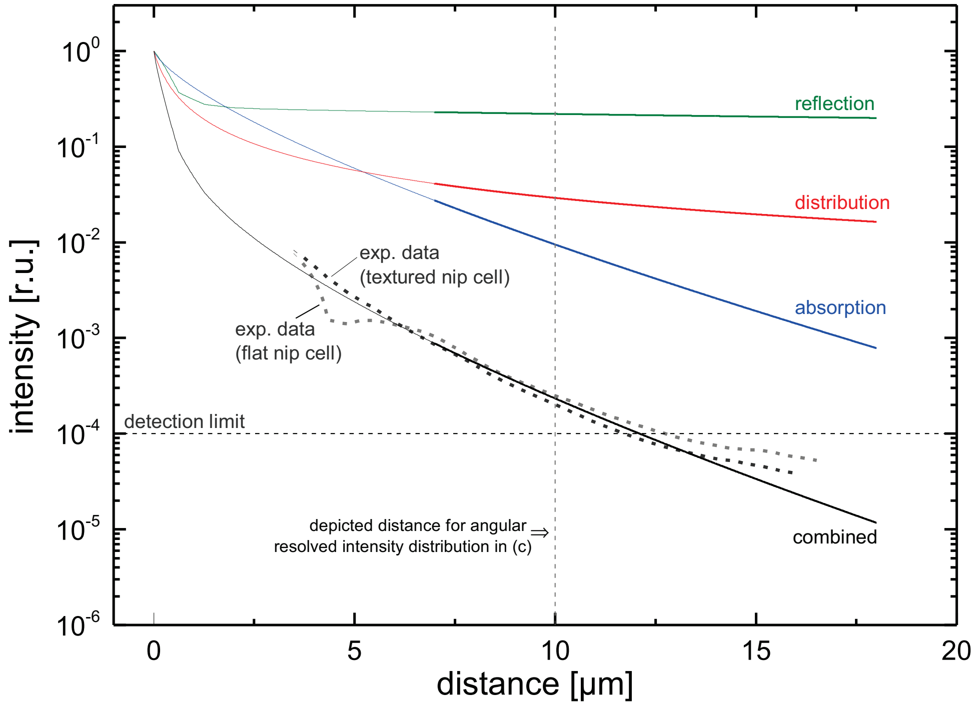

(a) Intensity decay for different loss-mechanism (750 nm)

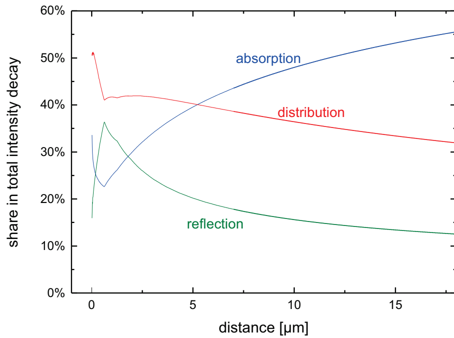

(b) Separation of the overall intensity decay into the main loss-mechanism (750 nm)

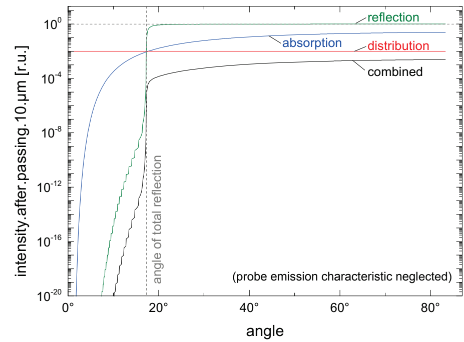

(c) Angular resolved intensity after passing 10 µm of µc-Si:H (750 nm)

Figure 8.3: Results of the ray-tracing model

angular distributions is the share in integrated intensity at angles beyond the angle of total reflection.

Figure 8.3(a) visualises the results of a ray-tracing simulation based on the angular distribution of light emitted by a SNOM probe. The loss mechanisms do not directly influence each other. Accordingly, the different loss mechanisms are treated separately, like in a system at which only one loss mechanism exists at the same time. The displayed combined intensity loss is a superposition (product) of independent loss mechanisms. A comparison between the simulated intensity decay and experimental data reveal good correspondence, especially when keeping in mind, that the ray-tracing approach neglects any effects which relate to the wave nature of light. The bump in the experimentally determined intensity decay of the flat nip cell[2] is not apparent in the ray-tracing simulation. This modulation of the decreasing intensity is related to interferences induced by multiple reflections inside the μc-Si:H layer. Due to the incoherent approach, interferences are not considered, but will be explained by FDTD-simulations in Chapter 8.2. The deviation between simulation and experiment at distances above 13 μm might be attributed to a direct transmission between the probes (path C in Fig. 6.1) which has an increasing share of the measurement signal at low intensities close to the detection limit (Chap. 6.5).

Figure 8.3(b) displays the share in total intensity of the intensity decay due to absorption, reflection losses and a distribution of light inside the layer, in dependence on the probe-to-probe distance. The intensity decay caused by reflection losses reveals a maximum at a distance at which light rays with small angle of incidence reach the front interface for the first time. Due to the high transmittance at small angles of incidence, the intensity of rays with small angles strongly decays at each reflection at the front interface. Moreover, at small angles of incidence, a high number of reflections is needed to pass a certain distance, measured parallel to the surface (path length increase displayed in Fig. 6.8, p.70). As soon as light rays with small angle of incidence are transmitted through the front interface, the relative strength of reflection losses decreases. The distribution of light inside the layer is the major loss-mechanism for short distances. At distances beyond 5 μm, the attenuation of the propagating light is dominated by absorption.

Obviously, the strength of at least some of the loss-mechanisms depend on the angle of incidence. To investigate this dependency, the attenuation of light with different angles of incidence is considered. Figure 8.3(c) illustrates the relative intensity after passing 10 μm of μc-Si:H in dependence on the angle of incidence. As previously mentioned, the intensity decay due to finite reflectance at the front interface, strongly depends on the angle of incidence. Hence, the decrease in intensity of rays with small angles is several orders of magnitudes stronger than for rays with angles larger than the critical angle.

The absorptance depends on the angle of incidence, because the actual path length inside the absorber layer is longer for small angles of the incident light. Within this

[2] flat nip cell: non textured μc-Si:H thin-film solar cell in n-i-p configuration (Chap. 2.7)

model, the intensity decay due to a distribution of light only depends on the distance between the probes. Hence, no angle dependence is apparent for this loss-mechanism.

Influence of the Wavelength and the Angular Distribution Finally, the ray-tracing approach offers an insight into the influence of the wavelength and the angular distribution on the intensity decay. As it is shown in Figure 8.4(a), the wavelength has a strong influence on the absorption. For short wavelength, the decay due to absorption is the major reason for the decrease in intensity with increasing distance to the illumination probe. The reflection losses (Fig. 8.4(b)) are less influenced by the wavelength. At angles slightly above the angle of total reflection, the reflectivity depends on the extinction coefficient which is wavelength dependent. In μc-Si:H, the extinction coefficient is high at short wavelengths (Fig. 6.1) which result not only in high absorbance but also in high reflection losses (Chap. 6.3). The simulated combined losses for different wavelengths are illustrated in Figure 8.4(c). Exemplarily, the experimental data acquired at a wavelength of 750 nm are compared to the simulated data.

The intensity decay is correlated to the angular distribution of light inside the layer. A small standard deviation σ relates to a distribution at which a major part of the intensity is shared among rays with small angles of incidence. The path-length increase for small angles is high which results in high absorptance (Fig. 8.4(d)). Furthermore, the number of reflections needed to pass a certain distance measured parallel to the sample surface is high for low angles of incidence. The high number of reflections combined with the low reflectivity at small angles of incidence result in high reflection losses for distributions with small standard deviation (Fig. 8.4(e)). The combined losses, calculated for a Gaussian distribution with a standard deviation σ of 0.4, agrees best with the data based on the angular distribution of a real SNOM probe and the experimentally determined data (Fig. 8.4(f)).

8.1.2 Limitations of Ray-Tracing

A prerequisite for the applicability of the ray-tracing approach is the knowledge about scattering and reflection at the interfaces. In case of flat surfaces, no scattering occurs and it can be assumed that the angle of incidence equals the angle of reflection. The angle dependent reflectivity is described by the Fresnel-equations. Textured surfaces are more complex, especially if the texture exhibits features smaller than or similar to the wavelength. The angular distribution induced by scattering at textured surfaces is described by several theoretical models [24, 54, 74, 81–83]. However, it is difficult to calculate the reflection coefficient since the Fresnel-equations do not apply.

Furthermore, ray-tracing is not applicable at subwavelength-sized structures, e.g. to

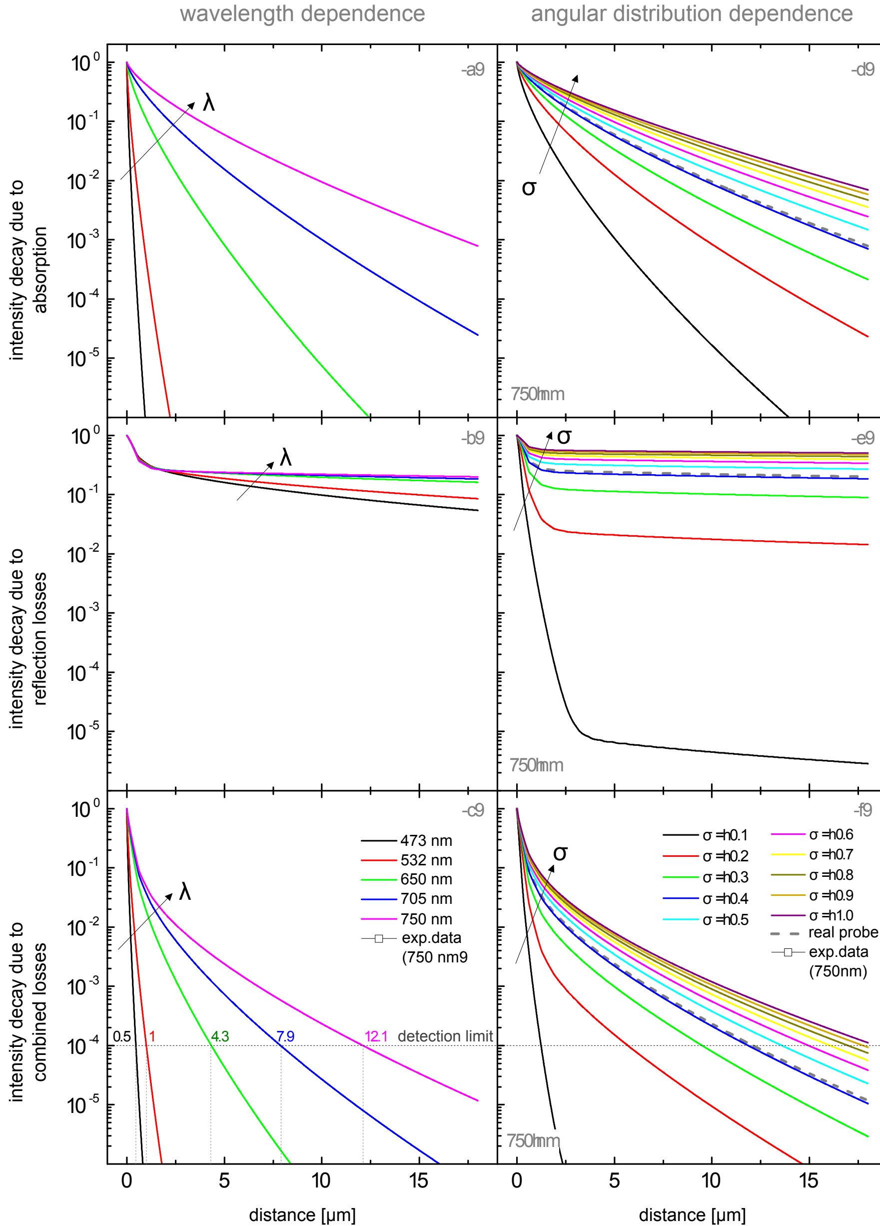

Figure 8.4: Intensity decay due to absorption (a), reflection losses (b), and combined losses (c) for different wavelengths. Additionally, the intensity decay based on the angular distribution of a SNOM probe and several several Gaussian distributions with different standard deviations σ is displayed separately for the different loss mechanisms (d),(e) and (f). The combined losses include the intensity decay due to a distribution of light inside the layer which neither depends on the wavelength nor on the angular distribution. The experimental data are measured at a flat nip cell. (The wavelength dependence of the intensity decay is calculated based on the angular emission spectrum of a real SNOM probe ($\sigma \approx 0.4$))

calculate the field distribution inside and close to a SNOM probe. A more detailed analyses is provided by finite-difference time-domain (FDTD) simulations which are described in the following section.

8.2 FDTD Simulations

In order to confirm the experimental data and to gain insight into the electro-magnetic field distribution inside the investigated layer, finite-difference time-domain (FDTD) simulations are performed. Two different layer stacks are simulated, a *real layer stack model* and a *half space model*. The real layer stack model corresponds to a layer stack equivalent to the measured samples. An 80 nm thin zinc oxide front-contact covers a 1.3 µm µc-Si:H absorber layer which is complemented by a 80 nm thin zinc oxide back-contact and a metal back-reflector. The layer stack is surrounded by a perfectly matched layer (PML) in all spatial directions to realise open boundary conditions. The half-space model excludes the zinc oxide back-contact and the back reflector. The PML is directly attached to the µc-Si:H absorber layer, suppressing any reflections at the rear-side. A comparison between these two models offers information about the origin of light at a certain position as will be discussed later.

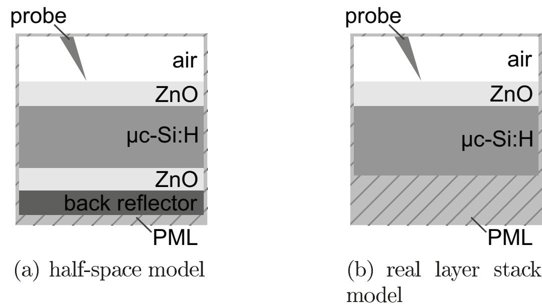

(a) half-space model

(b) real layer stack model

Figure 8.5: Illustration of the simulated layer stacks

In contrast to former simulations [72, 76] which relate to measurements with global illumination, the illumination probe is included in the simulation to model the local illumination of a dual-probe measurement (Chap. 5.2). For reasons, which will be explained later, only the illumination probe is included in the simulation. The probe is modelled as a metallised glass cone with an opening angle of 15°, placed at a distance of about 50 nm above the ZnO layer. The aperture size is set to 160 nm. The light source is implemented as point source placed inside the probe. In correspondence to the experiment, the probe is tilted by 15° and orientated diagonally towards the edges of the simulated

cube.[3] The probe alignment maximises the evaluable light propagation length. As a consequence of the probe tilt, the system loses its rotational symmetry and the polarization of the impinging light has to be taken into account. Hence, the electro-magnetic fields are independently calculated for light linear polarized in the x- and y-direction. The intensity distribution for non-polarised light is the sum of the intensities for both cardinal directions of polarisation.

The simulations were performed with the freely available FDTD software package MEEP [84] which was adapted for this purpose by Ermes [85]. This kind of simulation is highly hardware demanding, since on the one hand, a high resolution of 10 nm is necessary to take small features like the aperture into account. On the other hand, several micrometres of light propagation need to be simulated to allow for a comparison with the measurements. In total, the simulation maps 10 x 10 μm of the layer stack whereby the height is set to 8 μm. The complex electric and magnetic fields have to be calculated for all 10^9 data points of the simulated domain. Therefore, this simulation was performed on the supercomputer Juropa.

Figure 8.6(a) and 8.7(a) display 3D-visualisations of the simulated intensity distributions for non-polarised light. The white dotted line corresponds to the direction at which the detection probe is placed at a dual probe measurement. The intensity distribution at the diagonal plane alongside the white dotted line is displayed in Figure 8.6(b) and Figure 8.7(b), respectively. Points of interest are marked with encircled numbers. The relative intensity directly underneath the aperture (1) is in the order of 10^{-4}. A loss of four or five orders of magnitude in intensity, depending on the aperture size, corresponds well to experiences from measurements.

Comparison with a half space model The simulation of the real layer stack reveals an increased light intensity slightly above the layer surface (4). This intensity can either arise from an undesired direct light-transfer between illumination and detection probe or from light leaving the absorber layer. The difference in the intensity distributions of the real layer and the half-space model allows for a distinction between the two different light-paths. No back-reflector exists at the half-space model. Hence, light which is coupled into the absorber layer has no chance to change its direction of propagation and to return to the front interface. Consequently, if a certain light intensity is apparent above the sample surface, it can not originate from light inside the μc-Si:H layer. Instead, it is directly transmitted from the illumination probe or reflected at the interfaces on top of the absorber layer. Since the half-space model does hardly reveal any light intensity slightly above the surface (Fig. 8.7(b)), a direct transfer of light in between the probes is

[3] For the sake of simplicity, a probe aligned along the z-axis of the simulation domain is placed on top of a tilted layer stack. (This explains the shape of the visualisation shown in Figure 8.6(b) and 8.7(b))

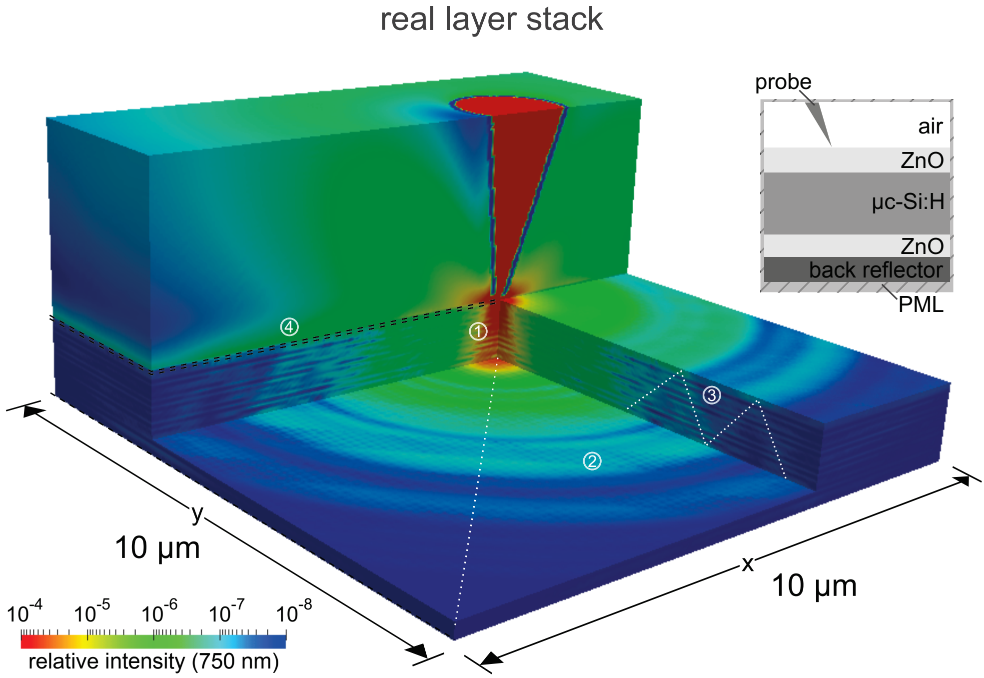

(a) 3D visualisation of the simulated intensity distribution (real layer stack)

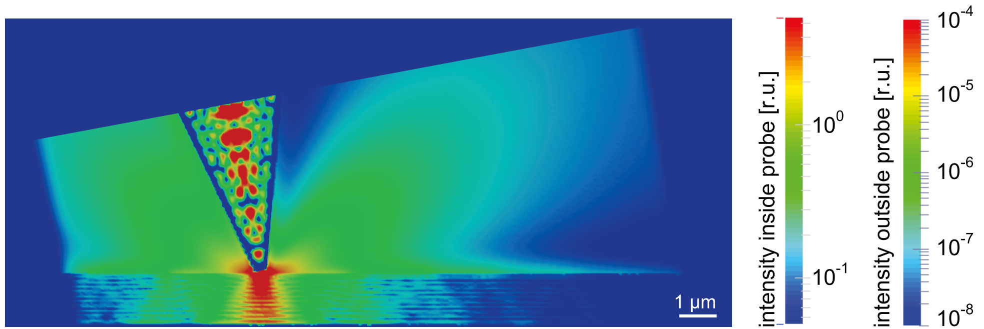

(b) Diagonal slice (real layer stack)

Figure 8.6: Visualisation of the simulated intensity distribution at a real layer stack

not a dominant light path, at least for undamaged perfect probes. Instead, light from the absorber layer is partly transmitted at the front interface where it is measurable by the detection probe.

A distinct feature of the intensity distribution in the real layer stack model, not apparent in the half-space model, is a modulation of the intensity decay, visible as bright rings (2)

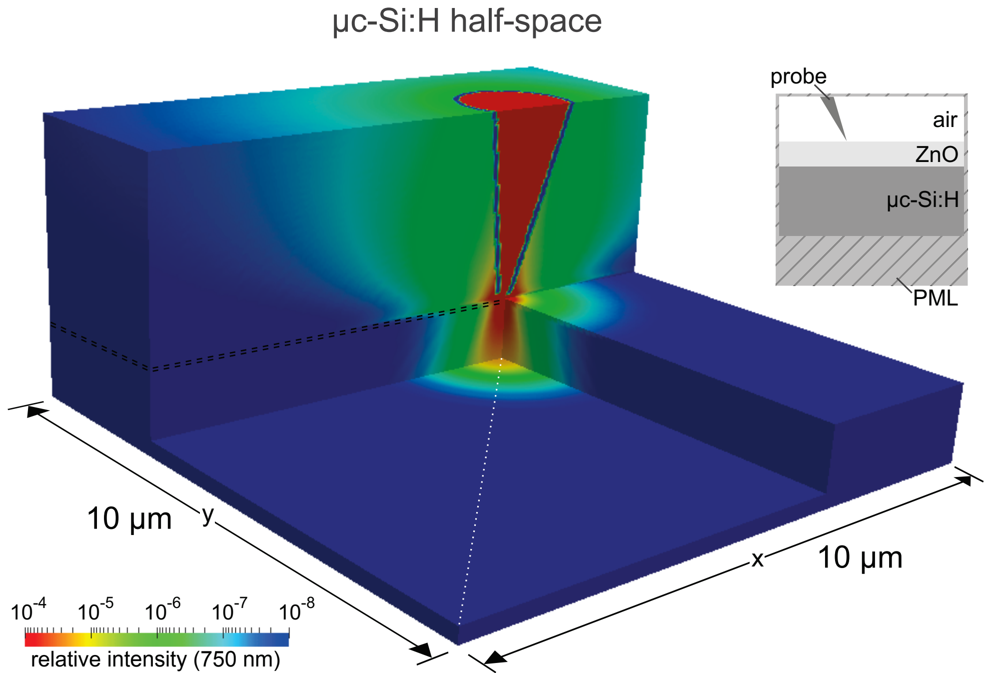

(a) 3D visualisation of the simulated intensity distribution (µc-Si:H half-space)

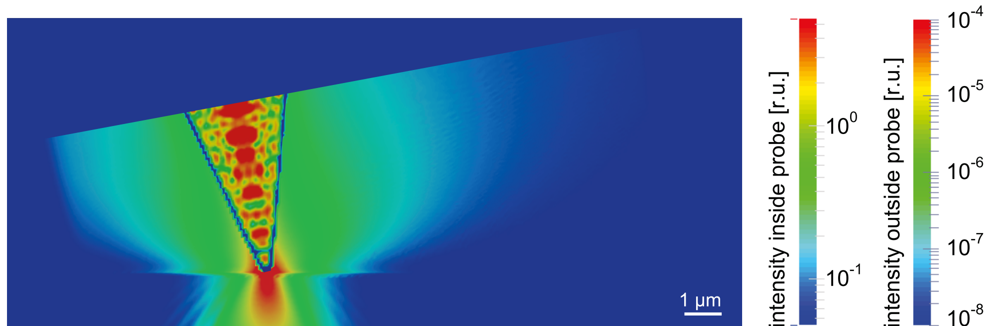

(b) Diagonal slice (µc-Si:H half-space)

Figure 8.7: Visualisation of the simulated intensity distribution at a µc-Si:H half-space

at slices taken parallel to the sample surface (Fig. 8.6(a)). The modulations originate from interferences induced by multiple reflections of light inside the absorber layer (3). Whenever the light is reflected at the front interface, the local intensity is increased.

Comparison with experimental data The experimental data are determined at a dual probe measurement, as described in Chapter 7.2. The presented simulation provide

the three dimensional intensity distribution of light emitted by an illumination probe placed on top of an µc-Si:H layer. However, the detection probe is not included in the model. Although it is in general possible to take the detection probe into account, the required computing time currently exceeds a reasonable range. A single simulation only provides the intensity for a single position of illumination and detection probe. During a measurement the detection probe scans the sample surface in direct vicinity to the illumination probe. An implementation of both probes demands for a single simulation for each position of the detection probe relative to the illumination probe. The high demand in computing time for a single simulation (about 500 CPU hours), currently renders an implementation of the detection probe in the simulation impossible.

In order to compare the simulations with experiments, it has to be discussed how the intensity measured at the sample surface relates to the simulated three dimensional intensity distribution. The measured intensity is proportional to the intensity of light

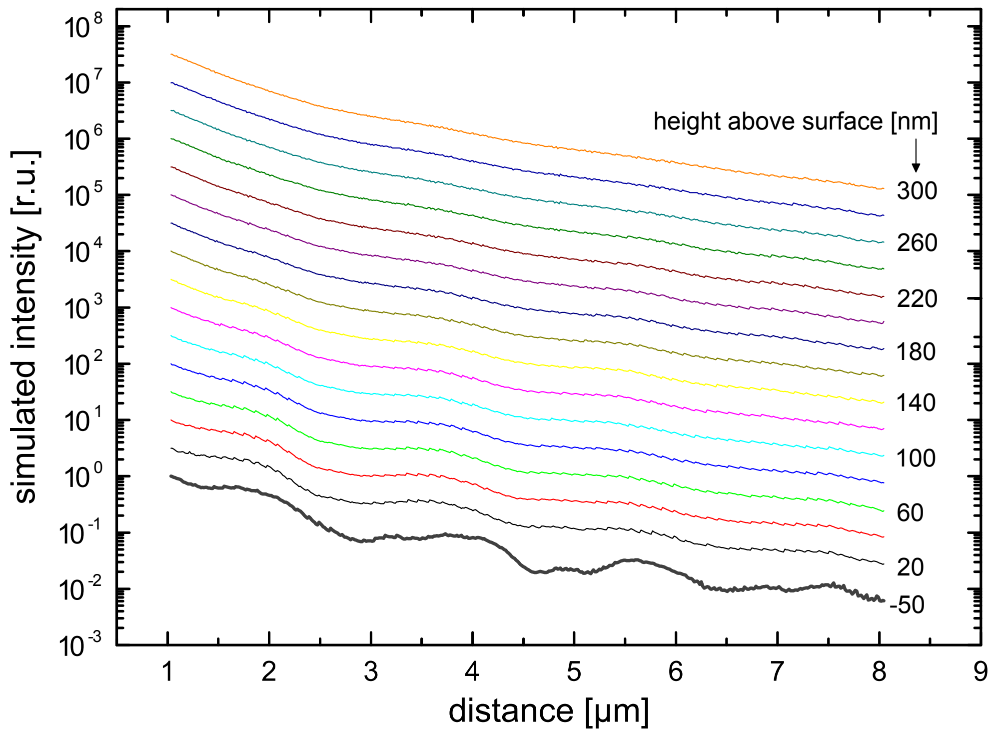

Figure 8.8: Comparison of the intensity extracted from the FDTD simulation at selected heights above the surface (thin lines). Additionally the intensity inside the µc-Si:H layer 50 nm underneath the surface is displayed (thick grey line). (The vertical distance between the plotted intensity decays is only for visualisation)

transmitted through the front-interface (propagating waves) as well as to the intensity of light which is totally reflected at the same interface (evanescent waves). The simulated intensities likewise include propagating and evanescent waves. As a first approach, it is assumed that the measured intensity is proportional to the simulated intensity at a height of 20 nm above the sample surface. In Figure 8.8, the intensity at several heights above the sample surface is displayed. For comparison, the intensity 50 nm beneath the surface is shown as well. Even though the modulation of the intensity is getting less distinct with increasing height, the intensity taken at heights, which are typical for probe-to-surface distances, is to a great extent proportional to the intensity inside the layer. The disappearance of the intensity modulation at heights in the order of half a wavelength might be related to evanescent waves arising from total reflection inside the layer.

In Figure 8.9 the simulated intensity decay is compared to the experimental data and to the simulated intensity decay based on the ray-tracing approach. The simulations consider flat interfaces, the experimental data are determined for flat and textured nip-cells. The minimal probe to probe distance is experimentally limited. Hence, the intensity at small probe to probe distances is exclusively accessible by simulations.

The intensity distribution determined by FTDT simulations reveal a modulation of the intensity decay. As already mentioned, the modulation is most likely based on interference induced by multiple reflections at the front and back interface. The modulations of the intensity decay are visible at dual-probe measurements at flat-interfaces, although

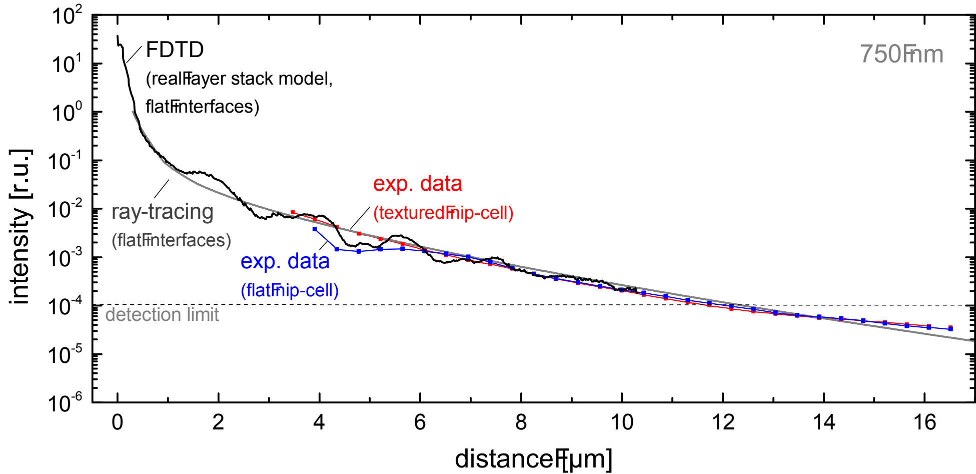

Figure 8.9: Plot of the simulated intensity decay extracted 20 nm above the surface alongside the white dotted line in Fig. 8.6(a). For comparison, the intensity decay based on the ray-tracing approach and experimentally determined data are shown as well.

scattering at small features of the nominally flat surface distort the modulation pattern at longer distances. Accordingly, measurements at samples with textured interfaces do not reveal any modulations of the intensity decay. The ray-tracing approach completely neglects the wave nature of light. Consequently, interference do not occur at this model and a modulation of the intensity decay is not visible.

8.2.1 Limitations of the Simulation

Due to a limitation of the applied simulation software, metals have to be assumed as perfect conductors. Especially the field distribution inside the probe close to the aperture might change, when losses inside the metal coating are taken into account. Although the intention of the simulation is to provide the intensity decay between the probes, rather than the detailed field distribution inside a SNOM probe, a change in the angular emission distribution of the illumination probe will have an influence on the intensity decay. Nonetheless, deviations of real probes from the idealised probe shape implied in the simulations will most likely have a distinctly stronger effect on the probe's emission.

An additional difference between simulation and experiment relates to a change of the electromagnetic field induced by the probe itself. Mainly two effects are imaginable. First, the existence of a metallised detection probe might change the electro-magnetic field close to the probe. In detail, this influence remains unknown until dual-probe simulations become feasible. However, simulations of small idealised structures reveal that the influence is small, especially close to the aperture [85]. Second, a probe placed in near-field distance to the sample surface allows photons to tunnel from the μc-Si:H layer to the probe. Hence, the probe detects the existence of photons which are only apparent at this position because of the presence of the probe. Theoretically, tunnelling photons reduce the light intensity inside the μc-Si:H layer. However, the total amount of energy transferred to the probe is small. Furthermore, the simulation is in good agreement with the measurements, indicating that the intensity decay, extracted from a single-probe simulation, represents the experiment (Fig.8.9).

The presented FTDT simulations relate to measurements performed at samples with flat interfaces. In general, FTDT simulations are able to imply textured interfaces [76]. Hence, in order to simulate dual-probe measurements at textured interfaces, FTDT simulations might be applied as well. However, in case of a textured surface, the position of the illumination probe might have a major influence on the propagation of light. The probe's aperture size is small in relation to the topography features. Hence, the propagation of light might be influenced by the inclination of the surface underneath the probe. Consequently, the propagation of light inside the layer depends on the position of the illumination probe. In Chapter 7.2 a coupling efficiency eliminated scan mode

is introduced which avoids a dependence on the local coupling efficiency by alternating the position of the probes during the measurement. Averaging a statistically sufficient number of illumination and detection positions results in a coupling efficiency eliminated intensity decay. In order to proceed similarly in simulations, multiple simulations are necessary. Further more, the dependence of the intensity decay on the texture demands for simulating different textures. The computation time is tremendous.

8.2.2 Angular Distribution of the SNOM-Probe Emission/Sensitivity

The simulated light distribution in a µc-Si:H half-space (Fig. 8.7(b)) offers access to the angular distribution of the SNOM probe's near-field emission inside of the µc-Si:H layer. Contrary to the far-field emission of a SNOM probe, which is accessible by measuring the intensity distribution at a macroscopic distance with a CMOS-chip (Chap. 4.3), it is difficult to gain the angular distribution of the near-field emission or sensitivity experimentally.

The angular distribution is gained from a line scan along the diagonal of the half-space simulation at a plane parallel to the surface at a distance d_0 of 1250 nm underneath the sample surface (Fig. 8.7(a)). In Figure 8.10, the normalised intensity is plotted versus the

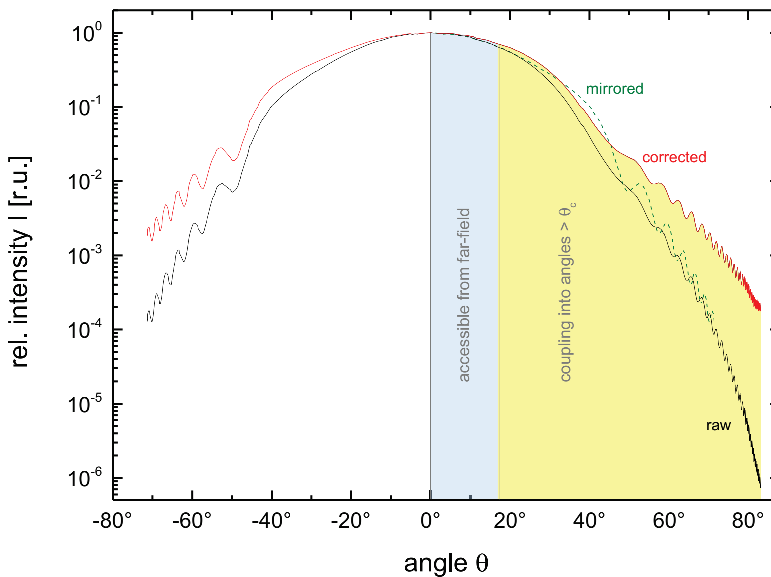

Figure 8.10: Simulated angular distribution of the light emitted by a SNOM probe placed in the near-field of a µc-Si:H surface

angle inside the μc-Si:H layer (black line, labelled "raw"). The probe is tilted by 7.5° in accordance to the experiment in which slightly tilted probes are inevitable to allow for an approaching of the two probes to small distances. As a natural consequence of the probe tilt, the angular distribution is anisotropic. Positive angles in Figure 8.10 relate to the direction towards the second probe. For comparison, the angular distribution at negative angles is added as mirror image.

The translation of an intensity given in a plane into an angular intensity distribution demands for several corrections. First of all, the distance d of a pixel in the plane from the probe's aperture is not constant. The area illuminated under the same solid angle increases and has to be corrected by $d^2 \propto 1/cos^2(\beta)$. Furthermore, an increase in the probe-to-pixel distance also increases the absorption inside the μc-Si:H layer. The superposition of the angular distribution of the SNOM probe by the intensity decay due to absorption requires a correction factor $e^{\alpha d}$. Additionally, the angle between the aperture and different pixels along the line scan is not constant which needs to be corrected by $1/cos(\beta)$. In total the intensity is corrected by

$$I(\theta)_{cor} = I(\theta)_{raw} \cdot \frac{e^{\alpha d}}{cos^3(\beta)} \tag{8.2}$$

In contrast to a far-field illumination, a SNOM probe placed in the sample's near-field is capable of coupling light into angles not accessible from the outside (yellow area in Figure 8.10, mind the logarithmic scale).

Finally, the intensity extracted from a single line scan is transferred to the *Angular Intensity Distribution* ($\mathrm{AID_{Si}}$) by spherical integration. The AID stands for the total intensity of scattered light per angular element whereby the subscript "Si" relates to a distribution inside of μc-Si:H.

$$AID_{Si}(\theta) = I(\theta)_{cor} \cdot sin(\theta) \tag{8.3}$$

Figure 8.11 displays the AID_{Si} at a wavelength of 750 nm of a SNOM probe placed at subwavelength distance on top of the layer stack alongside a set of Gaussian distributions with several standard deviations σ (Chap. 8.1.1). Additionally, the angular resolved emission of typical textured front- and back-interfaces, as they are used at our institute (Chap. 2.7), are shown. For each intensity distribution, the share of intensity scattered in angles beyond the critical angle (depicted by the dashed vertical line in Fig. 8.11) is displayed in Figure 8.12. In terms of light propagation inside a layer, the angular distribution at angles beyond the critical angle is crucial, since the intensity of rays at low angles decreases strongly and hardly contributes to the intensity at distances which are

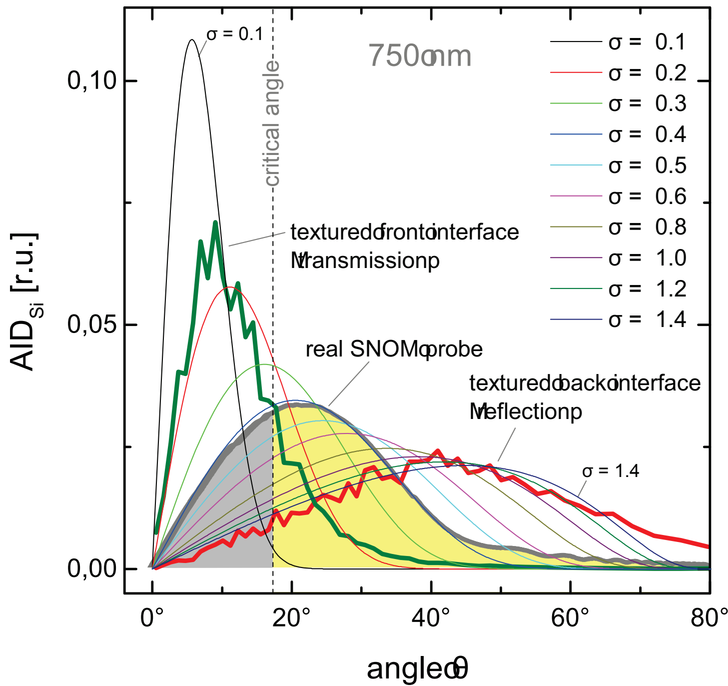

Figure 8.11: Angular intensity distribution (AID_{Si}) of the emitted light intensity by a SNOM probe into an µc-Si:H half space and several Gaussian distributions with different standard deviations σ (described in Chap. 8.1.1), besides the scattering profiles of a textured front and back-interface [54]. The dashed vertical line marks the angle of total reflection.

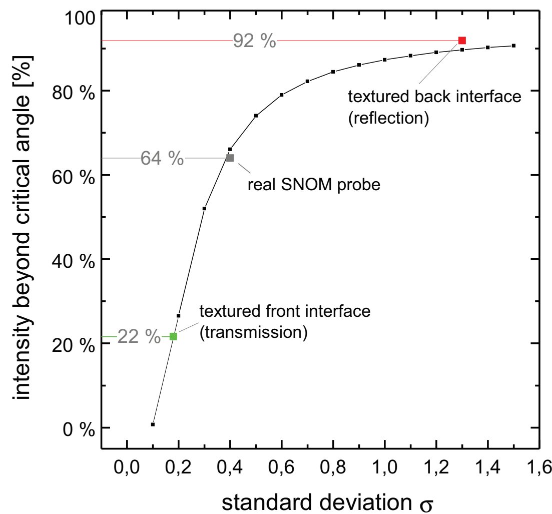

Figure 8.12: Integrated intensity at angles beyond the angle of total reflection, calculated for the angular intensity distributions presented in Fig. 8.11.

experimentally accessible (Fig. 8.3(c)). The angular intensity distribution of the SNOM probe reveals that 64 % of the emitted light intensity is scattered into angles beyond the angle of total reflection. The AID_{Si} of the SNOM probe resembles a Gaussian distribution with a standard deviation σ of 0.4 (Fig. 8.11). Figure 8.12 exhibits how a change in the AID_{Si} of the SNOM probe towards a Gaussian distribution with smaller or larger standard deviation influences the share in intensity emitted at an angle beyond the critical angle. For comparison, Figure 8.12 provides the AID_{Si} of a typical textured front and back interface as well. The centre of the AID_{Si} of the SNOM probe is in between those of the textured interfaces. Hence, the angular distribution of light emitted by a SNOM probe placed in subwavelength distance to the surface is, in terms of its shape and position of the maximum, comparable to the angular distribution which can be achieved by textured surfaces.

In detail, the angular distribution of a SNOM probe strongly depends on the probe's structure, especially close to the aperture. Small deviations from a symmetrically shaped aperture, impurities in the metal coating or particles collected by the probe during the scanning procedure might have a significant influence on the angular distribution of the emitted light. Furthermore, uncertainties in the probe to sample distance might influence the angular distributions as well. The angular distribution displayed in Figure 8.11 is based on the simulation of a perfect idealized SNOM probe. Deviations of the SNOM probes from the idealized shape are not taken into account. In order to minimize the influence of the aperture's shape, each probe is thoroughly tested at least in terms of its far-field emission characteristic (Chap. 4.4).

Despite of deviations between the simulated and the real probe structure, the ray-tracing simulations based on the calculated angular distribution are in good agreement with the experimental results (Fig. 8.3(a)).

9 Summary & Outlook

9.1 Summary

In this work, the light propagation in microcrystalline silicon thin film solar cells is investigated. For this purpose, a dual-probe scanning near-field optical microscope (SNOM) was developed and set up from scratch. The microscope is equiped with two separated probes for local illumination and detection on a subwavelength scale. Applying newly developed modes of measurement, exclusively available at dual probe SNOMs, the microscope allows for measuring the propagation of light in thin layers with high precision.

Within the framework of this thesis, the different physical challenges of dual probe scanning near-field optical microscopy are outlined and the technological solutions are described. The reliability of the setup was thoroughly tested at measurements of light propagation in flat and textured microcrystalline silicon (μc-Si:H) thin film solar cells in nip-configuration. The measured raw data are analysed by multiple methods. It is observed, that the lateral intensity decay of light is strongly influenced by local surface features. Therefore, an advanced dual-probe scan mode is introduced which compensates for the non-constant coupling efficiencies, caused by local surface features.

In dual-probe operation, only a small share of the photons emitted by the illumination probe finally reaches the detection probe. Hence, the different loss mechanisms, which are accounted for the strong attenuation of the propagating light, are theoretically investigated by means of a ray-tracing approach. Ray-tracing allows to examine the loss mechanisms separately. The simulation reveals, that for a wavelength of 750 nm the intensity decay within the first 5 μm is dominated by the radial distribution of light inside the layer. At longer distance, absorption is the major mechanism for a decrease in light intensity. The intensity decay due to a transmittance at the front interface strongly attenuates the propagation of light with small angles of incidence. Although ray-tracing neglects the wave nature of light, the approach is capable to reproduce the lateral intensity decay of light propagating in a 1 μm thick μc-Si:H layer.

The ray-tracing approach is supplemented with finite-difference time-domain (FDTD) simulations which provide the field distribution on a sub-wavelength scale. By including the illumination probe to the simulated layer stack, an improved compliance of simulation

and experiment is achieved. Based on the FDTD simulation, the light distribution inside and above the layer stack is investigated and compared to a half-space model which represents a system without light-trapping properties. It is demonstrated, that at least for undamaged, perfect probes, a direct light transfer between illumination and detection probe, bypassing the absorber layer, is negligible.

Furthermore, the FDTD simulations provide the angular distribution of the light emitted by a SNOM probe, placed at subwavelength distance above the surface. Thereby, the simulations complement the experimentally determined angular resolved far-field emission characteristic of a probe in air. It is shown that a large share of 64 % of the light intensity emitted by a SNOM probe, placed at subwavelength distance above a μc-Si:H absorber layer, is coupled into angles which exceeds the angle of total reflection.

Finally, the intensity decay of the propagating light, determined by FDTD simulations, revealed good accordance with the measured data. A modulation of the intensity decay, which originates from interference induced by multiple reflections, is observed in the measurement as well as in FDTD simulations. The good compliance between simulation and experiment indicates that macroscopic absorption coefficients are suitable for the description of light propagation even on microscopic scales.

9.2 Outlook

Periodic Gratings A promising light-trapping concept is the use of plasmonic gratings which apply the coupling of light to plasmonic resonances to guide and localise the incident light with low losses. First SNOM measurements at plasmonic gratings were already performed based on samples provided by Paetzold [49]. SNOM measurements at these samples reveal a periodic intensity modulation. This might be due to grating effects but can as well be induced by topography artefacts (Chap. 7.3). A probe placed on top of a bump will have a different coupling efficiency than one placed between the bumps at a flat surface. It's a challenge to distinguish between the optical features based on the plasmonic grating and optical artefacts with the same periodicity. Measurements at the edge of the periodic pattern and the flat surrounding surface might reveal guided optical modes without the influence of topography effects.

Nano Particles The usage of nano particles is one approach of third generation devices which promise to increase efficiency. Macroscopic characterisation methods are limited to the investigation of a large ensemble of particles. On the contrary, near-field microscopes are theoretically capable of investigating single particles and measuring scattering properties, photoluminescence as well as charge carrier extraction. Unfortunately, scanning probe measurements at surfaces covered with particles often results in a collection of the particles at the probe. This difficulty is not particularly restricted to SNOM measure-

ments but occur as well at other scanning probe methods, like conductive AFM. If the particles are stronger attached to the surface, e.g. by partly embedding the particles into a layer, it should be feasible to perform SNOM measurements at this kind of samples.

Polarisation Dependent Measurements In case of a globally illuminated randomly textured surface, the large number of simultaneously illuminated surface features average any polarisation dependence. The local illumination, applied in dual-probe operation, implies that the illuminated area is small in comparison to the size of the surface features. Hence, the illumination might be restricted to a single wall of a crater. As a result, the propagation of light, emitted by the illumination probe, potentially depends on the direction of polarisation. Principally, it is possible to perform polarisation dependent SNOM measurements. However, a SNOM probe, especially one with asymmetrical aperture, might change the polarisation of the incident light. Hence, even if the polarisation of the light coupled into the illumination probe is known, the light, which is actually coupled into the sample surface, might be polarised differently. A sophisticated probe characterisation could help to solve this problem.

The introduced ray-tracing algorithm is currently restricted to flat interfaces, since it is difficult to calculate the reflectance at a textured surface with sub-wavelength size features. A FDTD simulation, similar to the one presented in Chapter 8.2, but with textured surfaces, could provide information about the polarisation dependency. Nonetheless, the requirement for testing different positions of the illumination probe will demand for a high computing time.

Electrical Measurements As a future project, it might be interesting to extend the capabilities of the dual-probe SNOM to electrical measurements. Electrical single-, as well as dual-probe modes, are conceivable. In electrical single-mode operation, the sample is locally illuminated by the illumination probe while the photo current is measured. Due to the extremely small illuminated area, it will be a challenge to measure the tiny photo currents. In electrical dual-probe mode, the photo current is measured locally by an conducting probe. The currently applied shear-force distance control is a non-contact method. However, as a first step it is imaginable to place a conducting probe at a constant position of the sample surface, while an illumination probe scans the adjacent surface area. This way a local photo current is measured.

Zusammenfassung

In dieser Arbeit wird die Lichtausbreitung in mikrokristallinen Silizium Dünnschicht Solarzellen untersucht. Für diesen Zweck wurde ein optisches zwei Spitzen Nahfeld-Mirkoskop (SNOM[1]) entwickelt und aufgebaut. Das Mikroskop ist mit zwei getrennten Spitzen ausgestattet, welche eine lokale Beleuchtung und Detektion auf Sub-Wellenlängen Skalen ermöglichen. Durch Verwendung neuer Mess-Verfahren, welche ausschließlich an zwei-Spitzen SNOMs verfügbar sind, kann die Lichtausbreitung in dünnen Schichten mit hoher Präzision gemessen werden.

Im Rahmen dieser Arbeit werden die verschiedenen technischen Herausforderungen der Zwei-Spitzen-Nahfeldmikroskopie erläutert und technische Lösungen gezeigt. Die Zuverlässigkeit des Aufbaus wurde gründlich an Messungen der Lichtführung in flachen und texturierten mikrokristallinen Silizium Dünnschicht Solarzellen in nip-Konfiguration getestet. Die gemessenen Rohdaten wurden mit verschiedenen Verfahren ausgewertet. Dabei wurde beobachtet, dass die Abnahme der Lichtintensität in Schichtrichtung stark von lokalen Oberflächen Strukturen beeinflusst wird. Daher wurde ein neuartiger Zwei-Spitzen Scanmodus entwickelt, welcher die durch lokale Strukturen bedingten nicht konstanten Kopplungseffizienten kompensiert.

Im Zwei-Spitzen Betrieb erreicht nur ein kleiner Teil der von der Beleuchtungsspitze emittierten Photonen letztendlich die Detektionsspitze. Daher werden die verschiedenen Verlustmechanismen, welche für die starke Dämpfung des propagierenden Lichts verantwortlich sind, mittels eines ray-tracing[2] Ansatzes untersucht. Ray-tracing erlaubt es die verschiedenen Verlustmechanismen separat zu untersuchen. Die Simulation zeigt, dass für eine Wellenlänge von 750 nm der Intensitätsabfall innerhalb der ersten 5 µm von der radialen Verteilung des Lichts in der Schicht dominiert wird. In größerem Abstand ist die Absorption der Hauptmechanismus für eine Abnahme der Lichtintensität. Die Lichtführung von Strahlen mit kleinem Einfallswinkel wird stark durch die hohe Transmission am Front-Interface gedämpft. Obwohl ray-tracing die Wellennatur des Lichtes vernachlässigt, ist der Ansatz in der Lage, den lateralen Intensitätsabfall in einer 1 µm dicken µc-Si:H Schicht zu reproduzieren.

[1] SNOM - Scanning Near-field Optical Microscope
[2] deut. Strahlverfolgung

Der ray-tracing Ansatz wird ergänzt durch Simulationen mittels der Finite-Differenzen-Methode im Zeitbereich (FDTD[3]), welche die Feld-Verteilung auf Sub-Wellenlängenskala wiedergibt. Durch Einbeziehung der Beleuchtungs-Spitze in den simulierten Schicht-Stapel, konnte eine verbesserte Übereinstimmung von Simulation und Experiment erzielt werden. Auf Basis der FDTD Simulationen wird die Licht-Verteilung innerhalb und oberhalb des Schichtstapels untersucht und mit einem Halbraum-Modell verglichen, welches ein System ohne light-trapping[4] Eigenschaften darstellt. Es wird gezeigt, dass zumindest für unbeschädigte, ideale Spitzen ein direkter Licht-Transfer zwischen Beleuchtungsspitze und Detektionsspitze, unter Umgehung der Absorber-Schicht, vernachlässigbar ist.

Des Weiteren bieten die FDTD-Simulationen Zugang zu der Winkelverteilung der Emission einer, in Sub-Wellenlängenabstand über einer Oberfläche platzierten, SNOM-Spitze. Hierbei ergänzen die Simulationen die experimentell bestimmte Emissions-Charakteristik in Luft im Fernfeld. Es wird gezeigt, dass eine SNOM Spitze, die in Sub-Wellenlängenabstand zu einer µc-Si:H Schicht platziert ist, einen großen Anteil von 64 % der Intensität unter Winkeln einkoppelt, die größer als der Totalreflexionswinkel sind.

Der mittels FDTD-Simulationen bestimmte Intensitätsabfall zeigt eine gute Übereinstimmung mit den gemessenen Daten. Eine Modulation des Intensitätsabfalls, welcher durch Interferenzen verursacht wird, die durch Mehrfach-Reflexionen in der Schicht entstehen, wird sowohl in den FDTD-Simulationen beobachtetet, als auch im Experiment. Die gute Übereinstimmung zwischen Simulation und Experiment zeigt, dass makroskopische Absorptionskoeffizienten geeignet sind, um die Lichtausbreitung auch auf mikroskopischen Skalen zu beschreiben.

[3] FDTD - Finite-Difference Time-Domain
[4] deut. Licht-Einfang

References

[1] M. Eddy, "Energy Price Increases Pose Challenge for Merkel," *The New York Times*, 2012.

[2] "Germany's energy transformation Energiewende," *The Economist*, 2012.

[3] P. Hockenos, "The Energiewende," *die Zeit*, 47, 2012.

[4] K. Bittkau and T. Beckers, "Special Issue: 23rd International Conference on Amorphous and Nanocrystalline Semiconductors (ICANS 23)," *Phys. Status Solidi A*, 207:493–767, 2010.

[5] L. Novotny, "The history of near-field optics," volume 50 of *Progress in Optics*, pages 137 – 184, Elsevier, 2007, doi:http://dx.doi.org/10.1016/S0079-6638(07)50005-3.

[6] T. Schmid, T. A. Schmitz, P. D. Setz, et al., "Methods for molecular nanoanalysis," *Chimia*, 60(11):A783–A788, 2006, doi:10.2533/chimia.2006.783.

[7] J. Hsu, "Near-field scanning optical microscopy studies of electronic and photonic materials and devices," *Material Science & Engineering R-Reports*, 33(1):1–50, 2001.

[8] Y. Toda, M. Kourogi, M. Ohtsu, et al., "Spatially and spectrally resolved imaging of GaAs quantum-dot structures using near-field optical technique," *Applied Physics Letters*, 69(6):827–829, 1996, doi:10.1063/1.117905.

[9] E. Betzig, J. Trautman, R. Wolfe, et al., "Near-field Magnetooptics and High-density Data-storage," *Applied Physics Letters*, 61(2):142–144, 1992.

[10] T. Beckers, *Untersuchung optischer Nanostrukturen für die Photovoltaik mit Nahfeldmikroskopie*, Ph.D. thesis, RWTH Aachen, 2010.

[11] T. Beckers, K. Bittkau, C. Rockstuhl, et al., "The optical near-field of randomly textured light trapping structures for thin-film solar cells," in "Photonics for Solar Energy Systems II," Proceedings of the Society of Photo-Optical Instrumentation Engineers (SPIE), 2008.

[12] L. Bergmann and C. Schaefer, *Optik*, de Gruyter, Berlin, 10 edition, 2004.

[13] E. Hecht, *Optik*, Oldenbourg Wissenschaftsverlag, 2009.

[14] L. Novotny and B. Hecht, *Principles of nano-optics*, Cambridge Univ. Press,, Cambridge, 2006.

[15] P. J. Moyer, *Development, Physics, and Applications of near-field scanning optical microscopy*, Ph.D. thesis, North Carolina State University, 1993.

[16] W. Demtröder, *Laserspektroskopie 2*, Springer, Berlin, 6. edition, 2013.

[17] P. D. R. Gross, "Lecture Notes to "Physics 3" (WS 2001/2002 and WS 2002/2003)," http://www.wmi.badw.de/teaching/Lecturenotes/, walther-Meißner-Institut (WMI), Bayerische Akademie der Wissenschaften.

[18] D. A. Recknagel, *Optik*, VEB Verlag Technik, Berlin, 1986.

[19] H. Bethe, "Theory of diffraction by small holes," *Physical Review*, 66(7/8):163–182, OCT 1944, doi:10.1103/PhysRev.66.163.

[20] C. BOUWKAMP, "On Bethes Theory of Diffraction by Small Holes," *Philips Research Reports*, 5(5):321–332, 1950.

[21] C. Bouwkamp, "Diffraction Theory," *Reports on Progress in Physics*, 17:35–100, 1954, doi:10.1088/0034-4885/17/1/302.

[22] S. A. Maier, *Plasmonics fundamentals and applications*, Springer, Berlin, 2007.

[23] G. P. Alberto M. Marino, "Diffraction by a Small Circular Aperture," *Lecture on nano-optics given by of Lukas Novotny at the ETH Zürich*.

[24] D. Domine, F. J. Haug, C. Battaglia, et al., "Modeling of light scattering from micro- and nanotextured surfaces," *Journal of Applied Physics*, 107(4):8, 2010.

[25] R. D. Guenther, *Modern optics*, Wiley, New York, 1990.

[26] O. Vetterl, A. Lambertz, A. Dasgupta, et al., "Thickness dependence of microcrystalline silicon solar cell properties," *Solar Energy Materials and Solar Cells*, 66(1–4):345 – 351, 2001, doi:http://dx.doi.org/10.1016/S0927-0248(00)00193-8.

[27] D. Staebler and C. Wronski, "Reversible conductivity changes in discharge-produced amorphous Si," *Applied Physics Letters*, 31(4):292–294, 1977.

[28] P. Bermel, C. Luo, L. Zeng, et al., "Improving thin-film crystalline silicon solar cell efficiencies with photonic crystals," *Optics Express*, 15(25):16986–17000, 2007.

[29] C. Haase and H. Stiebig, "Optical properties of thin-film silicon solar cells with grating couplers," *Progress in Photovoltaics: Research and Applications*, 14(7):629–641, 2006.

[30] U. Paetzold, E. Moulin, D. Michaelis, et al., "Plasmonic reflection grating back contacts for microcrystalline silicon solar cells," *Applied Physics Letters*, 99(18), 2011.

[31] P. Spinelli, V. E. Ferry, J. van de Groep, et al., "Plasmonic light trapping in thin-film Si solar cells," *Journal of Optics*, 14(2, SI), 2012, doi:10.1088/2040-8978/14/2/024002.

[32] E. Yablonovitch, "Statistical ray optics," *J. Opt. Soc. Am.*, 72:899–907, 1982.

[33] P. D. U. Rau, "Lecture on Photovoltaic (WS2012/2013)," .

[34] E. Yablonovitch and G. D. Cody, "Intensity enhancement in textured optical sheets for solar cells," *IEEE Transactions on Electron Devices*, 29(2):300 – 305, 1982, doi: 10.1109/T-ED.1982.20700.

[35] C. Ulbrich, *Spectral and directional dependence of light-trapping in solar cells*, Ph.D. thesis, RWTH Aachen, 2011.

[36] T. Tiedje, E. Yablonovitch, G. D. Cody, et al., "Limitting Efficiency of Silicon Solor Cells," *IEEE Transactions on Electron Devices*, ED-31(5):711–716, 1984.

[37] G. 03e1 Standard Tables for Reference Solar Spectral Irradiances: Direct Normal and A. I. Hemispherical on 37 degree Tilted Surface.

[38] Z. Yu, A. Raman, and S. Fan, "Fundamental limit of light trapping in grating structures," *Optics Express*, 18(19):A366–A380, 2010.

[39] S. Hoppe, G. Ctistis, J. Paggel, et al., "Spectroscopy of the shear force interaction in scanning near-field optical microscopy," *Ultramicroscopy*, 102(3):221–226, 2005, doi:10.1016/j.ultramic.2004.10.002.

[40] J. D. van der Waals, *Over de Continuiteit van den Gas- en Vloeistoftoestand*, Ph.D. thesis, Universität Leiden, 1873.

[41] M. K. Hans-Jürgen Butt, *Surface and Interfacial Forces*, Wiley-VCH, 2010.

[42] J. Schmidt, H. Bergander, and L. Eng, "Experimental and theoretical analysis of shear-force interaction in the non-contact regime with 100 pN force resolution," *Applied Surface Science*, 157(4):295–301, 2000, doi:10.1016/S0169-4332(99)00542-5, 2nd International Workshop on Noncontact Atomic Force Microscopy (NC-AFM 99), Pontresina Switzerland, SEP 01-04, 1999.

[43] F. F. Froehlich and T. D. Milster, "Mechanical resonance behavior of near-field optical microscope probes," *Applied Physics Letters*, 70(12):1500–1502, 1997.

[44] P. Moyer and M. Paesler, "Shear Force Reflection Near-Field Scanning Optical Microscopy," in C. Williams, editor, "Scanning Probe Microscopies II," volume 1855 of *Proceedings of the Society of Photo-Optical Instrumentation Engineers (SPIE)*, pages 58–66, SOC Photo Opt Instrumentat Engineers, 1993, doi:10.1117/12.146363.

[45] R. L. Williamson, L. J. Brereton, M. Antognozzi, et al., "Are artefacts in scanning near-field optical microscopy related to the misuse of shear force?" *Ultramicroscopy*, 71(1-4):165–175, 1998.

[46] E. Ayars, D. Aspnes, P. Moyer, et al., "Proximal electromagnetic shear forces," *Journal of Microscopy-Oxford*, 196(Part 1):59–60, 1999.

[47] K. Karrai and I. Tiemann, "Interfacial shear force microscopy," *Physical Review B*, 62(19):13174 – 13181, Nov 2000.

[48] I. Smolyaninov, W. Atia, S. Pilevar, et al., "Experimental study of probe-surface interaction in near-field optical microscopy," *Ultramicroscopy*, 71(1-4):177–182, 1998, doi:10.1016/S0304-3991(97)00098-3, 4th International Conference on Near-Field Optics and Related Techniques, Jerusalem,Israel, FEB 09-13, 1997.

[49] U. W. Paetzold, *Light trapping with plasmonic back contacts in thin-film silicon solar cells*, Ph.D. thesis, RWTH Aachen, 2012.

[50] W. Boettler, V. Smirnov, A. Lambertz, et al., "Window layer development for microcrystalline silicon solar cells in n-i-p configuration," in "Physica Status Solidi C - Current Topics in Solid State Physics, Vol 7 No 3-4," volume 7 of *Physica Status Solidi C-Current Topics in Solid State Physics*, pages 1069–1072, 2010, doi:10.1002/pssc.200982833, 23rd International Conference on Amorphous and Nanocrystalline Semiconductors (ICANS23), Utrecht, Netherlands, AUG 23-28, 2009.

[51] F.-J. Haug, T. Söderström, O. Cubero, et al., "Plasmonic absorption in textured silver back reflectors of thin film solar cells," *Journal of Applied Physics*, 104(6), 2008, doi:10.1063/1.2981194.

[52] E. Moulin, U. Paetzold, J. Kirchhoff, et al., "Study of detached back reflector designs for thin-film silicon solar cells," *Physica Status Solidi - Rapid Research Letters*, 6(2):65–67, 2012, doi:10.1002/pssr.201105463.

[53] E. Moulin, U. Paetzold, K. Bittkau, et al., "Investigation of the impact of the rear-dielectric/silver back reflector design on the optical performance of thin-film silicon solar cells by means of detached reflectors," *Progress in Photovoltaics: Research and Applications*, 21(5):1236–1247, 2013, doi:10.1002/pip.2355.

[54] K. Bittkau, W. Boettler, M. Ermes, et al., "Light scattering at textured back contacts for n-i-p thin-film silicon solar cells," *Journal of Applied Physics*, 111(8), 2012, doi: 10.1063/1.3703572.

[55] Rychen, "Piezoeletric Quartz Tunning Forks for Scanning Probe Microscopy," *Nanonis GmbH, Switzerland*, 1111.

[56] A. Ruiter, K. van der Werf, J. Veerman, et al., "Tuning fork shear-force feedback," *Ultramicroscopy*, 71(1-4):149–157, 1998, doi:10.1016/S0304-3991(97)00111-3, 4th International Conference on Near-Field Optics and Related Techniques, Jerusalem, Israel, FEB 09-13, 1997.

[57] W. A. Atia and C. C. Davis, "A phase-locked shear-force microscope for distance regulation in near-field optical microscopy," *Applied Physics Letters*, 70(4):405–407, 1997.

[58] K. Hsu and L. Gheber, "Tip-sample interaction in a "shear-force" near-field scanning optical microscope," *Review of Scientific Instruments*, 70(9):3609–3613, 1999, doi: 10.1063/1.1149967.

[59] C. Durkan and I. V. Shvets, "Investigation of the physical mechanisms of shear-force imaging," *Journal of Applied Physics*, 80(10):5659–5664, 1996.

[60] G. Behme, A. Richter, M. Suptitz, et al., "Vacuum near-field scanning optical microscope for variable cryogenic temperatures," *Review of Scientific Instruments*, 68(9):3458–3463, 1997.

[61] P. Hoffmann, B. Dutoit, and R.-P. Salathé, "Comparison of mechanically drawn and protection layer chemically etched optical fiber tips," *Ultramicroscopy*, 61:165 – 170, 1995, doi:10.1016/0304-3991(95)00122-0.

[62] Turner, "Etch procedure for optical fibers," 1984.

[63] R. Stockle, C. Fokas, V. Deckert, et al., "High-quality near-field optical probes by tube etching," *Applied Physics Letters*, 75(2):160–162, 1999.

[64] J. Veerman, A. Otter, L. Kuipers, et al., "High definition aperture probes for near-field optical microscopy fabricated by focused ion beam milling," *Applied Physics Letters*, 72(24):3115–3117, 1998, doi:10.1063/1.121564.

[65] C. Adelmann, J. Hetzler, G. Scheiber, et al., "Experiments on the depolarization near-field scanning optical microscope," *Applied Physics Letters*, 74(2):179–181, 1999, doi:10.1063/1.122997.

[66] J. D. Jackson, *Klassische Elektrodynamik*, Walter de Gruyter, 1999.

[67] D. N. Davydov, K. B. Shelimov, T. L. Haslett, et al., "A near-field scanning optical microscope with a high Q-factor piezoelectric sensing element," *Applied Physics Letters*, 75(12):1796–1798, 1999, doi:10.1063/1.124823.

[68] A. Ruiter, J. Veerman, K. vanderWerf, et al., "Dynamic behavior of tuning fork shear-force feedback," *Applied Physics Letters*, 71(1):28–30, 1997, doi:10.1063/1.119482.

[69] K. Karrai and R. Grober, "Piezoelectric Tip-sample Distance Control For Near-field Optical Microscopes," *Applied Physics Letters*, 66(14):1842–1844, 1995.

[70] M. Schneemann, *Mikroskopische Untersuchungen der Sperrspannungselektrolumineszenz von (multi-) kristallinen Siliziumsolarzellen*, Ph.D. thesis, RWTH Aachen, 2011.

[71] K. Bittkau, T. Beckers, S. Fahr, et al., "Nanoscale investigation of light-trapping in a-Si:H solar cell structures with randomly textured interfaces," *Physica Status Solidi A - Applications and Material Science*, 205(12, Sp. Iss. SI):2766–2776, 2008, doi:10.1002/pssa.200880454.

[72] C. Rockstuhl, S. Fahr, F. Lederer, et al., "Local versus global absorption in thin-film solar cells with randomly textured surfaces," *Applied Physics Letters*, 93(6), 2008, doi:10.1063/1.2965117.

[73] A. Hoffmann, K. Bittkau, T. Beckers, et al., "Investigation of local light scattering properties of SnO_2 substrates in amorphous silicon cells," in "Proceedings of the 26. EUPVSEC," 2011.

[74] K. Bittkau, M. Schulte, M. Klein, et al., "Modeling of light scattering properties from surface profile in thin-film solar cells by Fourier transform techniques," *Thin Solid Films*, 519(19):6538–6543, 2011, doi:10.1016/j.tsf.2011.04.122.

[75] A. E. Klein, N. Janunts, A. Tuennermann, et al., "Investigation of mechanical interactions between the tips of two scanning near-field optical microscopes," *Applied Physics B-Lasers and Optics*, 108(4):737–741, 2012, doi:10.1007/s00340-012-5182-7.

[76] C. Rockstuhl, F. Lederer, K. Bittkau, et al., "Light localization at randomly textured surfaces for solar-cell applications," *Applied Physics Letters*, 91(17), 2007, doi:10.1063/1.2800374.

[77] "SNOM Tool" (inhouse developed versatile analysis software for SNOM and AFM measurements created by Karsten Bittkau).

[78] J.-H. Lambert, *Photometria*, 1760.

[79] B. Hecht, H. Bielefeldt, Y. Inouye, et al., "Facts and artifacts in near-field optical microscopy," *Journal of Applied Physics*, 81(6):2492–2498, 1997, doi:10.1063/1.363956.

[80] M. Ermes, S. Lehnen, K. Bittkau, et al., "Reconstruction of SNOM near-field images from rigorous optical simulations by including topography artifacts," *Proceedings of SPIE - The International Society for Optical Engineering*, 8789, 2013.

[81] M. Schulte, K. Bittkau, K. Jäger, et al., "Angular resolved scattering by a nano-textured ZnO/silicon interface," *Applied Physics Letters*, 99(11):111107, 2011, doi:10.1063/1.3640238.

[82] K. Jager and M. Zeman, "A scattering model for surface-textured thin films," *Applied Physics Letters*, 95(17):171108, 2009, doi:10.1063/1.3254239.

[83] A. Krywonos, J. E. Harvey, and N. Choi, "Linear systems formulation of scattering theory for rough surfaces with arbitrary incident and scattering angles," *Journal of the Optical Society of America A-Optics Image Science and Vision*, 28(6):1121–1138, JUN 2011.

[84] A. F. Oskooi, D. Roundy, M. Ibanescu, et al., "MEEP: A flexible free-software package for electromagnetic simulations by the FDTD method," *Computer Physics Communications*, 181(3):687–702, 2010, doi:10.1016/j.cpc.2009.11.008.

[85] A. M. Ermes, *Optical near-field investigations of photonic structures for application in silicon-based thin-film solar cells*, Ph.D. thesis, RWTH Aachen, 2013.

Acknowledgments

Last but not least, I would like to thank everyone, who contributed to this work. Special thanks goes to

Prof. Dr. Uwe Rau for supervising this work.

Prof. Dr. Reinhard Carius for the enduring support during my diploma and doctoral thesis.

Karsten Bittkau for his superb supervision of this thesis and for always having an answer to all theoretical, programming and experimental concerns. Not to mention his unique sense of humour.

Ulrich Paetzold for providing the investigated samples and many valuable advices and discussions.

Markus Ermes for performing simulations at the Jülich supercomputer JUROPA.

Prof. Dr. Gavin Conibeer, Ivan Perez-Wurfl, Supriya Pillai, Shelley Bambrook, and Carolina Gimbert for a great time at the University of New South Wales, Australia.

Josef Klomfaß, Markus Hülsbeck, Oliver Thimm, Patrick Thelen, and Long Dai Trieu for supporting the set up of the microscope and building all this little magic devices, which became an essential part of the microscope.

the IEK5 machine shop for manufacturing countless tiny, unsymmetrical, complex parts with exotic American threads, partly out of brittle ceramic, in no time.

Thomas Beckers for the introduction to near-field microscopy.

Anna Fründ for always providing solutions to sophisticated translation concerns.

André Hoffmann, Florian Köhler and Matthias Schneemann for proofreading this thesis.

Carolin Ulbrich and Beatrix Blank for being the best office mates imaginable!

Tina Leidinger for various (rather unsuccessful) fashion advices.

the producers of Kaspersky anti virus for a free afternoon each Thursday during endless unstoppable virus scans.

the German public transportation companies Deutsche Bahn AG, Rurtalbahn GmbH and the drivers of bus number SB11 for plenty hours on platforms waiting for delayed trains.

the "Rurtalbahner" for making those hours a pleasure.

Jonas Noll, Max Siegloch, Karen Wilken and especially Schnee for many very convenient car rides to and from Cologne.

the 11:45[5] lunch group.

those who I forgot to mention like Anna Heidt, Jan Flohre, Maurice Nuys, Minh Hang Tran, and those, who remain still unmentioned.

my family, especially Thomas and Marita Lehnen.

Thank you very much for your support!

[5] rather 11:50

Band / Volume 256
Entwicklung planarer $Ba_{0,5}Sr_{0,5}Co_{0,8}Fe_{0,2}O_{3-\delta}$-Membranmodule zur Sauerstoffabtrennung und Analyse ihres Transportverhaltens
P. Niehoff (2015), VIII, 134 pp
ISBN: 978-3-95806-044-9

Band / Volume 257
Extension of the Reactor Dynamics Code MGT-3D for Pebble-bed and Block-type High-Temperature-Reactors
D. Shi (2015), x, 162 pp
ISBN: 978-3-95806-045-6

Band / Volume 258
Failure Analysis of Thin Film Solar Modules using Lock-in Thermography
M. Siegloch (2015), XIII, 131 pp
ISBN: 978-3-95806-047-0

Band / Volume 259
Relation between growth rate, material quality, and device grade condition for intrinsic microcrystalline silicon:
From layer investigation to the application to thin-film tandem solar cells
S. Michard (2015), vi, 184 pp
ISBN: 978-3-95806-048-7

Band / Volume 260
Quantitative analysis of spatially resolved electroluminescence of Cu(In,Ga)Se_2 and a-Si:H thin-film solar cells and modules
T. Tran (2015), iii, 161 pp
ISBN: 978-3-95806-050-0

Band / Volume 261
Influence of the surface composition and morphology on the reflectivity of diagnostic mirrors in a fusion reactor
M. Matveeva (2015), 158 pp
ISBN: 978-3-95806-051-7

Band / Volume 262
Very High Cycle Fatigue Behavior of Riblet Structured High Strength Aluminum Alloy Thin Sheets
S. Stille (2015), XII, 123 pp
ISBN: 978-3-95806-054-8

Band / Volume 263
The role of soil heterogeneity on field scale evapotranspiration: 3D integrative modelling and upscaling of root water uptake
K. Huber (2015), xii, 128 pp
ISBN: 978-3-95806-057-9

Band / Volume 264
Strontium-Diffusion in Cer-Gadolinium-Oxid als Degradationsmechanismus der Festoxid-Brennstoffzelle
T. Mandt (2015), iii, 160 pp
ISBN: 978-3-95806-058-6

Band / Volume 265
Cluster analysis of European surface ozone observations for evaluation of MACC reanalysis data
O. Lyapina (2015), 187 pp
ISBN: 978-3-95806-060-9

Band / Volume 266
Real-time quantification of oxygen isotope exchange between carbon dioxide and leaf/soil water in terrestrial ecosystems with laser-based spectroscopy
L. Gangi (2015), XX, 156 pp
ISBN: 978-3-95806-061-6

Band / Volume 267
Secondary Uranium Phases of Spent Nuclear Fuel – CoXnite, $USiO_4$, and Studtite, UO_44H_2O – Synthesis, Characterization, and Investigations Regarding Phase Stability
S. Labs (2015), 153, xlii pp
ISBN: 978-3-95806-063-0

Band / Volume 268
Chemische, verfahrenstechnische und ökonomische Bewertung von Kohlendioxid als Rohstoff in der chemischen Industrie
A. Otto (2015), viii, 272 pp
ISBN: 978-3-95806-064-7

Band / Volume 269
In Vorbereitung

Band / Volume 270
Investigation of light propagation in thin-film silicon solar cells by dual-probe scanning near-field optical microscopy
S. Lehnen (2015),120 pp
ISBN: 978-3-95806-066-1

Weitere ***Schriften des Verlags im Forschungszentrum Jülich*** unter
http://wwwzb1.fz-juelich.de/verlagextern1/index.asp

Energie & Umwelt /
Energy & Environment
Band / Volume 270
ISBN 978-3-95806-066-1